M/EEG Source Imaging via the Spatiotemporal Kalman Filter and its Applications in Epileptology

Dissertation

zur Erlangung des akademischen Grades
Doktor der Ingenieurwissenschaften
(Dr.-Ing.)
der Technischen Fakultät
der Christian-Albrechts-Universität zu Kiel

vorgelegt von

Laith Hamid

Kiel 2018

1. Berichterstatter:	Prof. Dr.-Ing. Ulrich Heute
2. Berichterstatter:	Prof. Dr. med. Ulrich Stephani
Datum der mündlichen Prüfung:	05.12.2018

Declaration

This thesis is an account of research undertaken between June 2010 and August 2018 at the Department of Digital Signal Processing and System Theory, Institute of Electrical and Information Technology, Faculty of Engineering, University of Kiel, Kiel, Germany.

Except where acknowledged in the customary manner, the material presented in this thesis is, to the best of my knowledge, original and has not been submitted in whole or part for a degree in any university. This work was prepared to be in compliance with the rules set by the German Research Foundation (Deutsche Forschungs Gemeinschaft, DFG).

Laith Hamid
Kiel, 06.09.2018

Acknowledgments

First I would like to thank and express my utmost gratitude to my supervisors: Prof. Dr. Ulrich Heute and Prof. Dr. Ulrich Stephani. This thesis would not have been completed without their kind and continuous support, feedback, patience, and guidance. I would also like to thank Prof. Dr. Michael Siniatchkin for his support and interest in the development and application of the spatiotemporal Kalman filter. The algorithmic developments in this thesis and the methodological comparisons were all performed with the help of Dr. Andreas Galka who has helped me countless times in data analysis and paper writing. I am very grateful for his support. I would like to thank Prof. Dr. Gerhard Schmidt too for supervising my master students. I would also like to thank all the professors from the projects SFB855, PAK902, and SFB1261 who gave me feedback on my results and answered my questions.

I would like to thank Dr. Natia Japaridze for her immense help in selection of EEG data and evaluation of source imaging results. Additionally, I would like to acknowledge the kind help of Dr. Frederike Möller, Dr. Lydia Elshoff, and Dr. Gert Wiegand for providing clinical EEG data. I would like to thank my colleagues: Dr. Vera Moliadze, Dr. Navah Kadish, Dr. Jan Möhring, and Nawar Habboush for the nice environment in our working group. Many thanks go to the students who worked with me for a Hiwi job or who did their master thesis on our Kalman filter: Ali Al-Farawn, Nawar Habboush, Masoud Sarabi, Andreja Kostic, and Juan-Pablo Neira. I am also grateful for all the feedback that I received from the doctoral students who worked within the SFB855, PAK902, and SFB1261. Finally, I would like to thank our cooperation partners in Münster, Freiburg, and Rennes for their input and feedback that helped improve the quality of this work.

My thanks and gratitude go also to my family: my parents, siblings, aunts, uncles, and the rest of my family who supported me during my research time. I thank my beloved, Ekaterina, for her constant support, love, and faith in me. I thank my friends Haydar, Erfan, Atheer, Anatol, and Hussein for their support and encouragement. The rest of my friends have also helped with their emotional support.

I would like to acknowledge the financial support of the German Research Foundation (DFG) through the projects SFB855, PAK902, and SFB1261. This research was also funded, in part, by the European Union's Seventh Framework Program for research, technological development and demonstration through the project DESIRE Development Epilepsy (Grant Agreement no: 602531), WP2 WP4, http://epilepsydesireproject.eu/. The FEM head modeling was supported by DFG projects WO1425/2-1,7-1.

Abstract

Source imaging of electroencephalography (EEG) or magnetoencephalography (MEG) has shown promising results in the identification of the epileptogenic zone for epilepsy surgery. M/EEG source imaging requires the solution of the M/EEG inverse problem. Most of the approaches are, however, static approaches that ignore the temporal information in the recordings. Dynamical inverse solutions that are based on state-space models consider this information and use the Kalman filter to reconstruct the current density in the brain. The spatiotemporal Kalman filter (STKF) was implemented to tackle the high-dimensional M/EEG inverse problem.

The aim of this thesis was to continue the algorithmic development of the STKF and its regional variant, the regional STKF (RSTKF), and to investigate their applicability in the field of epileptology using simulated and clinical EEG recordings of epileptic spikes and focal seizures. The accuracy and spatial resolution of the STKF and the RSTKF were evaluated and compared to those of LORETA (low resolution brain electromagnetic tomography), a standard static method. The results were evaluated using visual inspection by an epileptologist, atlas labels, or postoperative magnetic resonance images.

The grid choice and the definition of the Laplacian matrix influence the performance of the STKF. The best STKF results were obtained when a full-brain grid was used together with the modified definition of the Laplacian matrix. Compared to LORETA, the results of the STKF were more focal and closer to the target area. Additionally, moderate spike averaging improved the results of the STKF. The STKF outperformed LORETA in case of low-resolution EEG data with 9-45 electrodes. For high-resolution EEG data with 64 electrodes or more, an additional dimensionality reduction step that is based on singular value decomposition was successfully added to the STKF algorithm to stabilize and accelerate the STKF, and to suppress spurious sources. In addition to that, STKF was applied, for the first time, to EEG recordings of a focal seizure and it outperformed LORETA with respect to the accuracy and consistency of the localization. For simultaneously-measured MEG-EEG recordings, the measurement model was generalized in order to perform MEG-EEG fusion within the framework of source analysis. MEG-EEG fusion produced more accurate and more stable results compared to the separate analysis of MEG or EEG data. Finally, the dynamical model of the RSTKF was extended to describe seven regions. The performance of the RSTKF was superior to that of LORETA and STKF, especially when the depth of the source increased.

The STKF may find application in the localization of the epileptogenic zone from low-resolution EEG data of focal seizures, non-averaged, or moderately averaged spikes, when the

source is superficial. For deeper sources, RSTKF may produce more accurate results.

Zusammenfassung

Quellenbildgebung hat in der Elektroenzephalographie (EEG) und Magnetoenzephalographie (MEG) vielversprechende Ergebnisse bei der Identifizierung epileptogener Zonen für die Epilepsiechirurgie geliefert. Für die M/EEG-Quellenbildgebung ist eine Lösung des inversen Problems des M/EEGs notwendig. Die meisten Lösungsansätze sind aber statisch und ignorieren die zeitliche Komponente in den Aufzeichnungen. Dynamische inverse Lösungen, die auf Zustandsraum-Modellen basieren, berücksichtigen diese und nutzen das Kalman-Filter, um die Quellstromdichte im Gehirn zu rekonstruieren. Das raumzeitliche oder spatiotemporale Kalman Filter (STKF) wurde implementiert, um die Hochdimensionalität des inversen Problems des M/EEGs beherrschbar zu machen.

Das Ziel dieser Arbeit war die algorithmische Weiterentwicklung des STKF und seiner regionalen Variante (RSTKF) sowie die Untersuchung ihrer Anwendbarkeit in der Epileptologie unter Verwendung simulierter und klinischer EEG-Aufzeichnungen von epileptischen Spikes und fokalen Anfällen. Dabei wurden Genauigkeit und räumliche Auflösung des STKF und des RSTKF bewertet und mit denen von LORETA (low resolution brain electromagnetic tomography), einem statischen Standardverfahren, verglichen. Die Ergebnisse wurden von einem Epileptologen visuell inspiziert sowie mittels Hirnatlas-Referenzregionen oder postoperativer Kernspintomogramme bewertet.

Die Wahl des Gehirn-Rasters und die Definition der Laplace-Matrix beeinflussen die Leistung des STKFs. Die besten STKF Ergebnisse wurden mit einem vollständigen Gehirn-Raster und der modifizierten Definition der Laplace-Matrix gewonnen. Im Vergleich zu LORETA waren diese fokaler und näher am Zielbereich. Zusätzlich verbesserte die Mittelung einer mittelgroßen Anzahl von Spikes die Ergebnisse des STKF. Das STKF übertraf LORETA im Falle niedrigauflösender EEG-Daten mit 9-45 Elektroden. Bei hochauflösenden EEG-Daten mit 64 Elektroden oder mehr wurde ein zusätzlicher, auf Singulärwertzerlegung basierender Dimensionalitätsreduktionsschritt erfolgreich zum STKF Algorithmus hinzugefügt, um das STKF zu stabilisieren, zu beschleunigen und störende Quellen zu unterdrücken. Darüber hinaus wurde das STKF zum ersten Mal auf EEG-Aufzeichnungen eines fokalen Anfalles angewendet und schnitt dabei besser ab als LORETA, bezogen auf Genauigkeit und Konsistenz der Lokalisation. Bei simultan gemessenen MEG-EEG-Aufzeichnungen wurde das Messmodell generalisiert, um eine MEG-EEG-Fusion im Rahmen der Quellenanalyse durchzuführen. Diese produzierte genauere und stabilere Ergebnisse im Vergleich zur getrennten Analyse von MEG- und EEG-Daten. Schließlich wurde das dynamische Modell des RSTKF von zwei auf sieben

Regionen erweitert. Die Leistungsfähigkeit des RSTKF übertraf die von LORETA und STKF, insbesondere mit Zunahme der Quellentiefe.

Das STKF könnte Anwendung finden bei der Lokalisierung der epileptogenen Zone aus niedrigauflösenden EEG-Daten fokaler Anfälle und nicht gemittelter oder moderat gemittelter Spikes, wenn die Quelle oberflächlich ist. Bei tiefer liegenden Quellen könnte RSTKF genauere Ergebnisse liefern.

Contents

Abbreviations

dB	Decibel
fT	femto Tesla
Hz	Hertz
ms	milliseconds of time
mm	millimeter
rad/s	radians per second
S/m	Siemens per meter
s	seconds of time
mV	millivolt

3D	three dimensional
ABIC	Akaike Bayesian Information Criterion
AIC	Akaike Information Criterion
AR(p)	Autoregressive Model of Order p
BE	Boundary Elements
BEM	Boundary Element Method
BFGS	Broyden-Fletcher-Goldfarb-Shanno
CAR	common average reference
CSF	Cerebro-spinal Fluid
DBS	Deep Brain Stimulation
DTI	Diffusion Tensor Image
ECoG	Electrocorticography
EEG	Electroencephalography
EMD	empirical mode decomposition
FE	Finite Elements
FEM	Finite Element Method
FD	Finite Difference
FDM	finite Difference Method
fMRI	functional MRI
FCD	Focal Cortical Dysplasia
GARCH	Generalized Autoregressive Conditional Heteroscedasticity
GCV	generalized cross-validation
HR-EEG	High-resolution EEG
ICA	Independent Component Analysis

KF	Kalman Filter
LFM	Lead Field Matrix
LORETA	Low Resolution Electrical Brain Tomography
LR-EEG	Low-resolution EEG
MATLAB	Matrix Laboratory
MEG	Magnetoencephalography
ML	Maximum Likelihood
MNE	Minimum Norm Estimate
MNI	Montreal Neurological Institute
MRI	Magnetic Resonance Image
PCA	Principal Component Analysis
PET	Positron Emission Tomography
RMS	Root Mean Square
ROI	Region of Interest
RSTKF	Regional Spatiotemporal Kalman Filter
SNR	Signal-to-Noise Ratio
SPECT	Single Photon Emission Computed Tomography
SPM	Statistical Parametric Mapping
STKF	Spatiotemporal Kalman Filter
STN	Subthalamic Nucleus
SVD	Singular Value Decomposition
TLE	Temporal Lobe Epilepsy
TSVD	truncated singular value decomposition

Notation

Functions and Operators

$\log_{10}$	the logarithm to base 10
$\mathbf{x}^{\intercal}$	vector or matrix transpose
$\mathbf{L}^{-1}$	the inverse of a matrix
$\mathscr{L}$	the Log-likelihood or natural logarithm of the likelihood function
$\mathscr{L}^{(II)}$	the type-II Log-likelihood
$\|\|\mathbf{x}\|\|_2$	2-norm of a vector
$\hat{\mathbf{j}}$	The estimate of a vector
AR(p)	Autoregressive Model of Order p

List of Variables

$\mathbf{1}_N$	vector of ones of dimension $N \times 1$
$\mathbf{A}$	the state-space model's state-transition matrix
$\mathbf{A}_0$	an intermediate matrix in the calculation of the modified Laplacian matrix
$\mathbf{A}_1$	an intermediate matrix in the calculation of the modified Laplacian matrix
$\mathbf{A}_2$	an intermediate matrix in the calculation of the modified Laplacian matrix
$\mathbf{A}_L$	the state-space model's local state-transition matrix
A_{pp}	peak-to-peak amplitude of an epileptic spike measured between its positive and negative peaks
a_1	first autoregressive model parameter that describes the voxel's contribution to its own dynamics
a_2	second autoregressive model parameter that describes the voxel's contribution to its own dynamics
$\mathbf{B}$	the state-space model's input matrix
$\mathbf{B}_L$	the state-space model's local input matrix
b	input parameter that describes the contribution of neighboring voxels to a voxel's dynamics
$\mathbf{d}(t)$	time series of a single channel of measurements
$\mathbf{d}_n(t)$	normalized time series of a single channel of measurements
$\mathbf{G}_t$	optimal Kalman gain matrix

$\mathbf{G}_{v,t}$	local optimal Kalman gain matrix
$mathbfg$	a point in 3D space on the source grid
$\mathbf{H}$	average-reference matrix
$\mathbf{I}_N$	identity matrix of dimension $N \times N$
$\mathbf{j}$	the brain's current density vector
$\tilde{\mathbf{j}}$	The brain's current density vector post Laplacianization
$\mathbf{j}_{t-1\|t-1}$	filtered current density vector at time $t-1$
$\mathbf{j}_{t\|t-1}$	predicted current density vector at time t
$\mathbf{j}_{t\|t}$	filtered current density vector at time t
$\mathbf{j}_{v,t-1\|t-1}$	voxel-specific filtered current density vector at time $t-1$
$\mathbf{j}_{v,t\|t-1}$	voxel-specific predicted current density vector at time t
$\mathbf{j}_{v,t\|t}$	voxel-specific filtered current density vector at time t
$\mathbf{j}_{v,t-1}$	voxel-specific current density vector at time $t-1$
$\mathbf{j}_{v,t}$	voxel-specific current density vector at time t
$\bar{\mathbf{j}}_{v,t}$	voxel-specific prediction vector of the current density at time $t+1$
$\bar{\mathbf{j}}_{v,t-1}$	voxel-specific prediction vector of the current density at time t
$\mathbf{K}$	the lead field matrix
$\mathbf{K}_{avr}$	the lead field matrix after re-referencing to the common average reference
$\mathbf{K}_e$	the lead field matrix of electrical EEG measurements
$\mathbf{K}_f$	the combined lead field matrix of electrical EEG and magnetic MEG measurements
$\mathbf{K}_m$	the lead field matrix of magnetic MEG measurements
$\mathbf{K}_{sp}$	the lead field matrix after pre-transformation spatial projection
$\tilde{\mathbf{K}}$	the lead field matrix post Laplacianization
$\tilde{\mathbf{K}}_{sp}$	the Laplacianized lead field matrix after post-transformation spatial projection
$\tilde{\mathbf{K}}_v$	voxel-specific matrix extracted from the matrix $\tilde{\mathbf{K}}$
$\mathbf{L}$	the classical Laplacian matrix
$\mathbf{L}_{mod}$	the modified Laplacian matrix
$\mathscr{L}$	the natural logarithm of the likelihood function or Log-likelihood
$\mathscr{L}^{(II)}$	the type-II Log-likelihood
m_d	mean value of time series d
N_e	the number of channels of electrical EEG measurements
N_j	the number of sources in the brain
N_{KF}	the number of parameters specific to STKF or RSTKF
N_L	the number of parameters specific to LORETA
N_m	the number of channels of magnetic MEG measurements
N_f	the combined number of channels of electrical EEG and magnetic MEG measurements
N_{st}	the dimension of the state in a state-space model
N_T	the number of time points (in samples) of a time series
N_v	the number of voxels or grid points in the brain's grid
N_y	the number of observations or measurements
q	grid resolution or spacing of the 3D grid

$\mathbf{r}_{\mathbf{j}t}$	source-space innovations
$\mathbf{r}_{jv,t}$	voxel-specific source-space innovations
$\mathbf{r}_{\mathbf{y}t}$	sensor-space innovations
N_r	number of brain regions for the RSTKF
RMS_B	root mean square value of the pre- and post-spike background activity
RMS_N	root mean square value of the measurement noise
RMS_S	root mean square value of the desired signal
$\mathbf{S}$	diagonal matrix of singular values that results from singular value decomposition
s_i	i_{th} singular value
$\mathbf{S}_e$	matrix of observation scales for EEG measurements
$\mathbf{S}_m$	matrix of observation scales for MEG measurements
s_{y_e}	state-space observation scaling parameter for EEG data
s_{y_m}	state-space observation scaling parameter for MEG data
SNR	signal-to-noise ration of a time series
$t-1$	previous time point in samples
$t+1$	next time point in samples
t	current time point in samples
$\mathbf{U}$	left-singular matrix that results from singular value decomposition
$\mathbf{u}$	vector of inputs
$\mathbf{u}_{v,t}$	voxel-specific vector of inputs
u	grid spacing or resolution
$\mathbf{V}$	right-singular matrix that results from singular value decomposition
v	the current voxel
$\acute{v}$	the neighboring voxel of the current voxel v
w	number of singular values that are higher than the threshold of spatial projection
x	Cartesian x-axis
$\mathbf{y}$	data vector of observations or sensor-space measurements
$\mathbf{y}_e$	data vector of electrical EEG observations
$\mathbf{y}_f$	data vector of combined electrical EEG and magnetic MEG observations
$\mathbf{y}_m$	data vector of of magnetic MEG observations
$\mathbf{y}_{sp}$	data vector of observations or sensor-space measurements after spatial projection
$\mathbf{y}_{t\|t-1}$	vector of current data prediction
$\bar{\mathbf{y}}$	The vector that results from the multiplication of $\mathbf{U}^T$ by $\mathbf{y}$
y	Cartesian y-axis
$\mathbf{y}_{avr}$	data vector of observations or measurements after re-referencing to the common average reference
$\bar{y}_i$	The i_{th} element of $\bar{\mathbf{y}}$
z	Cartesian z-axis
ε	vector of the state-space model's observation or measurement noise
ε_e	vector of the state-space model's EEG-specific observation or measurement noise
ε_f	combined vector of the state-space model's MEG-specific and EEG-specific observation or measurement noises
ε_m	vector of the state-space model's MEG-specific observation or measurement noise

η	vector of the state-space model's dynamical noise
θ_{KF}	vector of state-space model parameters specific to STKF or RSTKF
λ	regularization parameter
$\Sigma_{\mathbf{j}_{t-1\|t-1}}$	covariance matrix of filtered current density vector at time $t-1$
$\Sigma_{\mathbf{j}_{t\|t-1}}$	covariance matrix of predicted current density vector at time t
$\Sigma_{\mathbf{j}_{t\|t}}$	covariance matrix of filtered current density vector at time t
$\Sigma_{j_{v,t-1\|t-1}}$	voxel-specific covariance matrix of filtered current density vector at time $t-1$
$\Sigma_{j_{v,t\|t-1}}$	voxel-specific covariance matrix of predicted current density vector at time t
$\Sigma_{j_{v,t\|t}}$	voxel-specific covariance matrix of filtered current density vector at time t
$\Sigma_{\mathbf{r}_{y,t}}$	covariance matrix of sensor-space innovations
Σ_{ε}	covariance matrix of the state-space model's observation or measurement noise
$\Sigma_{\varepsilon e}$	covariance matrix of the state-space model's EEG-specific observation or measurement noise
$\Sigma_{\varepsilon f}$	combined covariance matrix of the state-space model's MEG-specific and EEG-specific observation or measurement noises
$\Sigma_{\varepsilon m}$	covariance matrix of the state-space model's MEG-specific observation or measurement noise
σ	global standard deviation of measurements
σ^2_{ε}	variance of the state-space model's observation or measurement noise
$\sigma^2_{\varepsilon e}$	variance of the state-space model's EEG-specific observation or measurement noise
$\sigma^2_{\varepsilon m}$	variance of the state-space model's MEG-specific observation or measurement noise
σ_{ε}	standard deviation of the state-space model's observation or measurement noise
Σ_{η}	covariance matrix of the state-space model's dynamical noise
$\Sigma_{\eta L}$	voxel-specific covariance matrix of the state-space model's dynamical noise
σ_{η}	standard deviation of the state-space model's dynamical noise
Ω	neighborhood matrix for a specific 3D grid
$\mathrm{diag}\,(c_1,c_2,\ldots)$	a diagonal matrix with elements $c_1,c_2,\ldots$ on the main diagonal

Chapter 1

Introduction

1.1 Motivation

Epilepsy is the second most common neurological disorder and is characterized mainly by the occurrence of epileptic seizures [Cha94]. About two thirds of cases of epilepsy can be treated using medication. The other one third of the cases displays resistance to pharmacological therapy. In this group some patients can be treated by epilepsy surgery. If a single resectable focus is successfully localized, there is a high probability that the patient will become seizure-free afterwards. During the presurgical evaluation a set of diagnostic measures involving neuroimaging modalities are used to localize the epileptogenic zone, the removal of which should lead to seizure freedom. The localization of the generators of epilepsy in the brain and reconstruction of sources and networks require neuroimaging methods with good spatial and temporal resolutions. Non-invasive electrophysiological modalities such as electroencephalography (EEG) or magnetoencephalography (MEG) measure the potential differences on the human scalp, in case of EEG, or the magnetic fields near the head surface, in case of MEG. These two modalities measure, with a high temporal resolution, the activity that is generated by the summation of the postsynaptic currents or potentials of the pyramidal cortical cells, which are arranged in a favorable geometric position to produce a constructive summation of their potentials when enough cells are simultaneously and synchronously active [dS13].

In the last 10 years there have been several studies that evaluated the accuracy of source imaging of surface EEG and compared its results to postsurgical magnetic resonance images (MRIs) and results from other invasive as well as non-invasive brain imaging modalities such as positron emission tomography (PET) and single photon emission computed tomography (SPECT). In [BLS$^+$09] the accuracy of EEG source imaging was investigated using high-resolution EEG (HR-EEG) recordings from 14 patients of epilepsy with large brain lesions. Postsurgical MRIs were used to validate the results of source imaging. In 85% of the cases, source imaging results were localized within the lesion. In [BSL$^+$11] a prospective study of 152 patients of epilepsy was conducted to compare the sensitivity and specificity of EEG source imaging in case of low-resolution EEG (LR-EEG) to those of source imaging with high-resolution EEG. Additionally, the data were used to compare the accuracy of source imaging when individual anatomy is used compared to the case of standard anatomy. Finally, EEG source imaging was compared to PET, SPECT and MRI. The results showed that the combination of HR-EEG with individual anatomy had the highest values for sensitivity (84%) and specificity (88%). Additionally, the comparison of these values with the sensitivity and specificity of MRI, PET or SPECT showed that EEG source imaging with HR-EEG and individual anatomy outperformed each one of these modalities. Finally, [LPV$^+$16] investigated the predictive values of source imaging with HR-EEG, MRI, PET and SPECT in the presurgical stage using data from 190 patients of epilepsy. Source imaging with HR-EEG had the highest predictive value of postsurgical seizure freedom followed by MRI. When source imaging and MRI agreed, the highest predictive value was reached. All of the above-mentioned studies point to the advantages of EEG-based source imaging for the localization of the epileptogenic zone.

EEG systems are low-cost, mobile and widely available in clinics around the world. EEG has an excellent temporal resolution (down to 1-0.05 ms) and a spatial sampling with electrode caps that have up to 256 electrodes. 64, 128, or 256 electrodes are used in high-resolution or high-density EEG. In low-density EEG, electrode montages with less than 64 electrodes are used. Low-density EEG is still the norm in many clinics, research centers, gaming, and mobile EEG. The measured signals have large amplitudes (μV to mV range), and the systems allow experimental flexibility. MEG has been thought of as a replacement to and an improvement on EEG, since MEG has a higher spatial resolution than EEG and is less influenced by volume conduction effects. MEG systems, however, are costly to acquire and to maintain since they require a constant supply of liquid helium and a shielded room to perform the measurements. For children, the distance between the sensors and the brain can be very large in certain head areas due to the helmet design in MEG devices. Additionally, they are immobile, less flexible, and sensitive to movement. This limits the applicability of MEG in comparison to EEG. Recently, the complementarity of MEG and EEG has been more emphasized which led to research about MEG-EEG fusion. For analyses on the sensor-level, the spatial resolution, especially for EEG, is very limited and the volume conduction effect distorts the localization of interesting phenomena and connectivity analyses. In order to increase the spatial resolution of EEG measurements, source imaging is used. In this approach, the EEG inverse problem is solved and an estimate of the current density in the whole brain is computed. The solution of the EEG inverse problem enables a localization of the generators in addition to the reconstruction of the time courses of activity. In a subsequent step, the time courses of activity of certain regions of interest (ROIs) can be used to estimate connectivity among brain regions for network reconstruction.

In the first step of source imaging, the EEG data are read and preprcoessed. Artifact reduction, dimensionality reduction and re-referencing are performed in this stage. In the next step, the EEG forward problem is solved to calculate the lead field matrix (LFM), which maps the source locations to the sensors and includes information about the geometries and conductivities of the head tissues. If individual MRIs are available, realistic and individual head models can be used. If the individual anatomy is not available, averaged MRIs are segmented to extract the geometries of the brain, skull and skin compartments. Standard conductivity values from the literature are used for head modeling. Realistic head models can be numerically computed using the boundary element (BE), finite element (FE) or finite difference (FD) methods. After that, the EEG data and the lead field matrix are used in conjunction with an inverse method to estimate the current density distribution in the brain. Finally, statistical analyses or network reconstruction can be performed on the source imaging results.

The imaging of the brain from surface EEG data can be performed using any one of three main approaches. In the first approach the surface EEG is assumed to be generated from a few current dipoles in the brain whose locations, orientations and intensity are estimated. Since these current dipoles can only represent the activity in a certain brain area, the exact location and extension of the epileptogenic area cannot be easily delineated. In the second approach, the so-called beamformer approach, the current density of every brain voxel is sequentially reconstructed for one voxel at a time under the assumption of lack of correlation between the voxels. This approach requires a good estimate of the data covariance from a long enough segment of data and can face problems when the data includes strong correlations. In the final approach, the distributed sources imaging approach, the current density vectors of all voxels are simultaneously estimated. These methods need some constraints to obtain a unique solution to the severely underdetermined EEG inverse problem. The accuracy of the solution depends on the constraints and the mathematics of the method. Most of the methods in this approach are static methods, i.e., they reconstruct the current density at a certain time point ignoring the results of the previous time points. Standard methods in the field such as minimum norm estimate (MNE) [Häm84] and low-resolution electromagnetic brain tomography (LORETA) [PMML94] belong to this category. For a review on EEG inverse methods, please refer to [BML01, GCM+08, JKM+14]. The temporal information of the EEG recordings include useful information about the locations of the sources and the interactions between them. A dynamical source imaging method, such as the Kalman filter [Kal60], takes these temporal information included in the measurements into account. The Kalman filter, mostly in its non-linear form, has found many applications in inverse modeling especially in climate and ocean modeling [NP15]. There is still a great potential for this method to be applied in the field of brain modeling and source imaging.

The spatiotemporal Kalman filter (STKF) [GYO+04b] is a modification of the traditional Kalman filter that is especially developed to deal with the high dimensionality of the M/EEG inverse problem. The advantage of the STKF approach is that it is based on a very flexible state space model. A state space model has two equations that describe the spatiotemporal dynamics in the brain and the measurement process respectively. The generalization of any one of these equations can enable models with regional dynamics in the brain or fusion of MEG-EEG recordings. State space modeling also permits the inclusion of the temporal information in the EEG recordings into the solution of the EEG inverse problem. The Kalman filter estimates the current density in the brain, which is the state variable in the state-space model. The other model parameters in the state space model that describe the brain dynamics and measurement need to be estimated via maximum-likelihood. Maximum likelihood parameter estimation is implemented here by minimizing the Akaike information criterion (AIC). So a parameter estimation phase to find the optimal model parameters precedes the current density estimation when STKF is used.

The STKF is based on a modified version of the original Kalman filter using a linear state-space model with spatially and temporally constant parameters. The performance of the method depends on the dynamical model and the accuracy of the results may be improved with more accurate and more physiological dynamical models. This method was first published in [GYO$^+$04b]. After that it was further investigated in [BRK$^+$09]. An important limitation of this model is that it assumes spatial homogeneity of the brain. Furthermore, it does not adapt the parameters in time. Additionally, there was no clarity about which factors influence the consistency of localization, accuracy and spatial resolution of the STKF. The strengths and weaknesses of the STKF, compared to the instantaneous methods, were not investigated in enough detail.

A further development of the model came with the state-space GARCH approach [GYO04a, WGYO06], where GARCH stands for generalized autoregressive conditional heteroskedasticity. In this approach, a further step in the direction of time-varying parameters was taken. Based on the authors' experience, the dynamical noise variance parameter was judged to be the most influential and, hence, it was adapted with time by means of its inclusion into the state vector. The state-space GARCH approach was further developed for EEG source imaging in [GOM$^+$08].

First results on another generalization of the STKF resulted from the diploma thesis of Philipp Stern [Ste08]. Here spatial heterogeneity of model parameters was introduced to the STKF using only two brain regions and simulated and clinical EEG data were used to test the idea.

Since both LORETA and STKF use spatial smoothness constraints, it has been useful to compare their performance to deduce the additional advantages of temporal smoothness in the STKF model. The standard model of the STKF was found to be superior to LORETA with respect to localization of sources of alpha rhythms and epileptiform discharges in EEG recordings [GYO$^+$04b, GOM$^+$08]. Non-averaged segments of interest (for example, non-averaged epileptiform discharges) were used in these analyses and there was no need to average similar events.

1.2 Aim of the Thesis

This work aims at continuing the algorithmic development of the spatiotemporal Kalman filter (STKF) and testing new and generalized variants of this method to improve the accuracy and spatial resolution of M/EEG source imaging. Additionally the application of the STKF and its generalized variants in the field of epileptology can be improved by testing these methods using both simulated and clinical recordings with relevance to epileptology and presurgical evaluation. The strengths and weaknesses of the STKF and its variants still need to be investigated should the method find wider application in clinical brain research. The application of non-linear Kalman filters is outside the scope of this thesis. We will constrain ourselves to the development and investigation of the linear spatiotemporal Kalman filter and its variants.

STKF-based solution of the inverse problem needs to be evaluated and compared to results of other neuroimaging modalities and standard methods of M/EEG source reconstruction. The results of a source imaging methods can be validated using various approaches. The first approach includes the comparison of the reconstructed sources with original source in simulated EEG data. In another approach, the source reconstruction results can be compared with electrocorticographic (ECoG) recordings in simultaneous EEG-ECoG data. Similarly, comparison with stereotaxic depth electrode recordings in simultaneous EEG-depth electrode data is also possible. Additionally, Comparison with structural MRI may be used. The reconstructed source can be compared with the malformations or lesions in presurgical MRIs or the resected volume from postsurgical MRI. Finally, EEG-functional MRI (fMRI) results (fMRI-based activation maps) are also used to validate M/EEG source reconstruction. In this work the first and fourth validation strategies will be used to evaluate the performance of the STKF.

In this work we will use state-of-the-art preprocessing and head modeling approaches. We will not apply connectivity analyses and we will concentrate on developing and applying dynamical inverse methods based on Spatiotemporal Kalman filtering. We want to apply the STKF to the analysis of epileptic spikes and focal seizures. First we will investigate the accuracy of source imaging via STKF. Accuracy is defined here relative to a simulated source, resected brain volume or a specific brain region. Additionally, we will comment on the spatial resolution of STKF results since most inverse methods produce smeared estimates of brain sources. We are first interested in the effects of source space definition, source location, and area on the accuracy of STKF results. Similarly, the effect of the number of EEG electrodes, high- or low-resolution EEG, on accuracy and spatial resolution of STKF results will also be studied. We will also study the effect of multimodal fusion (here: MEG-EEG fusion) on the accuracy of STKF results. For the case of high-resolution EEG with 64 electrodes or more, The effect of dimensionality reduction on the accuracy, spatial resolution and computational time of the STKF will be investigated. Finally, we will continue the development of the generalized STKF from [Ste08] with an extended model of regional brain dynamics in order to improve the accuracy and spatial resolution of dynamical EEG source imaging.

1.3 The Contribution of this Thesis

The main contribution of this thesis is in the field on dynamical inverse modeling and improving the applicability of the spatiotemporal Kalman filter and its regional variant in the field of epileptology. Despite the fact that the thesis is mostly concerned with EEG, an example of MEG-EEG fusion will be presented. The thesis only tries to use and not develop state-of-the-art methods in the preprocessing and forward modeling stages and it does not deal with connectivity or network analysis. In the preprocessing step, we will work with either clean or cleaned segments. In the forward modeling step, we will use software packages that compute the head models using implementations of the boundary element method and the finite element method. Within the framework of this doctoral thesis, three master thesis were conducted and successfully finished [Alf14, Sar14, Hab14]. In the forward modeling step, the STKF was used for the first time in conjunction with state-of-the-art volume conductor models computed using the boundary elements (BE) and the finite elements (FE) methods. Additionally, the definition of the source space using 3D grids that discretize the brain's gray matter or the whole brain plays an important role in improving the accuracy of the STKF. An additional improvement in the STKF's accuracy can be obtained by using a modified definition of the Laplacian matrix that corrects for the bias at the borders of the 3D grid [HHJ$^+$15, Alf14].

In the inverse modeling stage, we constrained our efforts to the localization of single sources. We have shown that, compared to instantaneous methods, the additional temporal smoothness constraints in the STKF improve the source imaging of focal seizure onset [HSJ$^+$15, Sar14]. In addition to that, source imaging via STKF shows promising results when low-density EEG data with 32 electrodes or less are used [HAFM$^+$17a, Alf14]. In the case of high-resolution EEG data, STKF has been applied for the first time on high-resolution EEG and we have shown that the introduction of dimensionality reduction via singular value decomposition (SVD) speeds up the STKF, performs denoising, and improves the stability of the inverse solution [HAFM$^+$17b, Alf14]. Furthermore, the generalization of the measurement model to include both EEG as well as MEG data allows for MEG-EEG fusion and improves source imaging [HAW$^+$13]. Some first results were previously obtained [Ste08] on the generalization of the system model from a homogeneous brain to two distinct brain regions to allow for regional dynamics in the brain. The resulting regional STKF (RSTKF) was extended in this thesis to seven brain regions and tested on both simulated and clinical EEG data.

Within the framework of this doctoral thesis, the author supervised the following master theses:

1. A. Alfarawn, "Comparison of static and dynamic source imaging of epileptiform discharges simulated using a neuronal population model," master thesis, Digital Signal Processing and System Theory , Christian-Albrechts-University of Kiel, 2014.

2. M. Sarabi, "EEG source imaging of epileptiform seizures using spatiotemporal Kalman filtering," master thesis, Digital Signal Processing and System Theory , Christian-Albrechts-University of Kiel, 2014.

3. N. Habboush, "MEG-EEG fusion using spatiotemporal Kalman filtering with an emphasis on the correct localization of deep brain sources," master thesis, Digital Signal Processing and System Theory , Christian-Albrechts-University of Kiel, 2014.

The following first-author (in case [3]: shared first authorship) contributions resulted from the author's doctoral research and supervision of master students:

1. Hamid, L.; Aydin, U.; Wolters, C.; Stephani, U.; Siniatchkin, M.; Galka, A., “MEG-EEG fusion by Kalman filtering within a source analysis framework,” Engineering in Medicine and Biology Society (EMBC), 2013 35th Annual International Conference of the IEEE , Osaka, pp. 4819-4822, 2013.
2. Hamid, L.; Sarabi, M.; Japaridze, N.; Wiegand, G.; Heute, U.; Stephani, U.; Galka, A., and Siniatchkin, M., “The Performance of the spatiotemporal Kalman filter and LORETA in seizure onset localization,” Engineering in Medicine and Biology Society (EMBC), 2015 37th Annual International Conference of the IEEE , Milan, Italy, pp. 2741-2744, 2015.
3. Habboush, N.; Hamid, L.; Japaridze, N.; Wiegand, G.; Heute, U.; Stephani, U.; Galka, A.; Siniatchkin, M., “The choice of the source space and the Laplacian matrix in LORETA and the spatio-temporal Kalman filter EEG inverse methods,” Engineering in Medicine and Biology Society (EMBC), 2015 37th Annual International Conference of the IEEE , Milan, Italy, pp. 2745-2749, 2015.
4. Hamid, L.; Dalaf, A.; Merlet, I.; Japaridze, N.; Heute, U.; Stephani, U.; Galka A; Wendling, F. and Siniatchkin, M., “Source reconstruction via the spatiotemporal Kalman filter and LORETA from EEG time series with 32 or fewer electrodes,” Engineering in Medicine and Biology Society (EMBC), 2017 39th Annual International Conference of the IEEE , Seogwipo, South Korea, pp. 2218-2222, 2017.
5. Hamid, L.; Dalaf, A.; Merlet, I.; Japaridze, N.; Heute, U.; Stephani, U.; Galka A; Wendling, F. and Siniatchkin, M., “Spatial projection as a preprocessing step for EEG source reconstruction using spatiotemporal Kalman filtering,” Engineering in Medicine and Biology Society (EMBC), 2017 39th Annual International Conference of the IEEE , Seogwipo, South Korea, pp. 2213-2217, 2017.
6. Hamid L.; Habboush N.; Stern P.; Japaridze N.; Aydin Ã; Wolters C.; Claussen J. C.; Heute U.; Stephani U.; Galka A.; Siniatchkin, M., “Source Imaging of Deep Brain Activity Using the Regional Spatiotemporal Kalman Filter”, submitted to PLOS ONE in December 2017, in review.

Chapter 2

Theoretical Background

2.1 Preprocessing of M/EEG Data

In this thesis we use, for clinical data, clean segments, which include no artifacts, or already cleaned ones after artifact suppression. Modern artifact suppression methods include, among other methods, principal component analysis (PCA), independent component analysis (ICA), wavelet transform, adaptive filtering, empirical mode decomposition (EMD), and state-space modeling [UGZ15, IRY16, SGHSG17]. For the preprocessing step in our analysis, a standardization of the measurements is performed for each data channel as follows:

$$\mathbf{d}_n(t) = \frac{(\mathbf{d}(t) - m_d)}{\sigma}$$

where $\mathbf{d}_n(t)$ represents a time series of length N_T, m_d is the mean of the time series, and σ is the global standard deviation over all N_y channels and N_T time points. The aim of data normalization is to enable the comparison of results across subjects and datasets. After that, for EEG data, the measurements are re-referenced to the common average reference (CAR)[NSW$^+$97]. This is necessary to remove the effect of the reference electrode and approximate a reference-free scenario prior to source localization. According to [PM99], the average-reference matrix is calculated as follows:

$$\mathbf{H} = \mathbf{I}_{N_y} - \frac{\mathbf{1}_{N_y}\mathbf{1}^{\mathsf{T}}{}_{N_y}}{N_y}$$

where $\mathbf{H}$ is of dimension $N_y \times N_y$, $\mathbf{I}_{N_y}$ is the identitiy matrix of similar dimension, and $\mathbf{1}_{N_y}$ is a vector of ones of dimension $N_y \times 1$. The average-referenced EEG data, $\mathbf{y}_{avr}$, is then obtained using:

$$\mathbf{y}_{avr} = \mathbf{H}\mathbf{y}$$

Similarly, the result of the forward modeling step, the $N_y \times N_j$-dimensional lead field matrix $\mathbf{K}$ is transformed via average referencing as follows:

$$\mathbf{K}_{avr} = \mathbf{H}\mathbf{K}$$

where $\mathbf{K}_{avr}$ is the average-transformed lead field matrix. To prevent linear dependence among the rows of the data or the lead field matrices, a single row is removed from each of these matrices.

In the preprocessing step, it is often necessary to estimate the signal-to-noise ratio (SNR) of the measurements. In this thesis we calculate the SNR for oscillatory activity as follows:

$$SNR = 20\log_{10}\left(\frac{RMS_S}{RMS_N}\right)$$

where RMS_S is the root mean square of the clean or cleaned desired signal. RMS_N is the root mean square of the measurement noise and is estimated from the measurements or is known from the characteristics of the measurement equipment. For epileptic spikes, the SNR is calculated from the electrode with the strongest spike as in [OTF07]:

$$SNR = 20\log_{10}\left(\frac{A_{pp}}{RMS_B}\right)$$

where A_{pp} is the peak-to-peak amplitude that is measured between the negative and positive spike peaks. The spike interval is assumed to be 135 ms around the negative spike peak [1]. Prior to and after the spike interval, 150 ms are then used to estimate the RMS of the background activity. In this thesis, we did not fix the spike interval to 135 ms but used the morphological information that can be seen in Fig 2.1 to determine the spike interval. For averaged spikes that were analyzed in this thesis, no post-spike intervals were available. Additionally, pre-spike intervals were very short and were located at the beginning of the dataset. These reasons motivated the decision to take the first 150 ms from each dataset with an averaged spike and use it as the pre- and post-spike background intervals to estimate the RMS of the background activity.

2.2 The M/EEG Inverse Problem

The possible locations of reconstructed dipoles may be described by a 3D regular grid with N_v grid points and a grid spacing or resolution q. The current density at each grid point may be described using a triplet of current dipoles in each of the Cartesian axes x, y, and z. The dimension of the current density vector $\mathbf{j}$ is N_j which is equal to $3N_v$. With the help of the lead field matrix of dimension $N_y \times N_j$, which results from the solution of the M/EEG forward problem, surface electrical or magnetic activity can be computed from a given current density distribution in the brain. The observation or measurement noise ε is modeled to be zero-mean, white, and Gaussian noise of dimension $N_y \times 1$. The $N_y \times N_y$-dimensional covariance matrix of the measurement noise is Σ_ε. The measurement process is assumed to be linear and is described

---

[1] In this thesis, except when explicitly mentioned, the negative spike peak in EEG datasets are plotted pointing upwards.

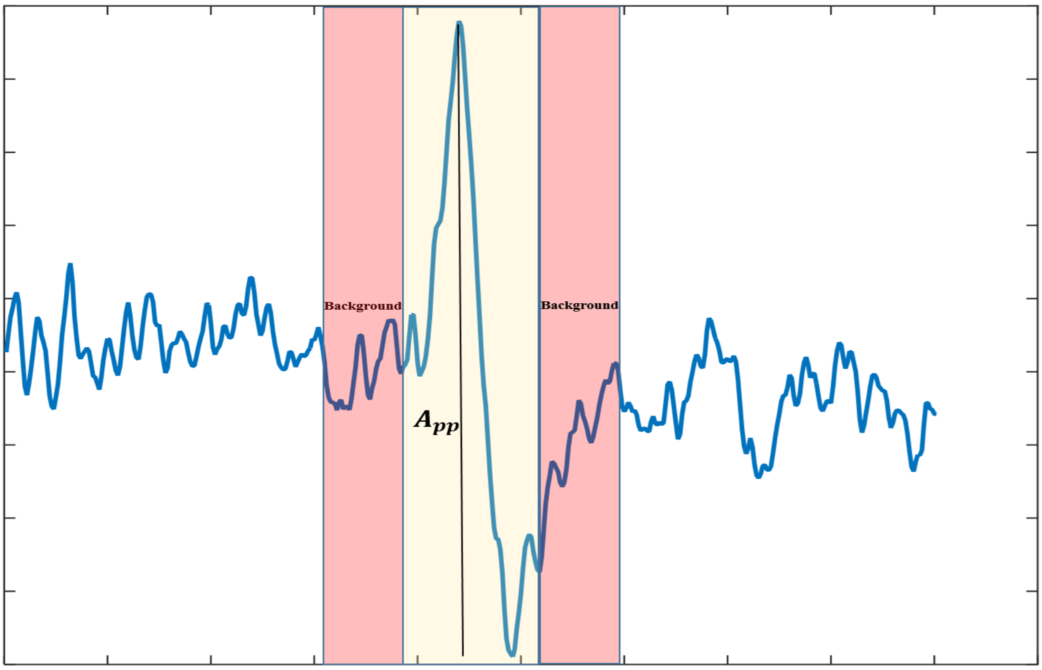

Figure 2.1: *A non-averaged spike is shown with the pre-spike (in red), spike (in yellow), and post-spike (in red) intervals. The valleys at the spike's begin and end are used to determine the spike interval.* A_{pp} *is the peak-to-peak amplitude in the spike interval. The figure was inspired by [OTF07].*

by the following measurement equation:

$$\mathbf{y} = \mathbf{Kj} + \varepsilon$$

In practice, the measurement noise covariance is estimated from the M/EEG data either as a full matrix or as a diagonal one. The current density distribution is reconstructed from the observations and the computed lead field matrix via a source imaging algorithm. In this thesis we will use a standard source imaging approach, low-resolution brain electromagnetic tomography (LORETA) [PMML94], that reconstructs a unique current density distribution from the data by imposing spatial smoothness as a constraint on the solution space. LORETA is a static method that ignores the temporal information in the data and reconstructs the brain activity at a single time point. In contrast to LORETA, we will use a dynamical source imaging approach, the spatiotemporal Kalman filter (STKF) [GYO$^+$04b], which is based on state-space modeling. Current density reconstruction is performed via state estimation while the state-space model parameters are estimated via maximum likelihood (ML). Since source imaging is transformed into a state estimation problem, a dynamical model is used to describe the spatiotemporal evolution of the hidden state, the brain's current density, and this dynamical model is used to make prediction about the value of the current density. These predictions will be optimally fused with the information from the measurements to obtain accurate estimates of the current density.

2.3 LORETA

"low resolution brain electromagnetic tomography" was implemented and published by R. Pascual-Marqui in [PMML94]. The method uses Tikhonov regularization to impose spatial smoothness constraints on the space of possible solutions. A unique solution that has maximum spatial smoothness is found and all other solutions are penalized. The cost function is shown in the equation below:

$$\arg\min_{\mathbf{j}} \left(\|\mathbf{y} - \mathbf{K}\mathbf{j}\|^2 + \lambda^2 \cdot \|\mathbf{L}\mathbf{j}\|^2 \right)$$

λ is the regularization parameter and it is estimated from the M/EEG data via Akaike Bayesian information criterion (ABIC) [GYO+04b, YGO+04]. Other methods exist to estimate the regularization parameter that are based on signal-to-noise ratio (SNR) estimation, truncated singular value decomposition (TSVD), or generalized cross-validation (GCV) [GCM+08].

The $N_j \times N_j$-dimensional Laplacian matrix is calculated according to the classical definition as follows:

$$\mathbf{L} = \left(\mathbf{I}_{N_v} - \frac{1}{6}\Omega \right) \otimes \mathbf{I}_3$$

Ω of dimension $N_v \times N_v$ is the neighborhood matrix for each 3D grid. It includes information about the immediate neighbors of each voxel v in the 3D grid and it is computed using the following equation:

$$\Omega_{\acute{v}v} = \begin{cases} 1 & \text{if } \acute{v} \text{ is a neighbor of } v \\ 0 & \text{otherwise} \end{cases}$$

The popular implementation of LORETA is based on the following equation:

$$\hat{\mathbf{j}} = \left(\mathbf{K}^{\intercal}\mathbf{K} + \lambda^2 \mathbf{L}^{\intercal}\mathbf{L} \right)^{-1} \mathbf{K}^{\intercal}\mathbf{y}$$

This implementation is, however, computationally expensive and requires many inversions of a large matrix. The implementation that we use in this thesis was derived and used first in [GYO+04b, YGO+04]. Please refer to the detailed derivation in [Yam03]. In the alternative equation, the estimate of the current density is obtained as follows:

$$\hat{\mathbf{j}} = \mathbf{L}^{-1}\mathbf{V}_{N_j \times N_y} \operatorname{diag}\left(\frac{s_i}{s_i^2 + \lambda^2} \right) \mathbf{U}^{\intercal}\mathbf{y}$$

where only the $N_j \times N_y$ submatrix of $\mathbf{V}$ is used in the above equation. The lead field matrix is linearly transformed via the Laplacian matrix as shown below:

$$\tilde{\mathbf{K}} = \mathbf{K}\mathbf{L}^{-1}$$

The transformed lead field matrix is now decomposed via singular value decomposition according to the equation:

$$\tilde{\mathbf{K}} = \mathbf{U}\mathbf{S}\mathbf{V}^{\mathsf{T}}$$

Within an Empirical Bayesian framework, ABIC is used both for the estimation of the hyperparameters, here λ and σ_{ε}, and for model comparison [GYO^{+}04b]:

$$\mathrm{ABIC} = -2\mathscr{L}^{(II)}\left(\sigma_{\varepsilon}, \lambda\right) + 2N_L$$

where N_L is the number of hyperparameters. The measurement noise variance is obtained using the following equation:

$$\sigma_{\varepsilon}^2 = \frac{1}{N_y}\sum_{i=1}^{N_y}\frac{\lambda^2}{\lambda^2 + s_i^2}\bar{y}_i^2$$

$\bar{y}_i$ is an element of the transformed vector $\bar{\mathbf{y}}$ that is described in the equation below:

$$\bar{\mathbf{y}} = \mathbf{U}^{\mathsf{T}}\mathbf{y}$$

The final equation of ABIC for all time points in the data is as follows:

$$\mathrm{ABIC}\left(\sigma_{\varepsilon}, \lambda\right) = TN_y \log \sigma_{\varepsilon}^2 + T\sum_{i=1}^{N_y}\log\frac{\lambda^2 + s_i^2}{\lambda^2}$$
$$+\frac{1}{\sigma_{\varepsilon}^2}\sum_{i=1}^{N_T}\sum_{i=1}^{N_y}\frac{\lambda^2}{\lambda^2 + s_i^2}\bar{y}_{i,t}^2 + 2N_L$$

2.4 The Spatiotemporal Kalman Filter (STKF)

The use of the standard Kalman filter [Kal60] to solve the high-dimensional M/EEG inverse problem faces two problems. The first problem concerns the propagation of huge full-rank covariance matrices. The second problem is parameter estimation that includes millions of unknown parameters that need to be learned from the M/EEG data. Sparsity assumptions and strong constraints on the parameter matrices may make the problem more solvable. Reduced-rank Kalman filters, such as the ensemble Kalman filter [Eve94] or reduced-rank square-root filters [VH97], are popular in the very high-dimensional problem of climate modeling. The spatiotemporal Kalman filter (STKF) [GYO^{+}04b] uses a partitioning appraoch to solve the high-dimensional M/EEG inverse problem. In the following, the mathematical theory of the STKF will be explained with the help of information that was adapted from [GYO^{+}04b, GOM^{+}08, Ste08, BRK^{+}09, HAW^{+}13, Alf14, Sar14, Hab14, HSJ^{+}15, HHJ^{+}15]. In the STKF approach, the Laplacian matrix $\mathbf{L}$ is used to decouple the fully-connected state-space model into a partitioned system with strong connectivity only between each voxel and its immediate neighbors. This allows for local low-dimensional Kalman filters at each voxel to estimate the current density of that specific voxel, which is influenced only by the current densities of the neighboring voxels. This transformation is called spatial whitening and is performed on the current density vector $\mathbf{j}$ according to the equation:

$$\tilde{\mathbf{j}}_t = \mathbf{L}\mathbf{j}_t$$

In the Laplacianized state-space model, the transformed lead field matrix $\tilde{\mathbf{K}}$ is obtained according to the formula

$$\tilde{\mathbf{K}} = \mathbf{K}\mathbf{L}^{-1}.$$

The spatial whitening is a linear transformation and it can be reversed by left multiplication of the stacked individual current density estimates for all voxels and time points with the inverse of the Laplacian matrix as follows:

$$\hat{\mathbf{j}}_t = \mathbf{L}^{-1}\hat{\tilde{\mathbf{j}}}_t$$

The global $N_j \times N_j$-dimensional covariance matrix of the current density estimate can be similarly recovered by reversing the spatial whitening transform using the inverse of the Laplacian matrix on the matrix that is constructed from local filtered state covariance matrices for all voxels. This process is described in the following equation:

$$\Sigma_{j_{t|t}} = \mathbf{L}^{-1}\tilde{\Sigma}_{\tilde{j}t|t}\mathbf{L}^{-1^{\mathsf{T}}}$$

For each low-dimensional Kalman filter, the state dimension is N_{st}. In the case of epileptic spikes, we used a first-order autoregressive model, or AR(1), for the dynamical model. This resulted in a 3×1-dimensional state vector. In the description of the Kalman filter equations below we will omit the tilde, although the equations describe the weakly-coupled state-space model. The local dynamical model for voxel v and time t is described by the equation:

$$\hat{\mathbf{j}}_{v,t} = \mathbf{A}_L\hat{\mathbf{j}}_{v,t-1} + \frac{1}{6}\mathbf{B}_L \sum_{\acute{v}\in N(v)} \hat{\mathbf{j}}_{v,t-1|t-1} + \eta_t$$

where $\mathbf{A}_L$ is the local state-transition matrix that propagates the current density vector of voxel v at time $t-1$ to the next time point. The local input matrix $\mathbf{B}_L$ propagates the contributions of the current density vectors of the neighboring voxels, averaged over the number of neighbors, to the dynamics of voxel v forward in time. The white Gaussian dynamical noise η_t represents the unmodeled phenomena that are not described by the deterministic part of the dynamical models, i.e., by the matrices $\mathbf{A}_L$ and $\mathbf{B}_L$. η_t has zero mean and its covariance matrix is $\Sigma_{\eta L}$.

The diagonal $N_{st} \times N_{st}$-dimensional local state-space model matrices that are specific to the dynamical model are described by the following equations [BRK+09]:

$$\mathbf{A}_L = a_1\mathbf{I}_3, \quad \mathbf{B}_L = b\mathbf{I}_3, \quad \Sigma_{\eta L} = \sigma_\eta^2\mathbf{I}_3$$

where a_1 is the state-space's first autoregressive model parameter, which describes the voxel's own contribution to its dynamical development. The parameter b is the state-space model parameter that describes the coupling of voxel v to its immediate neighbors. The voxel-specific dynamical noise covariance matrix $\Sigma_{\eta L}$ describes the stochastic part of the dynamical model through the parameter σ_η^2, which is among the most important state-space model parameters, in practice [GYO04a, GOM$^+$08, Ste08, GWO10, Hab14]. All of these model parameters are assumed to be constant in time and homogeneous in space. Additionally, they are assumed to be the same for all three current dipoles at each voxel.

The global measurement noise covariance matrix Σ_ε of dimension $N_y \times N_y$ is assumed to be diagonal with equal noise power for all channels. It is described by the equation:

$$\Sigma_\varepsilon = \sigma_\varepsilon^2 \mathbf{I}_{N_y}$$

where σ_ε^2 is the state-space model's measurement-noise variance parameter, which is assumed to be the same for all EEG electrodes or MEG sensors.

The measurement model of the state-space model can be expressed as

$$\mathbf{y}_t = \mathbf{K}\mathbf{j}_{t|t} + \varepsilon_t.$$

If dynamical noise variance is fixed during the optimization process, it becomes possible to assign this degree of freedom to the measurement equation by multiplying the observation matrix, i.e., the lead field matrix with observation scaling parameters that can be then optimized. In the case of EEG data, for example, the lead field matrix is multiplied by a scaling matrix of dimension $N_e \times N_e$ according to the following equation:

$$\mathbf{K}_e := \mathbf{S}_e \mathbf{K}_e$$

The scaling matrix has the state-space observation scaling parameter s_{y_e} on the main diagonal. This is shown in the equation below:

$$\mathbf{S}_e = s_{y_e} \mathbf{I}_{N_e}$$

At time t and voxel v, the prediction step of the Kalman filter begins with the $N_{st} \times 1$-dimensional local predicted state, which is calculated as follows:

$$\hat{\mathbf{j}}_{v,t|t-1} = \mathbf{A}_L \hat{\mathbf{j}}_{v,t-1|t-1} + \frac{1}{6}\mathbf{B}_L \sum_{\acute{v} \in N(v)} \hat{\mathbf{j}}_{\acute{v},t-1|t-1}$$

where $\hat{\mathbf{j}}_{v,t-1|t-1}$ is the local filtered state of voxel v at time $t-1$. The predicted state covariance matrix at voxel v is described by the equation:

$$\Sigma_{j_{v,t|t-1}} = \mathbf{A}_L \Sigma_{j_{v,t-1|t-1}} \mathbf{A}_L^\intercal + \Sigma_{\eta L}$$

where $\Sigma_{j_{v,t-1|t-1}}$ is the local filtered state covariance matrix at time $t-1$.

The predicted state is then projected via the lead field matrix to the sensor space to build the predicted measurement $\mathbf{y}_{t|t-1}$ at time t as follows:

$$\mathbf{y}_{t|t-1} = \mathbf{K}\hat{\mathbf{j}}_{t|t-1}.$$

In the measurement update or correction step, the predicted state is corrected by the new information from the measurement at time t. The $N_y \times 1$-dimensional sensor-level innovation or measurement prediction error $\mathbf{r}_{y,t}$ results from the difference between the predicted and the actual measurement vectors at time t according to the equation:

$$\mathbf{r}_{y,t} = \mathbf{y}_t - \mathbf{y}_{t|t-1}$$

The sensor-level innovation covariance matrix of dimension $N_y \times N_y$ is then obtained from

$$\Sigma_{\mathbf{r}_{y,t}} = \sum_{v} \mathbf{K}_v \Sigma_{j_{v,t|t-1}} \mathbf{K}_v^{\intercal} + \Sigma_{\varepsilon},$$

where $\mathbf{K}_v$ is $N_y \times 3$-dimensional and represents the voxel-specific lead field matrix.

The optimal local Kalman gain matrix $\mathbf{G}_{v,t}$ of dimension $N_{st} \times N_y$ is then computed from the following equation:

$$\mathbf{G}_{v,t} = \Sigma_{j_{v,t|t-1}} \mathbf{K}_v^{\intercal} \Sigma_{\mathbf{r}_{y,t}}^{-1}.$$

The Kalman gain matrix is now used to project the sensor-level innovation to the source level and compute the $N_{st} \times 1$-dimensional local source-level prediction error $\mathbf{r}_{\mathbf{j}_{v,t}}$ as follows:

$$\mathbf{r}_{\mathbf{j}_{v,t}} = \mathbf{G}_{v,t}\mathbf{r}_{y,t}.$$

The source-level prediction error is now used to correct the predicted state in order to compute the filtered state $\mathbf{j}_{v,t|t}$ of dimension $N_{st} \times 1$ as shown in the following equation:

$$\hat{\mathbf{j}}_{v,t|t} = \hat{\mathbf{j}}_{v,t|t-1} + \mathbf{r}_{j_{v,t}}.$$

The filtered state covariance matrix is calculated according to the equation

$$\Sigma_{\mathbf{j}_{v,t|t}} = (\mathbf{I}_{N_{st}} - \mathbf{G}_{v,t}\mathbf{K}_v)\,\Sigma_{\mathbf{j}_{v,t|t-1}}.$$

The process is then repeated for the next time point, until all N_T samples are finished.

For the analysis of brain oscillations, we used an autoregressive model of order 2 as the dynamical model. The state dimension N_{st} becomes 6. Instead of two separate equations for the dynamical model, the AR(2) model is reformulated into a single AR(1) model using the following equation:

$$\begin{bmatrix} \hat{\mathbf{j}}_{v,t} \\ \hat{\hat{\mathbf{j}}}_{v,t} \end{bmatrix} = \mathbf{A}_L \begin{bmatrix} \hat{\mathbf{j}}_{v,t-1} \\ \hat{\hat{\mathbf{j}}}_{v,t-1} \end{bmatrix} + \mathbf{B}_L \begin{bmatrix} \frac{1}{6} \sum\limits_{\acute{v} \in N(v)} \hat{\mathbf{j}}_{v,t-1|t-1} \\ \mathbf{0} \end{bmatrix} + \begin{bmatrix} \eta_t \\ \mathbf{0} \end{bmatrix}.$$

where $\bar{\mathbf{j}}_{v,t}$ is the local prediction of the current density vector at time $t+1$. $\bar{\mathbf{j}}_{v,t-1}$ is the corresponding quantity at time t.

The local state-transition matrix has an upper companion form as shown in the following equation:

$$\mathbf{A}_L = \begin{bmatrix} a_1\mathbf{I}_3 & a_2\mathbf{I}_3 \\ \mathbf{I}_3 & \mathbf{0} \end{bmatrix}.$$

The local input matrix $\mathbf{B}_L$ is written as follows:

$$\mathbf{B}_L = \begin{bmatrix} b\mathbf{I}_3 & \mathbf{0} \\ \mathbf{0} & \mathbf{0} \end{bmatrix}.$$

The local dynamical noise covariance matrix has a similar structure like that of the local input matrix. It is written as shown in the following equation:

$$\Sigma_{\eta_L} = \begin{bmatrix} \sigma_\eta^2\mathbf{I}_3 & \mathbf{0} \\ \mathbf{0} & \mathbf{0} \end{bmatrix}.$$

2.5 The Regional Spatiotemporal Kalman Filter (RSTKF)

Wold decomposition [Wol38] shows that stationary processes can be decomposed into deterministic and stochastic processes. The modeling of a time series may concentrate either on improving the deterministic part of the model, while keeping the stochastic part simple, or on improving the stochastic part, while keeping the deterministic part simple[Oza12]. In M/EEG source imaging via STKF, improving the deterministic model would require, e.g., the inclusion of information from structural and functional connectivity research about brain connections in the state-space's dynamical model. The development of the stochastic part of the dynamical model may include spatial or temporal adaptation of the dynamical noise variance parameter. Since the human brain is modular and has the ability to allow several dynamical processes to be simultaneously active in different brain regions, introducing spatial heterogeneity of the dynamical noise variance into the STKF's model with constant parameters may improve the modeling of brain data. The idea of the regional STKF (RSTKF) is to define different brain regions in the brain grid and assign to each one of them its own dynamical noise variance state-space parameter. The parameters are then estimated from the M/EEG data and the current density reconstruction may reveal improved results. An implementation of this idea using two regions and some first results were obtained in the diploma thesis of Philipp Stern [Ste08]. The application of this method in addition to the extension of its model to seven regions will be discussed in chapter 5. Compared to the STKF, the dynamical noise covariance matrix of the RSTKF will take the following form for an AR(1) model:

$$\Sigma_{\eta_L} = \sigma_\eta^2(v)\,\mathbf{I}_3.$$

$\sigma_{\eta}^{2}(v)$ may take a value from a discrete set of regions $r = 1...N_r$. For an AR(2) model, the dynamical noise covariance matrix of the RSTKF is constructed as follows:

$$\Sigma_{\eta_L} = \begin{bmatrix} \sigma_{\eta}^{2}(v)\mathbf{I}_3 & \mathbf{0} \\ \mathbf{0} & \mathbf{0} \end{bmatrix}.$$

2.6 New Developments to the STKF Pipeline

2.6.1 MEG-EEG Fusion

Recordings from each modality in simultaneous MEG-EEG can be separately analyzed and used for source reconstruction. Multimodal fusion via state-space modeling has an advantage, since state-space models are very flexible ones. MEG-EEG fusion will be integrated within the framework of source imaging, such that the different sensitivities of these modalities to the orientations and depths of sources may be optimally used. The generalization of the measurement equation to include sensors from another modality is explained in this section. The N_f-dimensional joint vector of recordings $\mathbf{y}_f$ is formed by stacking the magnetic and electrical recordings together as follows:

$$\mathbf{y}_f = \begin{bmatrix} \mathbf{y}_m \\ \mathbf{y}_e \end{bmatrix}.$$

The magnetic and electrical lead field matrices are similarly combined as shown in the equation below:

$$\mathbf{K}_f = \begin{bmatrix} \mathbf{S}_m\mathbf{K}_m \\ \mathbf{S}_e\mathbf{K}_e \end{bmatrix}.$$

Please note that this model optimizes the observation scaling parameters and, thus, we need one observation scaling parameter for each separate modality. The magnetic observation scaling matrix of dimension $N_m \times N_m$ is constructed as shown in the equation below:

$$\mathbf{S}_m = s_{y_m}\mathbf{I}_{N_m}.$$

The $N_e \times N_e$-dimensional electrical observation scaling matrix is also shown below:

$$\mathbf{S}_e = s_{y_e}\mathbf{I}_{N_e}.$$

The observation noise vectors are also combined in the vector ε_f:

$$\varepsilon_f = \begin{bmatrix} \varepsilon_m \\ \varepsilon_e \end{bmatrix}.$$

The observation noise for MEG is white Gaussian with zero mean and covariance matrix Σ_{ε_m}. For EEG, the observation noise is also white and Gaussian. It also has zero mean and a covariance matrix Σ_{ε_e}.

The combined MEG-EEG measurement noise covariance matrix of dimension $N_f \times N_f$ is constructed as follows:

$$\Sigma_{\varepsilon_f} = \begin{bmatrix} \Sigma_{\varepsilon_m} & \mathbf{0} \\ \mathbf{0} & \Sigma_{\varepsilon_e} \end{bmatrix}$$

The $N_m \times N_m$-dimensional MEG measurement noise covariance matrix is diagonal and the noise power is assumed to be equal over all MEG channels. It is modeled as shown in the equation below:

$$\Sigma_{\varepsilon_m} = \sigma^2_{\varepsilon_m} I_{N_m}.$$

The same applies to the $N_e \times N_e$-dimensional EEG measurement noise covariance matrix which is shown in the following equation:

$$\Sigma_{\varepsilon_e} = \sigma^2_{\varepsilon_e} I_{N_e}.$$

2.6.2 Grid Choice and the Definition of the Laplacian Matrix

The grid definition is part of the forward solution. It needs to be specified whether a cortical surface mesh or a 3D volumetric grid will be used. Additionally, the grid can include only the brain's gray matter or encompass the whole brain. The spacing of the grid needs to be defined too. Except for the finite-element (FE) head model, all other head models that are used in this thesis were boundary-element (BE) head models that were generated using the CURRY software [Com11]. Regarding the definition of the Laplacian matrix, the explicit procedure for the calculation of the modified Laplacian matrix was explained in [PM99] after a discussion about the advantages and disadvantages of the classical definition of the Laplacian matrix. The classical definition of the Laplacian matrix always uses six neighbors for each grid point. The definition that uses the actual number of neighbors results in a singular Lalacian matrix. The author of LORETA takes the average of both definitions and creates the modified definition of the Laplacian matrix that results in a non-singular matrix and does not suppress the current density at the grid borders [PM95].

The first step in calculating the Laplacian matrix according to the second definition is to calculate the matrix $[\mathbf{A}_2]_{\acute{v}v}$:

$$[\mathbf{A}_2]_{\acute{v}v} = \begin{cases} 1/6 & \text{if } \|\mathbf{g}_{\acute{v}} - \mathbf{g}_v\| = u \\ 0 & \text{otherwise} \end{cases}$$

where $\mathbf{g}$ is a point in 3D space on the source grid and u is the spacing or resolution of the 3D grid. After that, matrix $\mathbf{A_1}$ is calculated according to the equation below:

$$\mathbf{A}_1 = \frac{1}{2}\left(\mathbf{I}_{N_v} + \left[diag\left(\mathbf{A}_2 \mathbf{1}_{N_v}\right)\right]^{-1}\right)\mathbf{A}_2$$

In the equation below, a matrix, $\mathbf{A}_0$, of dimension $N_j \times N_j$ results from Kronecker multiplication with a 3-dimensional identity matrix:

$$\mathbf{A}_0 = \mathbf{A}_1 \otimes \mathbf{I}_3$$

The $N_j \times N_j$-dimensional modified Laplacian matrix is obtained from the equation:

$$L_{mod} = \frac{6}{u^2}\left(\mathbf{A}_0 - \mathbf{I}_{N_j}\right)$$

2.6.3 Dimensionality Reduction via Spatial Projection (SP)

Spatial projection [LLE$^+$14], a dimensionality reduction approach, was implemented and used in conjunction with the source imaging methods in the open source SPM8 toolbox [LMK$^+$11]. The use of dimensionality reduction approaches may help with problems of noise, numerical stability, and long computational times [HDN14]. We decided to integrate spatial projection, which is based on singular value decomposition, into the STKF algorithm, in order to decrease the computational time and to solve the problem of numerical stability and ghost sources. Spatial projection may be applied to the lead field matrix before or after spatial whitening. Before spatial whitening, the original lead field matrix is used. Singular value decomposition is applied on the matrix $\mathbf{K}\mathbf{K}^\mathsf{T}$ as follows:

$$\mathbf{K}\mathbf{K}^\mathsf{T} = \mathbf{U}\mathbf{S}\mathbf{V}^\mathsf{T}.$$

The matrix $\mathbf{S}$ has monotonically-decreasing singular values on the main diagonal. A threshold value of $1.2 * 10^{-7}$ is then applied in SPM8 as a standard threshold value and only the w singular values above this threshold value will be kept. After truncation of the $\mathbf{S}$ matrix, the left and right matrices of singular vectors will be updated accordingly. Then the left matrix of singular vectors, $\mathbf{U}$, will be used to transform the lead field matrix into an $N_w \times N_j$-dimensional matrix, $\mathbf{K}_{sp}$, as shown in the following equation:

$$\mathbf{K}_{sp} = \mathbf{U}^\mathsf{T}\mathbf{K}.$$

Additionally, the M/EEG data is also transformed into an $N_w \times N_T$-dimensional data, $\mathbf{y}_{sp}$, as follows:

$$\mathbf{y}_{sp} = \mathbf{U}^\mathsf{T}\mathbf{y}.$$

The application of spatial projection prior to spatial whitening may not be very advantageous, since another transformation, namely spatial whitening, follows spatial projection. Additionally, since almost all of the STKF's operations are in the weakly-coupled state-space, the practical lead field matrix for the STKF is the one after spatial whitening. Hence it may be better to perform spatial projection after spatial whitening. After spatial whitening, the Laplacianized lead field matrix $\tilde{\mathbf{K}}$ is used instead of the original lead field matrix in equation 2.6.3. The optimal place for spatial projection in the STKF's pipeline will be investigated in this thesis.

Additionally, different threshold values will be used to understand the effect of the threshold on spatial projection, when it is combined with the STKF.

2.7 Parameter Estimation Using Maximum Likelihood (ML)

Parameter estimation may be performed via maximum likelihood (ML). In order to penalize the models with a high number of parameters, maximum likelihood is performed via minimization of the Akaike information criterion (AIC) [Aka98]. AIC can be expressed by the following equation:

$$\mathrm{AIC}\left(\theta_{KF}\right) = -2\mathscr{L}\left(\theta_{KF}\right) + 2N_{KF},$$

where θ_{KF} is the parameter vector that includes all state-space model parameter and N_{KF} is the number of parameters that are included in θ_{KF}. $\mathscr{L}$ is the natural logarithm of the likelihood function [GYO$^+$04b].

If it was decided that observation scaling parameters were to be used, the vector of state-space model parameters for a simultaneously-measured MEG-EEG dataset, observation scaling parameters, and an AR(2) dynamical model becomes:

$$\theta_{KF} = \left[a_1, a_2, b, s_{y_e}, s_{y_m}, \sigma^2_{\varepsilon e}, \sigma^2_{\varepsilon m},\right]^{\mathsf{T}}.$$

Alternatively, the vector of state-space model parameters for a simultaneously-measured MEG-EEG dataset, an AR(2) dynamical model, and a regional STKF with N_r regions becomes:

$$\theta_{KF} = \left[a_1, a_2, b, \sigma^2_{\eta 1}, \ldots, \sigma^2_{\eta N_r}, \sigma^2_{\varepsilon e}, \sigma^2_{\varepsilon m},\right]^{\mathsf{T}}.$$

The evaluation of AIC is performed here via STKF, since the sensor-space innovations and the innovation covariance matrix are needed to compute the AIC. This can be seen in the equation below:

$$\begin{aligned}\mathrm{AIC}\left(\theta_{KF}\right) = &\sum_{t=1}^{N_T} \left(\log\left|\Sigma_{\mathbf{r}_{y,t}}\right| + \mathbf{r}_{y,t}{}^{\mathsf{T}}\Sigma_{\mathbf{r}_{y,t}}{}^{-1}\mathbf{r}_{y,t}\right)\\ &+ TN_y \log\left(2\pi\right) + 2N_{KF}.\end{aligned}$$

The STKF is called by an optimization algorithm to evaluate the AIC in its search for the set of parameters that minimizes the AIC. A quasi-newton method, the Broyden-Fletcher-Goldfarb-Shanno (BFGS) algorithm, is mainly used for the optimization. The gradient and Hessian of the cost function are numerically evaluated by MATLAB's Optimization Toolbox (Mathworks, Natick, Massachusetts, USA). In order to decrease the probability of staying in a local minimum, the Simplex algorithm is called, but less often so, during the optimization process [GOM$^+$08].

Chapter 3

Source Imaging of Simulated EEG Data via the Spatiotemporal Kalman Filter

3.1 Motivation

In this chapter we would like to understand the different factors that influence the accuracy and spatial resolution of the STKF. Since the current density distribution of real EEG recordings is not known, we will use simulated EEG data. Instead of simulating single dipoles, we agreed with our cooperation partners at "the Epileptogenic Systems: Signals and Models" group, which is part of the Signal and Image Processing Laboratory of the University of Rennes I, to generate for us simulated EEG data using neuronal population models [WBBC00, WHB$^+$05, CRBCW07], which are physiological brain models that belong to the family of neural mass models. We used these data in the first part of this chapter to compare the localization of averaged and non-averaged spikes, gray-matter and full-brain grids, classical and modified Laplacian matrices. Additionally, we wanted to gain insights about the effects of the source area and the number of electrodes on the performance of the STKF, compared to that of LORETA. We hypothesize that full-brain grids will improve the accuracy and decrease the variability of localization in both LORETA and STKF. Additionally we hypothesize that the modified Laplacian matrix will improve the localization of superficial sources since it does not force the current density distribution to be zero at the outer border of the grid. Finally we hypothesize that the STKF will outperform LORETA, especially in model comparison and low-resolution EEG, due to its additional temporal smoothness constraints.

In the second part of this chapter we try to suppress the redundancy in high-resolution EEG via a dimensionality reduction approach, spatial projection, that is available in the SPM software [LMK$^+$11, LLE$^+$14]. Information redundancy may lead to instabilities, especially for dynamical inverse methods, and cause wrong localization and spurious sources. We will investigate first how to integrate spatial projection within the inverse modeling pipeline. After that we will evaluate the improvement in the performance of the Kalman filter due to the application of spatial projection. Finally we will investigate the effect of the threshold of spatial projection on the STKF results. We hypothesize that spatial projection will decrease computational time and lead to stable and more accurate STKF results. Additionally we expect the choice of the threshold to affect the accuracy of the STKF.

3.2 The Influence of Grid Choice, Laplacian Matrix, Number of Electrodes, and Source Area on the Performance of the STKF

EEG source imaging results of the non-averaged spikes, which were generated from sources with 10 cm^2 source area in the lateral frontal and lateral temporal regions, were published by the author in [HAFM$^+$17a]. Only the analyses with full-brain grids and the modified Laplacian matrix and low-resolution EEG datasets of non-averaged spikes were published.

3.2.1 Methods

The simulated EEG data were generated by our cooperation partners at "the Epileptogenic Systems: Signals and Models" group, which is part of the Signal and Image Processing Laboratory of the University of Rennes I, using neuronal population models. They used the individual anatomy from a T1-weighted MRI (1.25 $\times$ 1 mm^3). Three compartments comprising the scalp, outer skull, and inner skull were segmented and meshed with 2440 triangles each. The conductivity values were set to 0.33 S/m, 0.0082 S/m, and 0.33 S/m for the scalp, outer skull, and inner skull, respectively. The segmented cortex was discretized using a cortical mesh of 19626 points and triangulated (ASA software, ANT Neuro, Enschede, the Netherlands). The dipoles were placed in the center of each triangle and the dipole orientation were constrained to the normal direction. After that, 400 s of brain dynamics was generated for different source locations and source areas as described in [CRMB$^+$10]. Model parameters were chosen such that epileptic spikes were generated by the model and the resulting active cortical patches with a source area of 5 cm^2 and brain dynamics were generated once from the frontal lobe and once from the temporal lobe. In the former case, the patch was placed in the left lateral frontal region. The center of the activity was localized in the left middle frontal gyrus. The activity may shift to the superior frontal gyrus with the extension of the source area. The lateral frontal region is relevant in the case of pediatric epilepsy patients. In the latter case, the patch was placed in the lateral temporal region, which is not as common as mesial temporal lobe epilepsies in adults but is still relevant in the case of adult patients of epilepsies. The center of activity was localized in the left superior temporal gyrus. With the increase of the source area, the activity may shift to the middle temporal gyrus. Outside these areas, the model parameters were chosen to generate normal background EEG activity [WBBC00]. The above procedure was repeated in order to generate brain dynamics from cortical patches with a source area of 10 cm^2. The forward problem was solved using the boundary element method as implemented in the OpenMEEG software [GPOC10] and the resulting LFM was multiplied with the brain dynamics to generate four EEG datasets, from two locations and two source areas, using a layout of 128 EEG electrodes. The electrode layout can be seen in Figure 3.1. The EEG data had a sampling frequency of 250 Hz.

In the preprocessing step, the spikes in each dataset were marked based on the signal of the electrode with the strongest spike. For the analysis of non-averaged spikes, a single strong spike from each of the four datasets was selected using visual inspection. The non-averaged spikes from the left lateral frontal and lateral temporal areas are shown in Fig 3.2 and Fig 3.4, respectively. After taking the number of marked spikes in each dataset into consideration, we chose to average 55 spikes in each dataset using CURRY7. The resulting average spikes from the left lateral frontal and lateral temporal regions are displayed in Fig 3.3 and Fig 3.5. For each source area and location, four new datasets were created from the original 128-electrode dataset using standard electrode layouts that are shown in Fig 3.6. The electrodes with the strongest averaged and non-averaged spikes in the resulting 40 datasets with different source locations, areas, and electrode montages are shown in Table 3.4. After spike averaging, we performed separate standardization and average-referencing for each dataset containing a single non-averaged or average spike. Finally, the SNR of each spike was calculated as described in section 2.1.

In the forward modeling step, the standard 3-compartment realistic head model from CURRY7, that was computed using the boundary element method, was used to calculate the LFM. The scalp, outer skull, and inner skull were described by 1065, 1305, and 2286 nodes, respectively. The conductivity values of the aforementioned compartments were set to 0.33 S/m, 0.0042 S/m, and 0.33 S/m, respectively. We note here that the conductivity value for the skull is different from the one used in simulating the EEG data. The brain was discretized using two grids, each with 7 mm grid spacing. The gray-matter grid had 3997 grid points and the full-brain grid had 5058 grid points. EEG source imaging via LORETA and STKF was performed using three models. In the first one the gray-matter grid was used with the classical definition of the Laplacian matrix. In the second model the full-brain grid was used with the classical Laplacian matrix. The third model used the full-brain grid with the modified Laplacian matrix. The dynamical model of the STKF was a first order autoregressive model. The summary of the analysis pipeline is depicted in Fig 3.7. The source imaging results were visualized using the Fieldtrip toolbox [OFMS11] by using linear transformations to match the grids generated by CURRY7 from the standard Colin27 MRI to the same standard MRI in the coordinate system used by Fieldtrip. Any changes in the figures or anatomical labels of the results, compared to the author's previous published work in [HAFM$^+$17a, HAFM$^+$17b], can only be attributed to continuous improvements in the visualization step. The evaluation of the results was performed by comparing the anatomical labels of the maxima of the strongest source from each source imaging result with the labels of the brain region that was used for the simulation. The anatomical automatic labeling (AAL) atlas [TMLP$^+$02] was used to find the anatomical labels. The anatomical regions that correspond to the AAL labels are listed in Table 3.1, Table 3.2, and

Table 3.3.

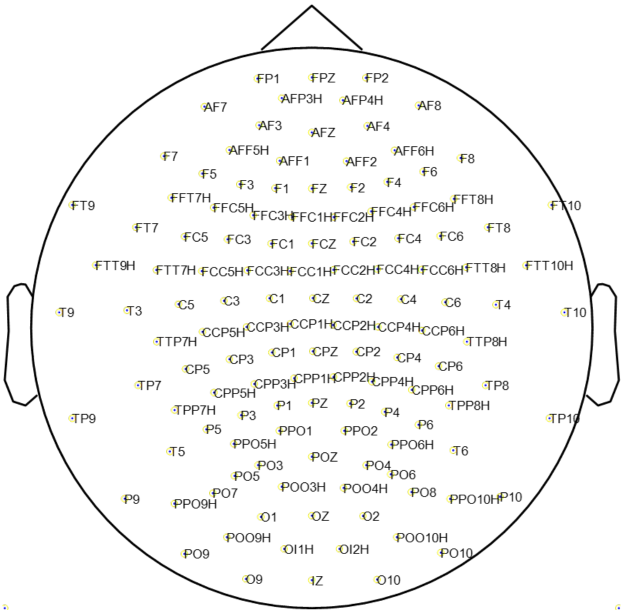

Figure 3.1: *The original 128-channel EEG electrode layout used for generating the EEG datasets from the underlying simulated brain dynamics. The layout was visualized using the Fieldtrip software [OFMS11].*

3.2.2 Results

THE SNR values of both averaged and non-averaged spikes for all electrode layouts, source locations, and source areas are listed in Table 3.4. Regarding the source imaging results, we will start with general observations about the performance of LORETA and STKF. First we observe more lateral results when comparing STKF to LORETA or results from the modified Laplacian to the classical Laplacian matrix. Additionally, STKF results are more focal than those of LORETA. Increasing the number of electrodes leads to more lateral and focal results. The size of the source area did not influence the extension of the estimated current density distribution. Additionally, the AIC results of STKF are lower than those of LORETA. We also observed that, for LORETA results, the ABIC values of the third model were lower than those of the second model except in 5/8 cases when analyzing the 9-electrode datasets. For STKF results, AIC results of the third model were always lower than those of the second model.

The analysis of the average spike from the left lateral frontal region and a source area of 5cm^2 via LORETA, as shown in Fig 3.8, resulted in sources in the lateral frontal region in 3/5 datasets for the first model. The use of the second model resulted in localizations in the desired area in 2/5 datasets. When the third model was used, 3/5 datasets had sources in the target area. Regarding the number of sources in the left lateral frontal area, STKF results, which are summarized in Fig 3.9, were similar to those of LORETA except for the case of the

AAL Atlas labels	corresponding anatomical region	AAL Atlas labels (cont.)	corresponding anatomical region (cont.)
Precentral L	left precentral gyrus	Parietal Sup L	left superior parietal lobule
Precentral R	right precentral gyrus	Parietal Sup R	right superior parietal lobule
Frontal Sup L	left superior frontal gyrus	Parietal Inf L	left inferior parietal lobule
Frontal Sup R	right superior frontal gyrus	Parietal Inf R	right inferior parietal lobule
Frontal Sup Orb L	left superior frontal gyrus, orbital part	SupraMarginal L	left supramarginal gyrus
Frontal Sup Orb R	right superior frontal gyrus, orbital part	SupraMarginal R	right supramarginal gyrus
Frontal Mid L	left middle frontal gyrus	Angular L	left angular gyrus
Frontal Mid R	right middle frontal gyrus	Angular R	right angular gyrus
Frontal Mid Orb L	left middle frontal gyrus, orbital part	Precuneus L	left precuneus
Frontal Mid Orb R	right middle frontal gyrus, orbital part	Precuneus R	right precuneus
Frontal Inf Oper L	left inferior frontal gyrus, pars opercularis	Paracentral Lobule L	left paracentral lobule
Frontal Inf Oper R	right inferior frontal gyrus, pars opercularis	Paracentral Lobule R	right paracentral lobule
Frontal Inf Tri L	left inferior frontal gyrus, pars triangularis	Caudate L	left caudate nucleus
Frontal Inf Tri R	right inferior frontal gyrus, pars triangularis	Caudate R	right caudate nucleus
Frontal Inf Orb L	left inferior frontal gyrus, pars orbitalis	Putamen L	left putamen
Frontal Inf Orb R	right inferior frontal gyrus, pars orbitalis	Putamen R	right putamen
Rolandic Oper L	left Rolandic operculum	Pallidum L	left globus pallidus
Rolandic Oper R	right Rolandic operculum	Pallidum R	right globus pallidus
Supp Motor Area L	left supplementary motor area	Thalamus L	left thalamus

Table 3.1: *Part one of the anatomical descriptions of the labels extracted from the anatomical automatic labeling (AAL) atlas [TMLP^{+}02]*

AAL Atlas labels	corresponding anatomical region	AAL Atlas labels (cont.)	corresponding anatomical region (cont.)
Supp Motor Area R	right supplementary motor area	Thalamus R	right thalamus
Olfactory L	left olfactory cortex	Heschl L	left transverse temporal gyrus
Olfactory R	right olfactory cortex	Heschl R	right transverse temporal gyrus
Frontal Sup Medial L	left medial frontal gyrus	Temporal Sup L	left superior temporal gyrus
Frontal Sup Medial R	right medial frontal gyrus	Temporal Sup R	right superior temporal gyrus
Frontal Med Orb L	left medial orbitofrontal cortex	Temporal Pole Sup L	left superior temporal pole
Frontal Med Orb R	right medial orbitofrontal cortex	Temporal Pole Sup R	right superior temporal pole
Rectus L	left gyrus rectus	Temporal Mid L	left middle temporal gyrus
Rectus R	right gyrus rectus	Temporal Mid R	right middle temporal gyrus
Insula L	left insula	Temporal Pole Mid L	left middle temporal pole
Insula R	right insula	Temporal Pole Mid R	right middle temporal pole
Cingulum Ant L	left anterior cingulate gyrus	Temporal Inf L	left inferior temporal gyrus
Cingulum Ant R	right anterior cingulate gyrus	Temporal Inf R	right inferior temporal gyrus
Cingulum Mid L	left midcingulate area	Cerebelum Crus1 L	left crus I of cerebellar hemisphere
Cingulum Mid R	right midcingulate area	Cerebelum Crus1 R	right crus I of cerebellar hemisphere
Cingulum Post L	left posterior cingulate gyrus	Cerebelum Crus2 L	left crus II of cerebellar hemisphere
Cingulum Post R	right posterior cingulate gyrus	Cerebelum Crus2 R	right crus II of cerebellar hemisphere
Hippocampus L	left hippocampus	Cerebelum 3 L	left lobule III of cerebellar hemisphere
Hippocampus R	right hippocampus	Cerebelum 3 R	right lobule III of cerebellar hemisphere
ParaHippocampal L	left parahippocampal gyrus	Cerebelum 4 5 L	left lobule IV, V of cerebellar hemisphere

Table 3.2: *Part two of the anatomical descriptions of the labels extracted from the anatomical automatic labeling (AAL) atlas [TMLP$^+$02]*

AAL Atlas labels	corresponding anatomical region	AAL Atlas labels (cont.)	corresponding anatomical region (cont.)
ParaHippocampal R	right parahippocampal gyrus	Cerebelum 4 5 R	right lobule IV, V of cerebellar hemisphere
Amygdala L	left amygdala	Cerebelum 6 L	left lobule VI of cerebellar hemisphere
Amygdala R	right amygdala	Cerebelum 6 R	right lobule VI of cerebellar hemisphere
Calcarine L	left calcarine sulcus	Cerebelum 7b L	left lobule VIIB of cerebellar hemisphere
Calcarine R	right calcarine sulcus	Cerebelum 7b R	right lobule VIIB of cerebellar hemisphere
Cuneus L	left cuneus	Cerebelum 8 L	left lobule VIII of cerebellar hemisphere
Cuneus R	right cuneus	Cerebelum 8 R	right lobule VIII of cerebellar hemisphere
Lingual L	left lingual gyrus	Cerebelum 9 L	left lobule IX of cerebellar hemisphere
Lingual R	right lingual gyrus	Cerebelum 9 R	right lobule IX of cerebellar hemisphere
Occipital Sup L	left superior occipital gyrus	Cerebelum 10 L	left lobule X of cerebellar hemisphere
Occipital Sup R	right superior occipital gyrus	Cerebelum 10 R	right lobule X of cerebellar hemisphere
Occipital Mid L	left middle occipital gyrus	Vermis 1 2	lobule I, II of vermis
Occipital Mid R	right middle occipital gyrus	Vermis 3	lobule III of vermis
Occipital Inf L	left inferior occipital cortex	Vermis 4 5	lobule IV, V of vermis
Occipital Inf R	right inferior occipital cortex	Vermis 6	lobule VI of vermis
Fusiform L	left fusiform gyrus	Vermis 7	lobule VII of vermis
Fusiform R	right fusiform gyrus	Vermis 8	lobule VIII of vermis
Postcentral L	left postcentral gyrus	Vermis 9	lobule IX of vermis
Postcentral R	right postcentral gyrus	Vermis 10	lobule X of vermis

Table 3.3: *Part three of the anatomical descriptions of the labels extracted from the anatomical automatic labeling (AAL) atlas [TMLP^{+}02]*

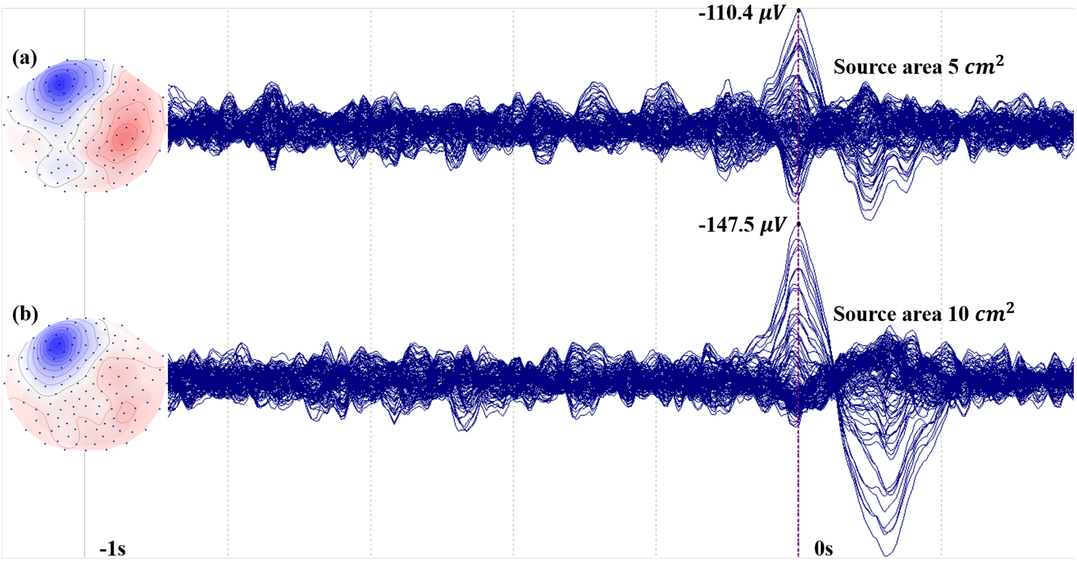

Figure 3.2: *In this figure the non-averaged spikes selected from (a) the EEG dataset, which was generated from the left lateral frontal source with 5 cm^2 source area, and (b) the EEG dataset, which was generated from the left lateral frontal source with 10 cm^2 source area, are shown. The EEG amplitudes at the spike peaks are shown next to the peak points. In the left column the voltage maps (negative in red, positive in blue) of the spike peaks of every data set are shown. The images were produced using CURRY7.*

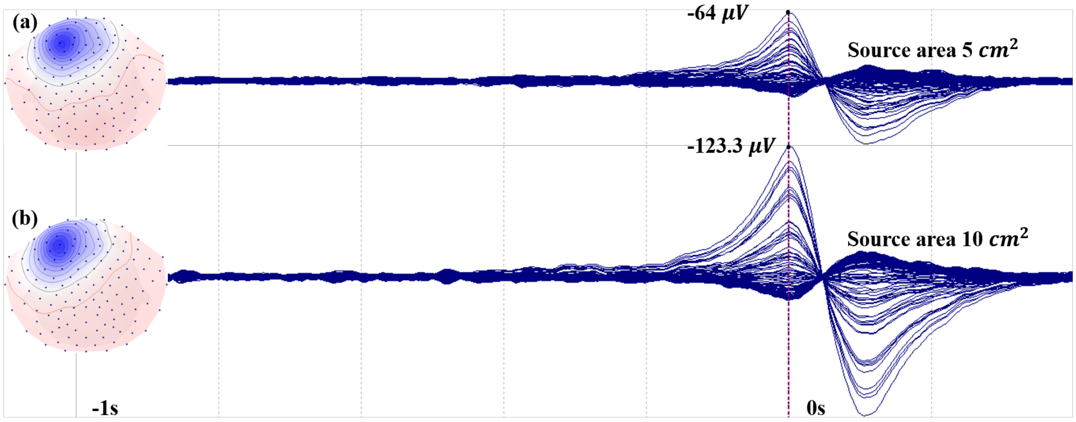

Figure 3.3: *In this figure the averaged spikes computed from (a) the EEG dataset, which was generated from the left lateral frontal source with 5 cm^2 source area, and (b) the EEG dataset, which was generated from the left lateral frontal source with 10 cm^2 source area, are shown. The EEG amplitudes at the spike peaks are shown next to the peak points. In the left column the voltage maps (negative in red, positive in blue) of the spike peaks of every data set are shown. The images were produced using CURRY7.*

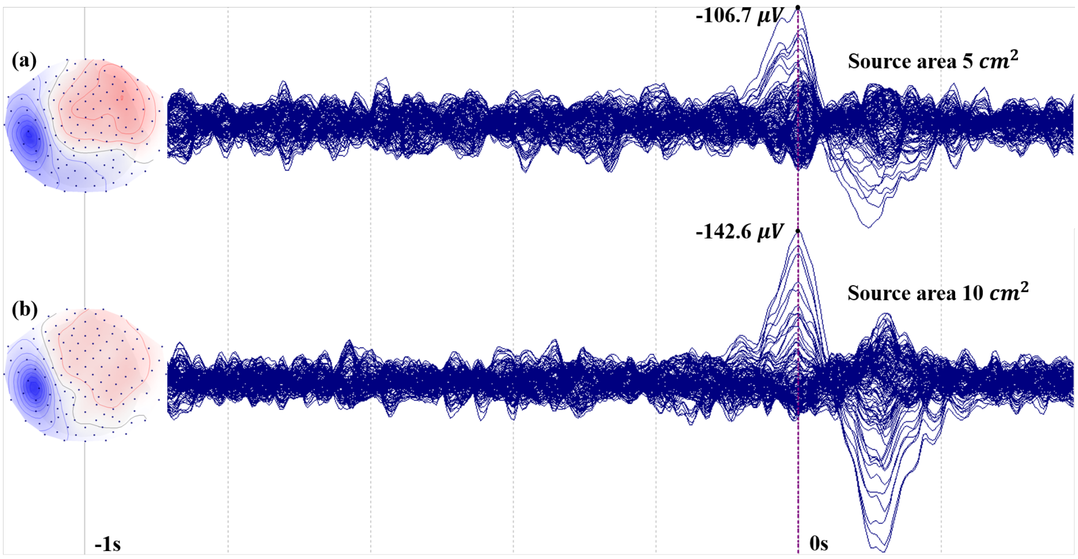

.

__Figure 3.4:__ In this figure the non-averaged spikes selected from (a) the EEG dataset, which was generated from the left lateral temporal source with 5 cm^2 source area, and (b) the EEG dataset, which was generated from the left lateral temporal source with 10 cm^2 source area, are shown. The EEG amplitudes at the spike peaks are shown next to the peak points. In the left column the voltage maps (negative in red, positive in blue) of the spike peaks of every data set are shown. The images were produced using CURRY7.

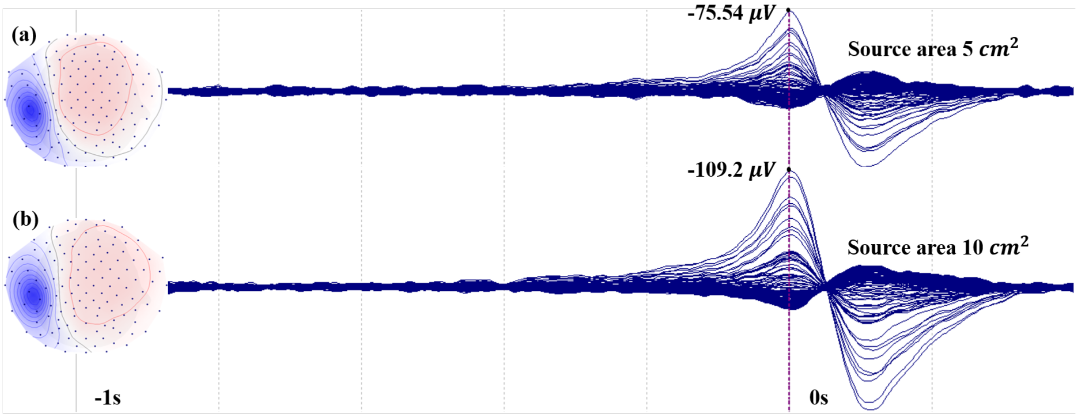

.

__Figure 3.5:__ In this figure the averaged spikes computed from (a) the EEG dataset, which was generated from the left lateral temporal source with 5 cm^2 source area, and (b) the EEG dataset, which was generated from the left lateral temporal source with 10 cm^2 source area, are shown. The EEG amplitudes at the spike peaks are shown next to the peak points. In the left column the voltage maps (negative in red, positive in blue) of the spike peaks of every data set are shown. The images were produced using CURRY7.

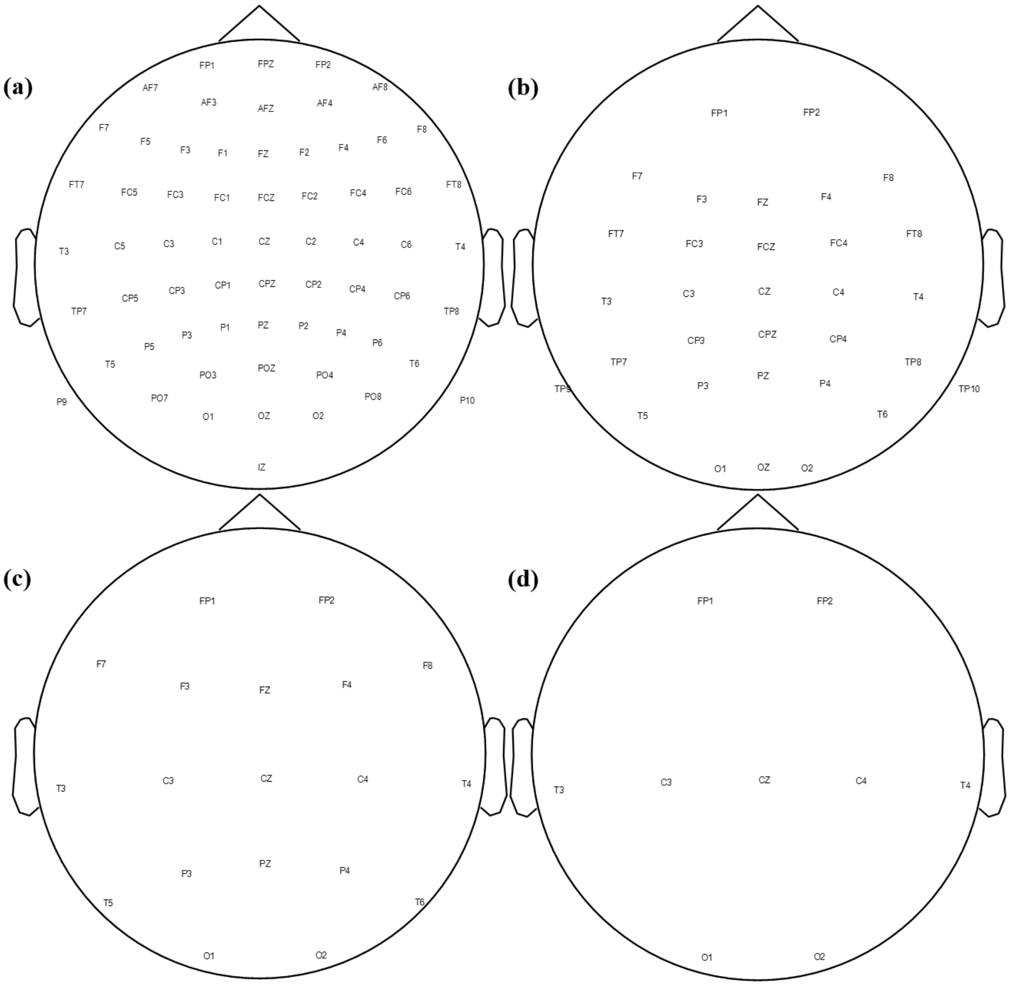

.

Figure 3.6: *Four electrode layouts are shown here which were used to generate the EEG datasets with 64, 32, 19, and 9 electrodes from the original 128-electrode dataset. The layouts were visualized using the Fieldtrip Software [OFMS11].*

Spikes	128-electrode dataset	64-electrode dataset	32-electrode dataset	19-electrode dataset	9-electrode dataset
Frontal averaged spike, 5 cm^2 source area	F3 35.9498	F3 36.2119	F3 36.0597	F3 36.1601	Fp1 27.757
Frontal non-averaged spike, 5 cm^2 source area	F3 20.6059	F3 20.519	F3 20.7022	F3 20.6942	Fp1 12.1869
Frontal averaged spike, 10 cm^2 source area	F3 40.7889	F3 40.8961	F3 40.975	F3 40.88	C3 30.3707
Frontal non-averaged spike, 10 cm^2 source area	F3 26.5522	F3 26.4984	F3 26.4877	F3 26.7061	C3 18.7764
Temporal averaged spike, 5 cm^2 source area	TTP7H 38.4502	CP5 39.5918	TP7 37.6187	T7 36.7242	T7 36.8527
Temporal non-averaged spike, 5 cm^2 source area	TTP7H 15.9484	TP7 17.3833	TP7 17.2830	T7 19.1365	T7 17.0013
Temporal averaged spike, 10 cm^2 source area	TTP7H 37.0488	CP5 37.7073	TP7 37.4095	T7 38.9171	T7 39.0938
Temporal non-averaged spike, 10 cm^2 source area	CP5 22.5361	CP5 22.5282	TP7 18.0671	P7 19.3726	T7 16.5478

Table 3.4: *The dominant electrodes and SNR values (in dB) for both averaged and non-averaged simulated spikes are shown for different electrode layouts, locations, and source areas.*

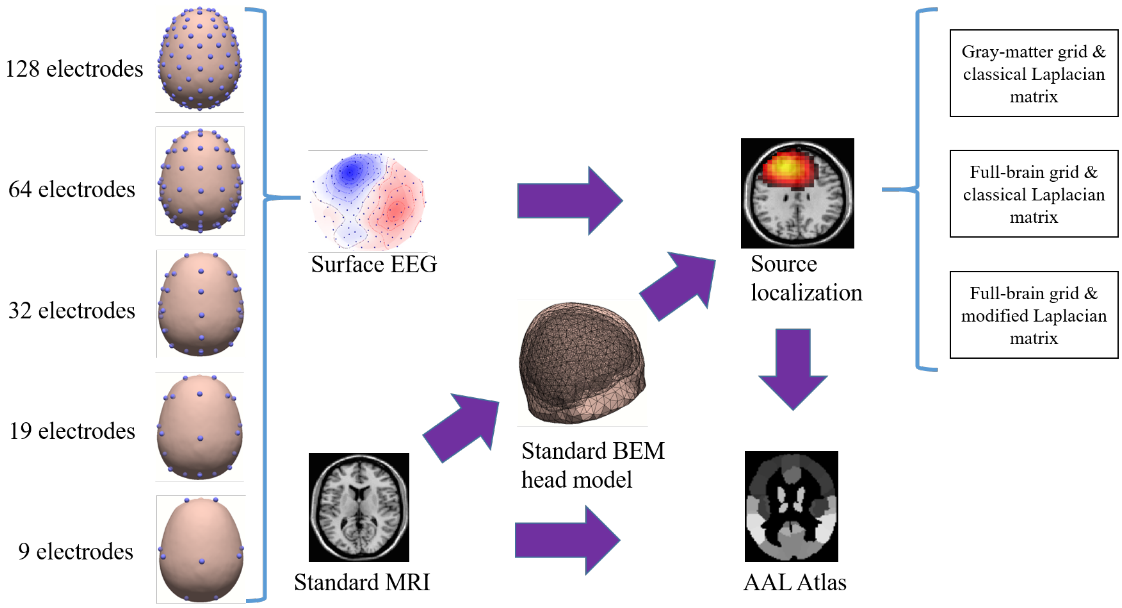

Figure 3.7: *An overview of the analysis pipeline is displayed which includes EEG preprocessing, creation of EEG datasets with 64, 32, and 19 channels based on standard electrode layouts, head modeling, source imaging via LORETA and STKF, and evaluation based on an anatomical atlas. The images were produced using CURRY7.*

second model, where sources fell within the desired region in 3/5 datasets. Table 3.5 collects the anatomical labels of the strongest sources, result evaluation and AIC values produced by both LORETA and STKF.

The analysis of the non-averaged spike from the same region and with the same source area via LORETA resulted in localizations in the left lateral frontal lobe in 3/5, 2/5, and 2/5 datasets for the first, second, and third model, respectively. These results are displayed in Fig 3.10. Analysis via STKF, the results of which are visualized in Fig 3.11, produced sources in the target area in 3/5, 1/5, and 1/5 datasets in the case of the first, second, and third models, respectively. The anatomical labels of the strongest sources, result evaluation and AIC values produced by both LORETA and STKF are listed in Table 3.6. Regarding the case of the average spike from the left lateral frontal region, all models produce left lateral frontal sources in 3/5 datasets. The source imaging results of LORETA are shown in Fig 3.12 and the STKF results are shown in a similar fashion in Fig 3.13. The anatomical labels of the strongest sources, result evaluation and AIC values produced by both LORETA and STKF are listed in Table 3.7.

A similar result can be observed in the case of the non-averaged spike except for the LORETA result of the second model, where sources were within the desired region in 2/5 datasets. The summary of source imaging results is shown in Fig 3.14 for LORETA and in Fig 3.15 for STKF. The comparison for ABIC and AIC results of LORETA and STKF in addition to the anatomical labels of the sources and the result evaluation are collected in Table 3.8.

The results of the average and non-averaged spikes from the left lateral temporal region are

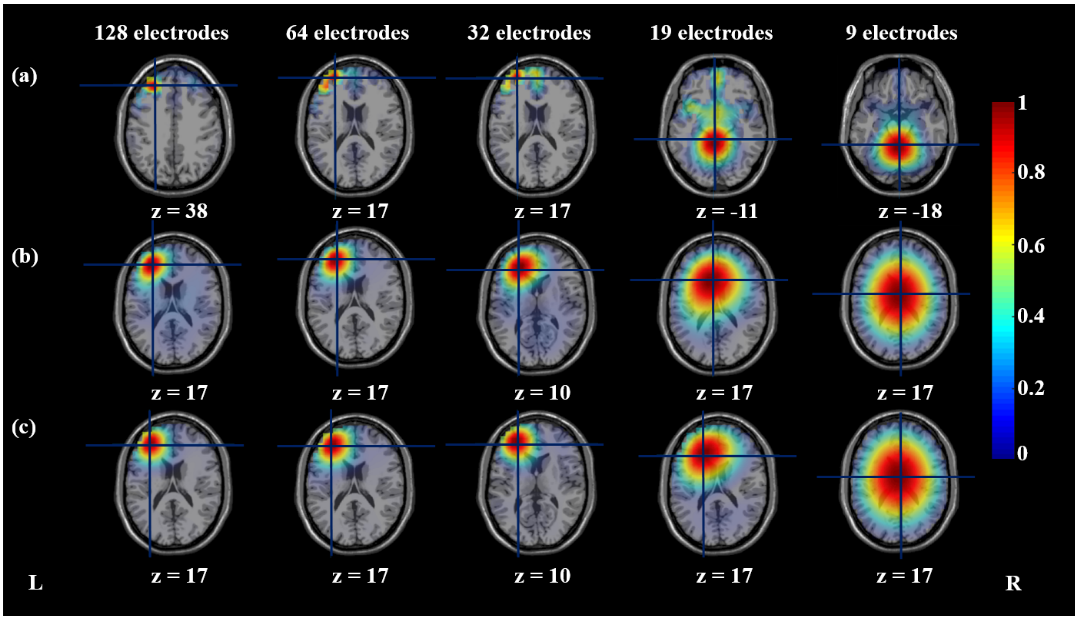

.

Figure 3.8: *EEG source imaging results via LORETA of an averaged spike selected from the EEG dataset, which was generated from the left lateral frontal source with 5 cm^2 source area. LORETA results using a gray-matter 3D grid and the classical Laplacian matrix are depicted in (a). Results using a full-brain 3D grid and the classical Laplacian matrix are shown in (b). For the results shown in (c), a full-brain grid and the modified Laplacian matrix were used. The results from the 128-, 64-, 32-,19-, and 9-electrode datasets are shown in columns 1-5 from the left, respectively. The results are visualized as axial MRI slices at each spike's peak, and the cursor is placed at the maximum of the estimated current density. Additionally the z-coordinates of the axial slices are shown in MNI coordinates. The source imaging results were visualized using the Fieldtrip software [OFMS11]*

Figure 3.9: *EEG source imaging results via STKF of an averaged spike selected from the EEG dataset, which was generated from the left lateral frontal source with 5 cm*^{2} *source area. STKF results using a gray-matter 3D grid and the classical Laplacian matrix are depicted in (a). Results using a full-brain 3D grid and the classical Laplacian matrix are shown in (b). For the results shown in (c), a full-brain grid and the modified Laplacian matrix were used. The results from the 128-, 64-, 32-,19-, and 9-electrode datasets are shown in columns 1-5 from the left, respectively. The results are visualized as axial MRI slices at each spike's peak, and the cursor is placed at the maximum of the estimated current density. Additionally the z-coordinates of the axial slices are shown in MNI coordinates. The source imaging results were visualized using the Fieldtrip software [OFMS11]*

LORETA Results	128 electrodes	64 electrodes	32 electrodes	19 electrodes	9 electrodes
Gray-matter grid and classical Laplacian matrix	Frontal Mid L, Frontal Sup L -C- -19949.5439	Frontal Mid L, Frontal Sup L -C- 11287.4653	Frontal Mid L, Frontal Sup L -C- 16382.1902	Cerebellum 3 L, Cerebellum 4 5 L -DC- 13106.5898	Vermis 3 -DC- 2660.4936
Full-brain grid and classical Laplacian matrix	Frontal Mid L -C- -16372.4339	Frontal Mid L -C- 10255.8855	N \A -DC- 18341.3699	N \A -DC- 12488.6167	N \A -DC- 2501.2472
Full-brain grid and modified Laplacian matrix	Frontal Mid L -C- -19972.9304	Frontal Mid L -C- 10196.2495	Frontal Mid L -C- 16257.3592	N \A -DC- 12101.601	N \A -DC- 2493.3177
STKF Results	128 electrodes	64 electrodes	32 electrodes	19 electrodes	9 electrodes
Gray-matter grid and classical Laplacian matrix	Frontal Mid L, Frontal Sup L -C- -151117.2557	Frontal Mid L, Frontal Sup L -C- -54994.1306	Frontal Mid L, Frontal Sup L -C- -22308.4322	Insula L -DC- -6342.5415	Frontal Med Orb R, Frontal Med Orb L -DC- -3841.8797
Full-brain grid and classical Laplacian matrix	Frontal Mid L -C- -122695.123	Frontal Mid L -C- -44266.4632	Frontal Mid L -C- -17563.9314	N \A -DC- -4883.7989	N \A -DC- -3282.4879
Full-brain grid and modified Laplacian matrix	Frontal Mid L -C- -123658.0525	Frontal Mid L -C- -45930.1798	Frontal Mid L -C- -19427.9677	N \A -DC- -6655.6774	N \A -DC- -3324.6273

Table 3.5: *EEG source imaging results of an averaged spike from an extended source in the left lateral frontal region with a source area of 5* cm^2*. LORETA and STKF results of the spike with 128 electrodes, 64 electrodes, 32 electrodes, 19 electrodes, and 9 electrodes are listed in the table. The results for different grids and Laplacian matrices were visualized at the peak of each spike. For the maximum source activation, anatomical labels from the AAL atlas are shown. If the maximum of the estimated source activity falls within the simulated region, the result is concordant, -C-, with the simulated region; if the maximum does not fall within the simulated region, the result is disconcordant, -DC-, with the simulated region.*

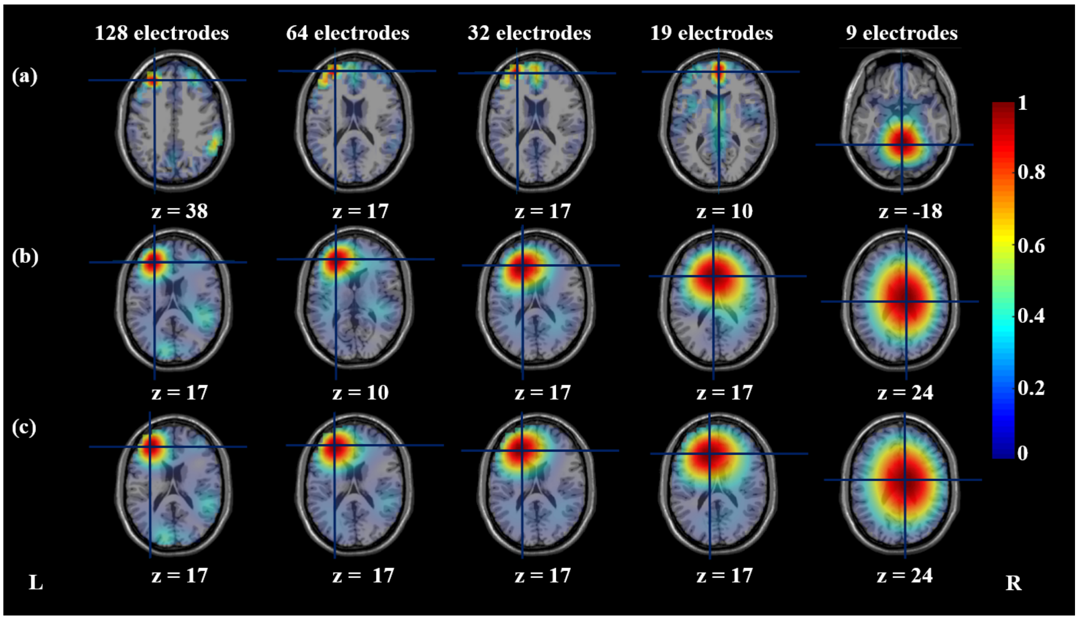

.

Figure 3.10: *EEG source imaging results via LORETA of a non-averaged spike selected from the EEG dataset, which was generated from the left lateral frontal source with 5 cm^2 source area. LORETA results using a gray-matter 3D grid and the classical Laplacian matrix are depicted in (a). Results using a full-brain 3D grid and the classical Laplacian matrix are shown in (b). For the results shown in (c), a full-brain grid and the modified Laplacian matrix were used. The results from the 128-, 64-, 32-,19-, and 9-electrode datasets are shown in columns 1-5 from the left, respectively. The results are visualized as axial MRI slices at each spike's peak, and the cursor is placed at the maximum of the estimated current density. Additionally the z-coordinates of the axial slices are shown in MNI coordinates. The source imaging results were visualized using the Fieldtrip software [OFMS11]*

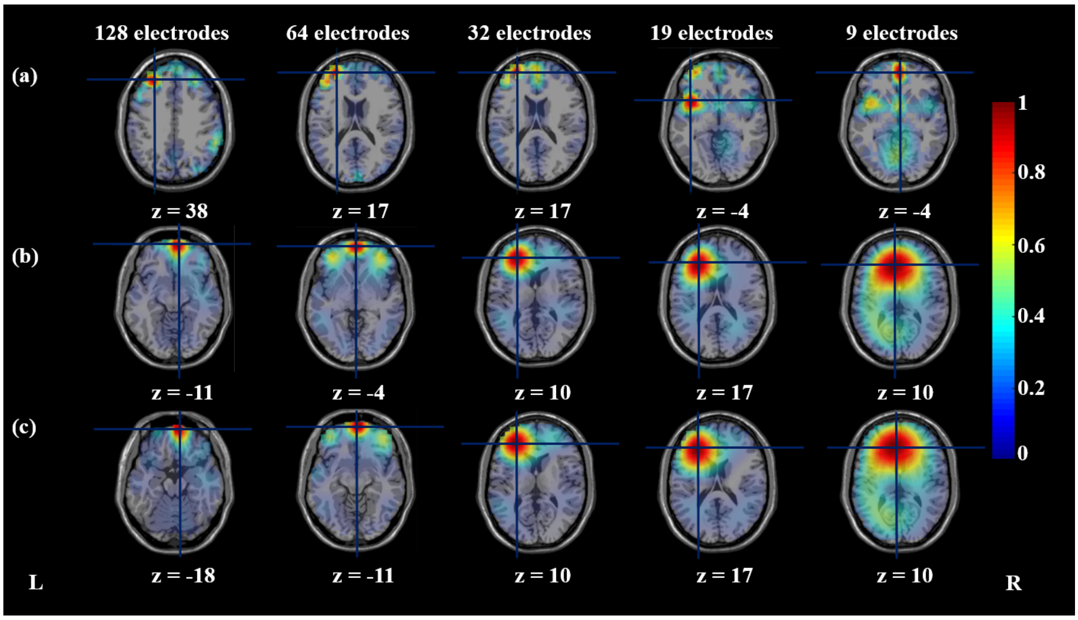

.

Figure 3.11: *EEG source imaging results via STKF of a non-averaged spike selected from the EEG dataset, which was generated from the left lateral frontal source with 5 cm^2 source area. STKF results using a gray-matter 3D grid and the classical Laplacian matrix are depicted in (a). Results using a full-brain 3D grid and the classical Laplacian matrix are shown in (b). For the results shown in (c), a full-brain grid and the modified Laplacian matrix were used. The results from the 128-, 64-, 32-,19-, and 9-electrode datasets are shown in columns 1-5 from the left, respectively. The results are visualized as axial MRI slices at each spike's peak, and the cursor is placed at the maximum of the estimated current density. Additionally the z-coordinates of the axial slices are shown in MNI coordinates. The source imaging results were visualized using the Fieldtrip software [OFMS11]. The results of the analyses with full-brain grids and the modified Laplacian matrix were adapted from figures published by the author in in [HAFM$^+$17b]*

LORETA Results	128 electrodes	64 electrodes	32 electrodes	19 electrodes	9 electrodes
Gray-matter grid and classical Laplacian matrix	Frontal Mid L, Frontal Sup L -C- 4568.3976	Frontal Mid L, Frontal Sup L -C- 17110.0044	Frontal Mid L, Frontal Sup L -C- 15732.7433	Frontal Sup Medial L, Frontal Sup Medial R, Cingulum Ant R -DC- 11780.5786	Vermis 4 5 -DC- 4762.535
Full-brain grid and classical Laplacian matrix	Frontal Mid L -C- 10298.3761	Frontal Mid L -C- 19206.4251	N \A -DC- 16747.9842	N \A -DC- 11399.6198	N \A -DC- 4666.7449
Full-brain grid and modified Laplacian matrix	Frontal Mid L -C- 8480.2076	Frontal Mid L -C- 17749.5825	N \A -DC- 15710.9669	N \A -DC- 11104.0304	N \A -DC- 4665.6518
STKF Results	128 electrodes	64 electrodes	32 electrodes	19 electrodes	9 electrodes
Gray-matter grid and classical Laplacian matrix	Frontal Mid L, Frontal Sup L -C- -58838.4904	Frontal Mid L, Frontal Sup L -C- -15438.3166	Frontal Mid L, Frontal Sup L -C- -4444.9657	Insula L -DC- 850.162	Frontal Med Orb R, Frontal Med Orb L -DC- 866.1855
Full-brain grid and classical Laplacian matrix	Frontal Med Orb R -DC- -38690.4475	Frontal Med Orb R, Frontal Med Orb L -DC- -6078.5028	Frontal Mid L -C- 979.9488	N \A -DC- 2833.1749	Cingulum Ant L -DC- 1357.3347
Full-brain grid and modified Laplacian matrix	Frontal Sup Orb R, Rectus R -DC- -39079.8578	Frontal Med Orb R, Frontal Med Orb L -DC- -7274.2216	Frontal Mid L -C- -376.2588	N \A -DC- 1916.7781	Cingulum Ant L -DC- 1324.926

Table 3.6: *EEG source imaging results of a non-averaged spike from an extended source in the left lateral frontal region with a source area of 5 cm^2. LORETA and STKF results of the spike with 128 electrodes, 64 electrodes, 32 electrodes, 19 electrodes, and 9 electrodes are listed in the table. The results for different grids and Laplacian matrices were visualized at the peak of each spike. For the maximum source activation, anatomical labels from the AAL atlas are shown. If the maximum of the estimated source activity falls within the simulated region, the result is concordant, -C-, with the simulated region; if the maximum does not fall within the simulated region, the result is disconcordant, -DC-, with the simulated region.*

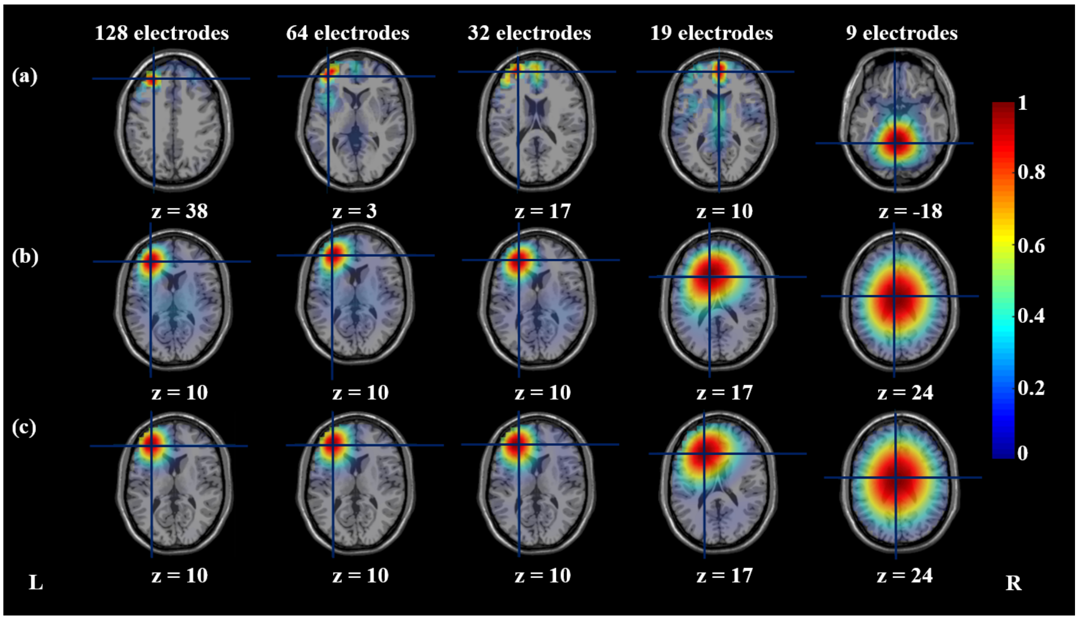

.

Figure 3.12: *EEG source imaging results via LORETA of an averaged spike selected from the EEG dataset, which was generated from the left lateral frontal source with 10 cm^2 source area. LORETA results using a gray-matter 3D grid and the classical Laplacian matrix are depicted in (a). Results using a full-brain 3D grid and the classical Laplacian matrix are shown in (b). For the results shown in (c), a full-brain grid and the modified Laplacian matrix were used. The results from the 128-, 64-, 32-,19-, and 9-electrode datasets are shown in columns 1-5 from the left, respectively. The results are visualized as axial MRI slices at each spike's peak, and the cursor is placed at the maximum of the estimated current density. Additionally the z-coordinates of the axial slices are shown in MNI coordinates. The source imaging results were visualized using the Fieldtrip software [OFMS11]*

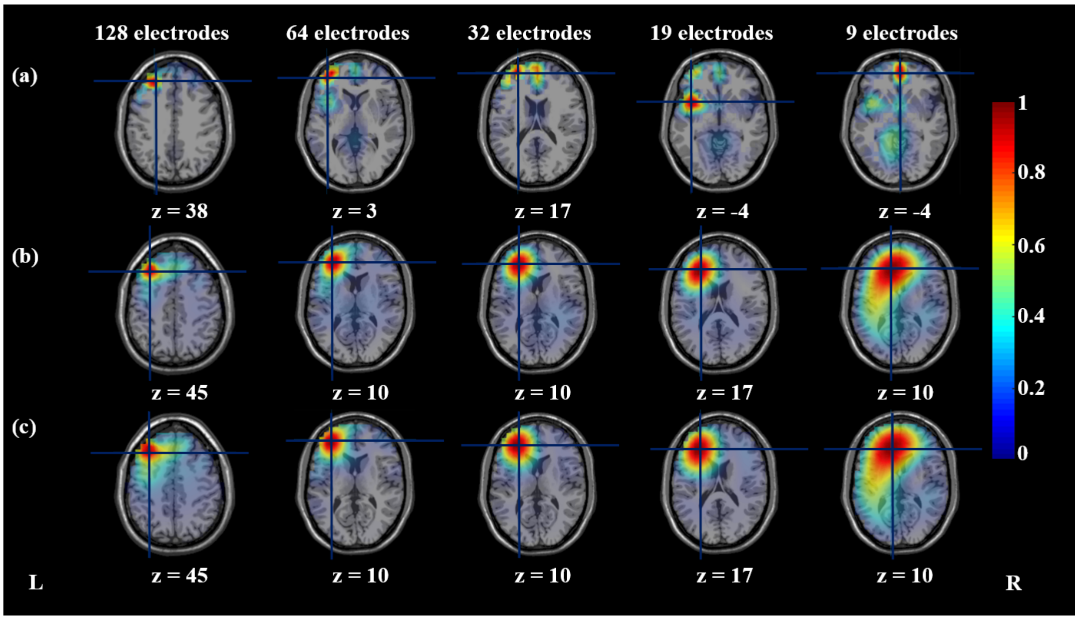

.

Figure 3.13: *EEG source imaging results via STKF of an averaged spike selected from the EEG dataset, which was generated from the left lateral frontal source with 10 cm*^{2} *source area. STKF results using a gray-matter 3D grid and the classical Laplacian matrix are depicted in (a). Results using a full-brain 3D grid and the classical Laplacian matrix are shown in (b). For the results shown in (c), a full-brain grid and the modified Laplacian matrix were used. The results from the 128-, 64-, 32-,19-, and 9-electrode datasets are shown in columns 1-5 from the left, respectively. The results are visualized as axial MRI slices at each spike's peak, and the cursor is placed at the maximum of the estimated current density. Additionally the z-coordinates of the axial slices are shown in MNI coordinates. The source imaging results were visualized using the Fieldtrip software [OFMS11]*

LORETA Results	128 electrodes	64 electrodes	32 electrodes	19 electrodes	9 electrodes
Gray-matter grid and classical Laplacian matrix	Frontal Mid L, Frontal Sup L -C- -29139.7421	Frontal Mid L, Frontal Sup L -C- 5885.4978	Frontal Mid L, Frontal Sup L -C- 13663.1449	Frontal Sup Medial L, Frontal Sup Medial R, Cingulum Ant R -DC- 11119.9447	Cerebellum 4 5 L -DC- 2626.7582
Full-brain grid and classical Laplacian matrix	Frontal Mid L, Frontal Inf Tri L -C- -28515.9316	Frontal Mid L, Frontal Inf Tri L -C- 7076.6196	Frontal Mid L -C- 14179.9941	N \A -DC- 10583.9752	N \A -DC- 2386.6016
Full-brain grid and modified Laplacian matrix	Frontal Mid L, Frontal Inf Tri L -C- -33800.2549	Frontal Mid L, Frontal Inf Tri L -C- 2556.8383	Frontal Mid L -C- 10851.3527	N \A -DC- 10284.9845	N \A -DC- 2385.0676
STKF Results	128 electrodes	64 electrodes	32 electrodes	19 electrodes	9 electrodes
Gray-matter grid and classical Laplacian matrix	Frontal Mid L, Frontal Sup L -C- -179062.1253	Frontal Mid L, Frontal Inf Tri L -C- -73368.8901	Frontal Mid L, Frontal Sup L -C- -28961.5328	Insula L -DC- -5000.4114	L -DC- -3818.5442
Full-brain grid and classical Laplacian matrix	Frontal Mid L -C- -147835.1268	Frontal Mid L, Frontal Inf Tri L -C- -64713.7624	Frontal Mid L -C- -26466.2838	N \A -DC- -4137.7149	N \A -DC- -3442.3585
Full-brain grid and modified Laplacian matrix	Frontal Mid L -C- -149102.4819	Frontal Mid L -C- -67111.3515	Frontal Mid L -C- -29081.9115	N \A -DC- -6013.3998	N \A -DC- -3490.9693

Table 3.7: *EEG source imaging results of an averaged spike from an extended source in the left lateral frontal region with a source area of 10 cm^2. LORETA and STKF results of the spike with 128 electrodes, 64 electrodes, 32 electrodes, 19 electrodes, and 9 electrodes are listed in the table. The results for different grids and Laplacian matrices were visualized at the peak of each spike. For the maximum source activation, anatomical labels from the AAL atlas are shown. If the maximum of the estimated source activity falls within the simulated region, the result is concordant, -C-, with the simulated region; if the maximum does not fall within the simulated region, the result is disconcordant, -DC-, with the simulated region.*

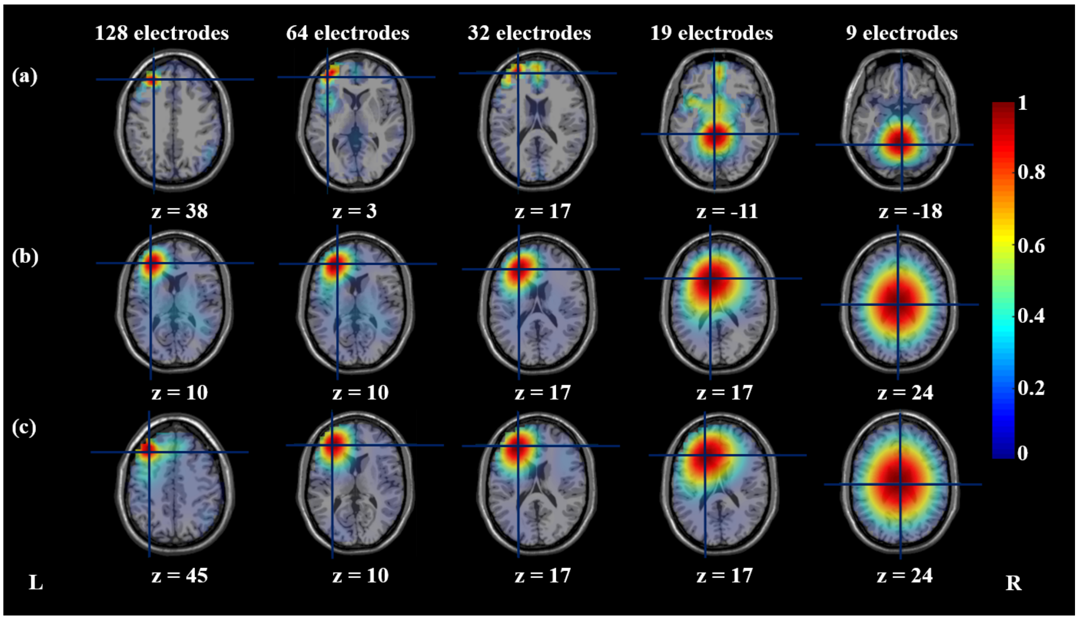

.

Figure 3.14: *EEG source imaging results via LORETA of a non-averaged spike selected from the EEG dataset, which was generated from the left lateral frontal source with 10 cm*^{2} *source area. LORETA results using a gray-matter 3D grid and the classical Laplacian matrix are depicted in (a). Results using a full-brain 3D grid and the classical Laplacian matrix are shown in (b). For the results shown in (c), a full-brain grid and the modified Laplacian matrix were used. The results from the 128-, 64-, 32- ,19-, and 9-electrode datasets are shown in columns 1-5 from the left, respectively. The results are visualized as axial MRI slices at each spike's peak, and the cursor is placed at the maximum of the estimated current density. Additionally the z-coordinates of the axial slices are shown in MNI coordinates. The source imaging results were visualized using the Fieldtrip software [OFMS11]. The figures concerning the analyses with full-brain grids and the modified Laplacian matrix and the low-resolution EEG datasets were adapted from figures published by the author in in [HAFM*$^+$*17a].*

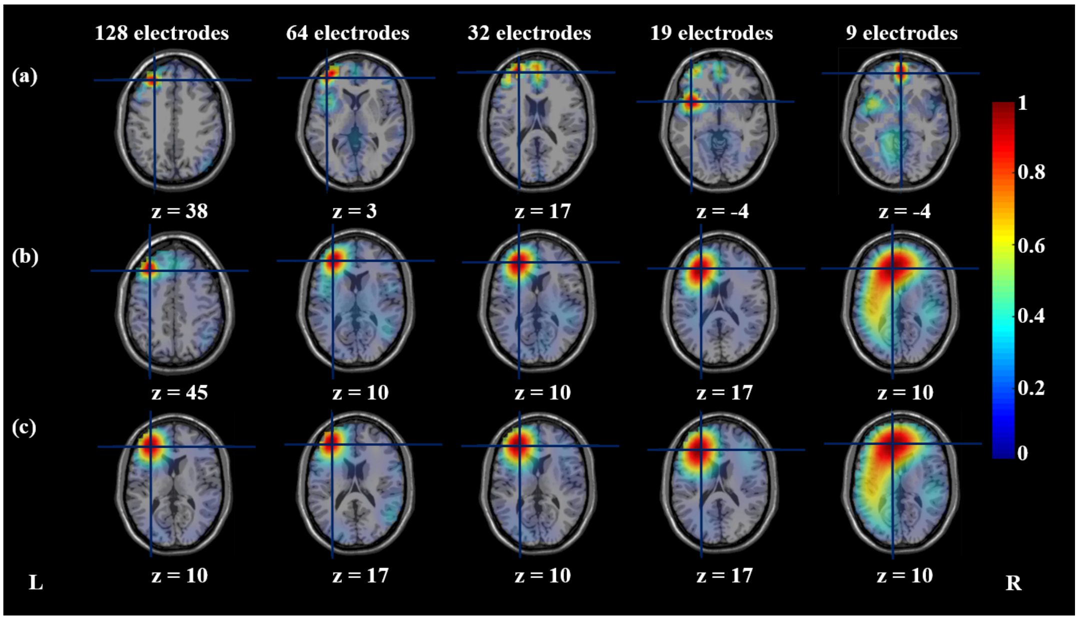

.

Figure 3.15: *EEG source imaging results via STKF of a non-averaged spike selected from the EEG dataset, which was generated from the left lateral frontal source with 10 cm*^{2} *source area. STKF results using a gray-matter 3D grid and the classical Laplacian matrix are depicted in (a). Results using a full-brain 3D grid and the classical Laplacian matrix are shown in (b). For the results shown in (c), a full-brain grid and the modified Laplacian matrix were used. The results from the 128-, 64-, 32-,19-, and 9-electrode datasets are shown in columns 1-5 from the left, respectively. The results are visualized as axial MRI slices at each spike's peak, and the cursor is placed at the maximum of the estimated current density. Additionally the z-coordinates of the axial slices are shown in MNI coordinates. The source imaging results were visualized using the Fieldtrip software [OFMS11]. The figures concerning the analyses with full-brain grids and the modified Laplacian matrix and the low-resolution EEG datasets were adapted from figures published by the author in in [HAFM*$^+$*17a]*

LORETA Results	128 electrodes	64 electrodes	32 electrodes	19 electrodes	9 electrodes
Gray-matter grid and classical Laplacian matrix	Frontal Mid L, Frontal Sup L -C- 8807.2065	Frontal Mid L, Frontal Inf Tri L -C- 20201.9113	Frontal Mid L, Frontal Sup L -C- 20855.055	Cerebellum 3 L, Cerebellum 4 5 L -DC- 14424.2014	Vermis 4 5 -DC- 4706.5164
Full-brain grid and classical Laplacian matrix	Frontal Mid L, Frontal Inf Tri L -C- 13234.7786	Frontal Mid L -C- 22160.9818	N \A – DC – 22848.1733	N \A – DC – 13966.7827	N \A – DC – 4570.0961
Full-brain grid and modified Laplacian matrix	Frontal Mid L, Frontal Inf Tri L -C- 10524.2753	Frontal Mid L, Frontal Inf Tri L -C- 19735.9085	Frontal Mid L -C- 20903.3721	N \A – DC – 13721.0513	N \A – DC – 4570.6438
STKF Results	128 electrodes	64 electrodes	32 electrodes	19 electrodes	9 electrodes
Gray-matter grid and classical Laplacian matrix	Frontal Mid L, Frontal Sup L -C- -66252.1382	Frontal Mid L, Frontal Inf Tri L -C- -16347.6497	Frontal Mid L, Frontal Sup L -C- -5846.2408	Insula L -DC- 602.5023	Frontal Med Orb R, Frontal Med Orb L -DC- 499.8804
Full-brain grid and classical Laplacian matrix	Frontal Mid L -C- -44812.8137	Frontal Mid L, Frontal Inf Tri L -C- -6946.6311	Frontal Mid L -C- 708.7411	N \A – DC – 2680.5676	N \A – DC – 1013.0905
Full-brain grid and modified Laplacian matrix	Frontal Mid L -C- -45199.7083	Frontal Mid L -C- -8292.6244	Frontal Mid L -C- -942.0896	N \A – DC – 1786.2139	Cingulum Ant L -DC- 975.6061

Table 3.8: *EEG source imaging results of a non-averaged spike from an extended source in the left lateral frontal region with a source area of 10 cm*^{2}*. LORETA and STKF results of the spike with 128 electrodes, 64 electrodes, 32 electrodes, 19 electrodes, and 9 electrodes are listed in the table. The results for different grids and Laplacian matrices were visualized at the peak of each spike. For the maximum source activation, anatomical labels from the AAL atlas are shown. If the maximum of the estimated source activity falls within the simulated region, the result is concordant, -C-, with the simulated region; if the maximum does not fall within the simulated region, the result is disconcordant, -DC-, with the simulated region.*

similar with respect to the number of sources in each model that was localized in the left lateral temporal area. LORETA, the results of which for the average spike are shown in Fig 3.16 and for the non-averaged spike are shown in Fig 3.18, in combination with the first, second, and third models resulted in sources in the desired region for 2/5, 3/5, and 3/5 datasets, respectively. The results of STKF are visualized in Fig 3.17 and in Fig 3.19. STKF showed left lateral temporal sources in 2/5, 4/5, and 4/5 datasets for the first, second, and third model, respectively. Anatomical labels, AIC values, and result evaluation are documented in Table 3.9 and in Table 3.10 for the average and non-averaged spikes, respectively.

The anatomical labels and AIC comparison results of the temporal spikes with a source area of 10cm^2 are listed in Table 3.11 for the average spike. A similar table is shown in Table 3.12 for the non-averaged spike. The results of STKF are similar for both average and non-averaged spikes with respect to the number of sources localized in the desired region. Fig 3.21 shows the STKF results for the average spike in conjunction with all three models. Similarly Fig 3.23 summarizes the STKF results of all models for the single spike. STKF produced sources in the target area in 1/5, 4/5, and 4/5 datasets for the first, second, and third models, respectively. EEG source imaging of the average spike via LORETA, the results of which are shown in Fig 3.20, together with the first, second, and third models estimated activity in the left lateral temporal area in 1/5, 3/5, and 3/5 datasets. The analysis of the non-averaged spike via LORETA resulted in reconstructed activity in the target area in 0/5, 2/5, and 2/5 datasets as can be seen in Fig 3.22.

3.2.3 Discussion

The results of the 128-electrode datasets for the average spike across all methods and models were concordant with the simulated region. For the non-averaged spike the results were correct except for one case by LORETA and two cases by STKF. The STKF produced wrong results in these two cases for the second and third models. The strongest sources were localized in the wrong area and ghost sources were present. We suspect that, in this case, information redundancy was responsible for the instability and wrong localization results. In the second part of this chapter, we will test a solution to this problem with the STKF that uses a dimensionality reduction approach based on singular value decomposition (SVD).The numerical problems may have been made worse by the use of the real number of neighbors for each voxel in the STKF's prediction model instead of the more common number of six neighbors for each and every voxel.

The results of the 64-electrode dataset in the lateral frontal area had correct localization results except for the same two cases that caused the instability problem for the STKF with the 128-electrode dataset. For the lateral temporal area, wrong results were found for the first model with the spike generated by the source with 10cm^2 source area across both methods. This may have been caused by the thin sampling of the gray-matter grid and the disadvantage of the classical Laplacian matrix for lateral brain sources.

The results of the 32-electrode dataset with LORETA for the average spike were mostly better than those of the non-averaged spike. STKF showed accurate sources for the left frontal

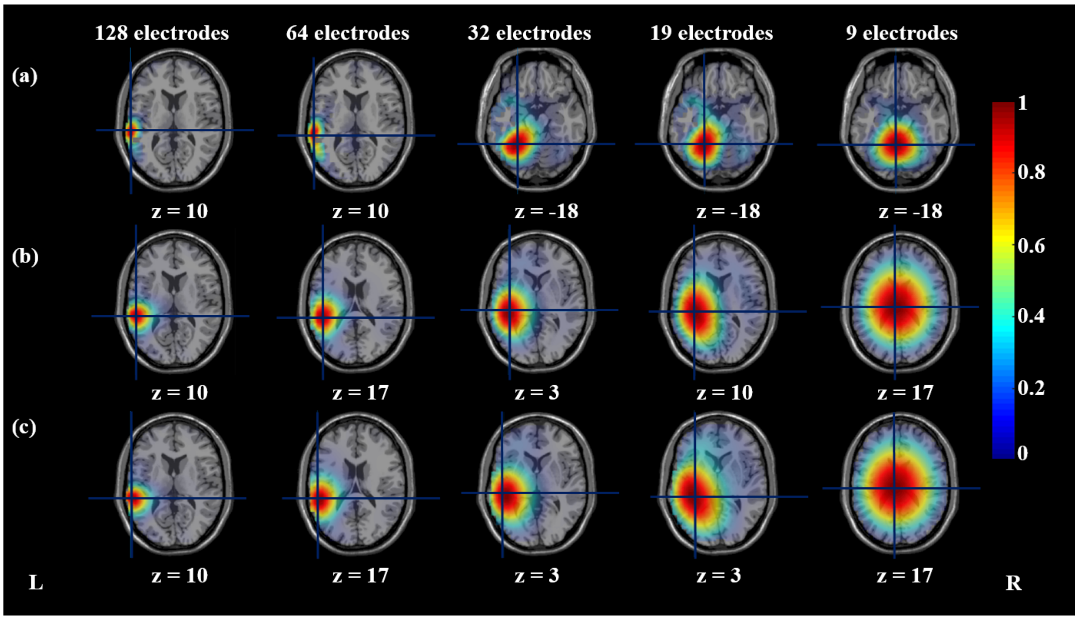

.

Figure 3.16: *EEG source imaging results via LORETA of an averaged spike selected from the EEG dataset, which was generated from the left lateral temporal source with 5 cm^2 source area. LORETA results using a gray-matter 3D grid and the classical Laplacian matrix are depicted in (a). Results using a full-brain 3D grid and the classical Laplacian matrix are shown in (b). For the results shown in (c), a full-brain grid and the modified Laplacian matrix were used. The results from the 128-, 64-, 32-,19-, and 9-electrode datasets are shown in columns 1-5 from the left, respectively. The results are visualized as axial MRI slices at each spike's peak, and the cursor is placed at the maximum of the estimated current density. Additionally the z-coordinates of the axial slices are shown in MNI coordinates. The source imaging results were visualized using the Fieldtrip software [OFMS11]*

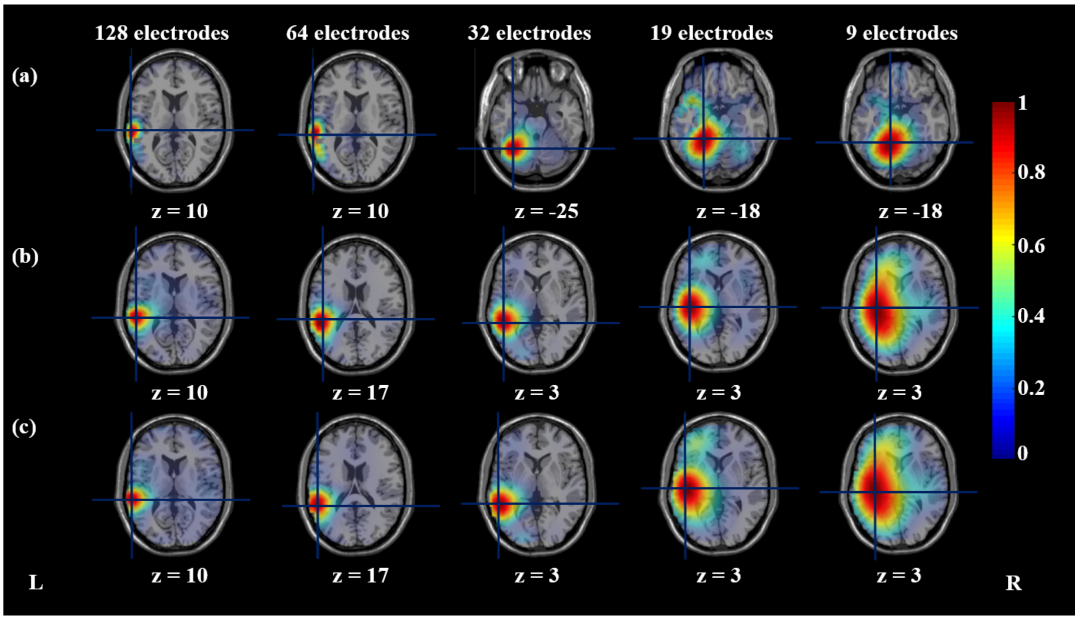

.

Figure 3.17: *EEG source imaging results via STKF of an averaged spike selected from the EEG dataset, which was generated from the left lateral temporal source with 5 cm*^{2} *source area. STKF results using a gray-matter 3D grid and the classical Laplacian matrix are depicted in (a). Results using a full-brain 3D grid and the classical Laplacian matrix are shown in (b). For the results shown in (c), a full-brain grid and the modified Laplacian matrix were used. The results from the 128-, 64-, 32-,19-, and 9-electrode datasets are shown in columns 1-5 from the left, respectively. The results are visualized as axial MRI slices at each spike's peak, and the cursor is placed at the maximum of the estimated current density. Additionally the z-coordinates of the axial slices are shown in MNI coordinates. The source imaging results were visualized using the Fieldtrip software [OFMS11]*

LORETA Results	128 electrodes	64 electrodes	32 electrodes	19 electrodes	9 electrodes
Gray-matter grid and classical Laplacian matrix	Temporal Sup L -C- -33648.5165	Temporal Sup L, Temporal Mid L -C- 12210.994	Cerebellum 4 5 L, Cerebellum 6 L, Fusiform L -DC- 14952.5607	Cerebellum 4 5 L -DC- 11400.503	Cerebellum 4 5 L -DC- 6403.9637
Full-brain grid and classical Laplacian matrix	Temporal Sup L, Temporal Mid L -C- -18928.6719	Temporal Sup L -C- 20210.9965	Temporal Sup L -C- 16120.7339	Heschl L -DC- 12184.5321	Thalamus L -DC- 6482.9459
Full-brain grid and modified Laplacian matrix	Temporal Sup L, Temporal Mid L -C- -20325.366	Temporal Sup L -C- 19051.9671	Temporal Sup L -C- 15328.116	N \A -DC- 10961.6683	Thalamus L -DC- 6483.3364
STKF Results	128 electrodes	64 electrodes	32 electrodes	19 electrodes	9 electrodes
Gray-matter grid and classical Laplacian matrix	Temporal Sup L -C- -158830.7183	Temporal Sup L, Temporal Mid L -C- -59484.3757	Cerebellum 6 L -DC- -23105.6241	Cerebellum 4 5 L, Fusiform L -DC- -6615.05	Cerebellum 4 5 L -DC- -2312.8463
Full-brain grid and classical Laplacian matrix	Temporal Sup L, Temporal Mid L -C- -133986.0331	Temporal Sup L -C- -47251.2364	Temporal Mid L -C- -16931.194	Temporal Sup L, Heschl L -C- -4768.3016	Heschl L -DC- -1616.8264
Full-brain grid and modified Laplacian matrix	Temporal Sup L, Temporal Mid L -C- -134933.3738	Temporal Sup L -C- -48962.3283	Temporal Mid L -C- -18493.6083	Temporal Sup L -C- -6007.1941	Heschl L -DC- -1646.8075

Table 3.9: *EEG source imaging results of an averaged spike from an extended source in the left lateral temporal region with a source area of 5 cm^2. LORETA and STKF results of the spike with 128 electrodes, 64 electrodes, 32 electrodes, 19 electrodes, and 9 electrodes are listed in the table. The results for different grids and Laplacian matrices were visualized at the peak of each spike. For the maximum source activation, anatomical labels from the AAL atlas are shown. If the maximum of the estimated source activity falls within the simulated region, the result is concordant, -C-, with the simulated region; if the maximum does not fall within the simulated region, the result is disconcordant, -DC-, with the simulated region.*

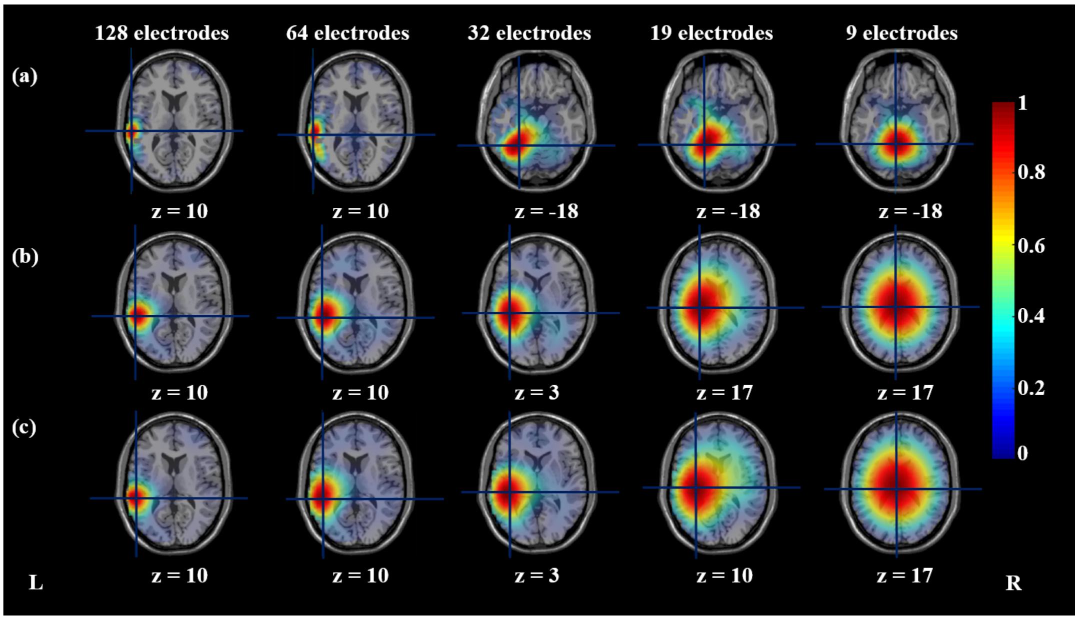

.

Figure 3.18: *EEG source imaging results via LORETA of a non-averaged spike selected from the EEG dataset, which was generated from the left lateral temporal source with 5 cm*^{2} *source area. LORETA results using a gray-matter 3D grid and the classical Laplacian matrix are depicted in (a). Results using a full-brain 3D grid and the classical Laplacian matrix are shown in (b). For the results shown in (c), a full-brain grid and the modified Laplacian matrix were used. The results from the 128-, 64-, 32-,19-, and 9-electrode datasets are shown in columns 1-5 from the left, respectively. The results are visualized as axial MRI slices at each spike's peak, and the cursor is placed at the maximum of the estimated current density. Additionally the z-coordinates of the axial slices are shown in MNI coordinates. The source imaging results were visualized using the Fieldtrip software [OFMS11]*

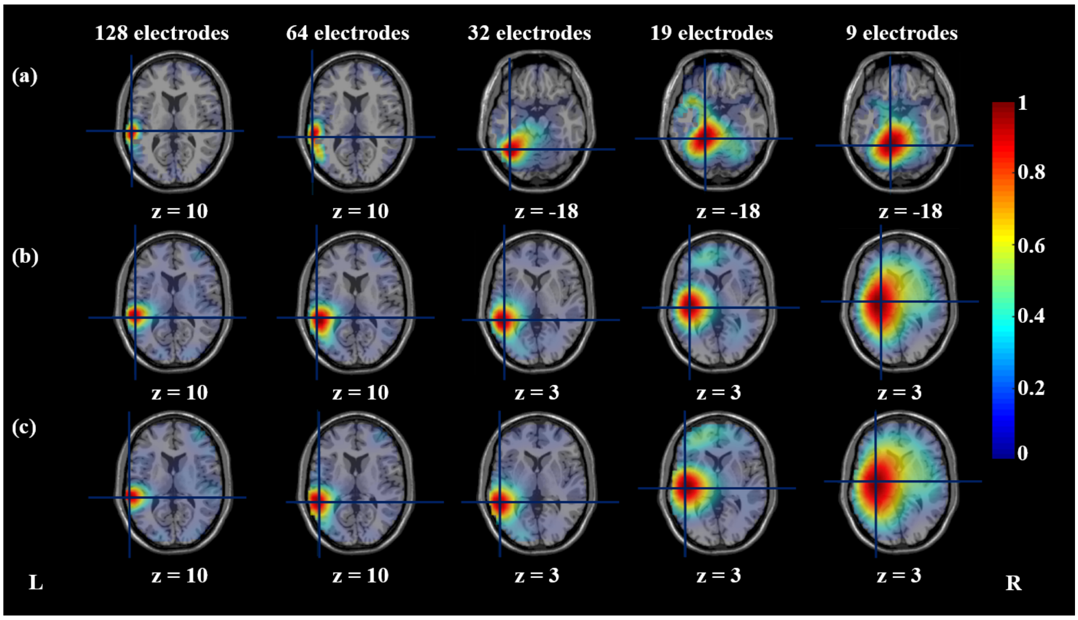

.

Figure 3.19: *EEG source imaging results via STKF of a non-averaged spike selected from the EEG dataset, which was generated from the left lateral temporal source with 5 cm*^{2} *source area. STKF results using a gray-matter 3D grid and the classical Laplacian matrix are depicted in (a). Results using a full-brain 3D grid and the classical Laplacian matrix are shown in (b). For the results shown in (c), a full-brain grid and the modified Laplacian matrix were used. The results from the 128-, 64-, 32-,19-, and 9-electrode datasets are shown in columns 1-5 from the left, respectively. The results are visualized as axial MRI slices at each spike's peak, and the cursor is placed at the maximum of the estimated current density. Additionally the z-coordinates of the axial slices are shown in MNI coordinates. The source imaging results were visualized using the Fieldtrip software [OFMS11]*

LORETA Results	128 electrodes	64 electrodes	32 electrodes	19 electrodes	9 electrodes
Gray-matter grid and classical Laplacian matrix	Temporal Sup L -C- 4610.3893	Temporal Sup L, Temporal Mid L -C- 19029.7184	Cerebellum 4 5 L, Cerebellum 6 L, Fusiform L -DC- 16533.924	Cerebellum 4 5 L -DC- 10618.4805	Cerebellum 4 5 L -DC- 5551.0203
Full-brain grid and classical Laplacian matrix	Temporal Sup L, Temporal Mid L -C- 11976.0254	Temporal Sup L, Temporal Mid L -C- 21946.3698	Temporal Sup L -C- 18006.3745	N \A -DC- 10887.3798	Thalamus L -DC- 5647.4952
Full-brain grid and modified Laplacian matrix	Temporal Sup L, Temporal Mid L -C- 10829.9756	Temporal Sup L, Temporal Mid L -C- 20876.158	Temporal Sup L -C- 16978.513	Insula L, Heschl L -DC- 10489.614	Thalamus L -DC- 5647.8034
STKF Results	128 electrodes	64 electrodes	32 electrodes	19 electrodes	9 electrodes
Gray-matter grid and classical Laplacian matrix	Temporal Sup L -C- -54913.9711	Temporal Sup L, Temporal Mid L -C- -15391.8196	Fusiform L -DC- -4857.8154	Cerebellum 4 5 L, Fusiform L -DC- 588.1541	Cerebellum 4 5 L -DC- 753.0944
Full-brain grid and classical Laplacian matrix	Temporal Sup L, Temporal Mid L -C- -35919.3345	Temporal Sup L, Temporal Mid L -C- -5234.6978	Temporal Mid L -C- 1287.1017	Temporal Sup L, Heschl L -C- 2735.3889	Putamen L, Pallidum L -DC- 1329.0395
Full-brain grid and modified Laplacian matrix	Temporal Sup L, Temporal Mid L -C- -36301.5329	Temporal Sup L, Temporal Mid L -C- -6503.461	Temporal Mid L -C- -172.9175	Temporal Sup L -C- 1932.3703	Insula L -DC- 1297.713

Table 3.10: *EEG source imaging results of a non-averaged spike from an extended source in the left lateral temporal region with a source area of 5 cm*^{2}*. LORETA and STKF results of the spike with 128 electrodes, 64 electrodes, 32 electrodes, 19 electrodes, and 9 electrodes are listed in the table. The results for different grids and Laplacian matrices were visualized at the peak of each spike. For the maximum source activation, anatomical labels from the AAL atlas are shown. If the maximum of the estimated source activity falls within the simulated region, the result is concordant, -C-, with the simulated region; if the maximum does not fall within the simulated region, the result is disconcordant, -DC-, with the simulated region.*

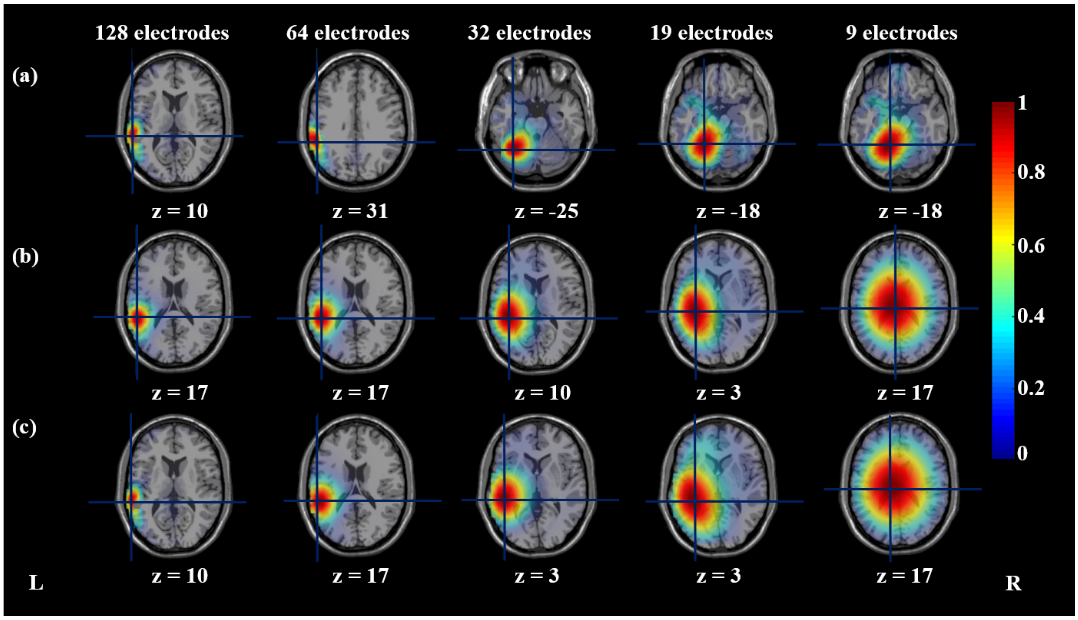

.

Figure 3.20: *EEG source imaging results via LORETA of an averaged spike selected from the EEG dataset, which was generated from the left lateral temporal source with 10 cm^2 source area. LORETA results using a gray-matter 3D grid and the classical Laplacian matrix are depicted in (a). Results using a full-brain 3D grid and the classical Laplacian matrix are shown in (b). For the results shown in (c), a full-brain grid and the modified Laplacian matrix were used. The results from the 128-, 64-, 32-,19-, and 9-electrode datasets are shown in columns 1-5 from the left, respectively. The results are visualized as axial MRI slices at each spike's peak, and the cursor is placed at the maximum of the estimated current density. Additionally the z-coordinates of the axial slices are shown in MNI coordinates. The source imaging results were visualized using the Fieldtrip software [OFMS11]*

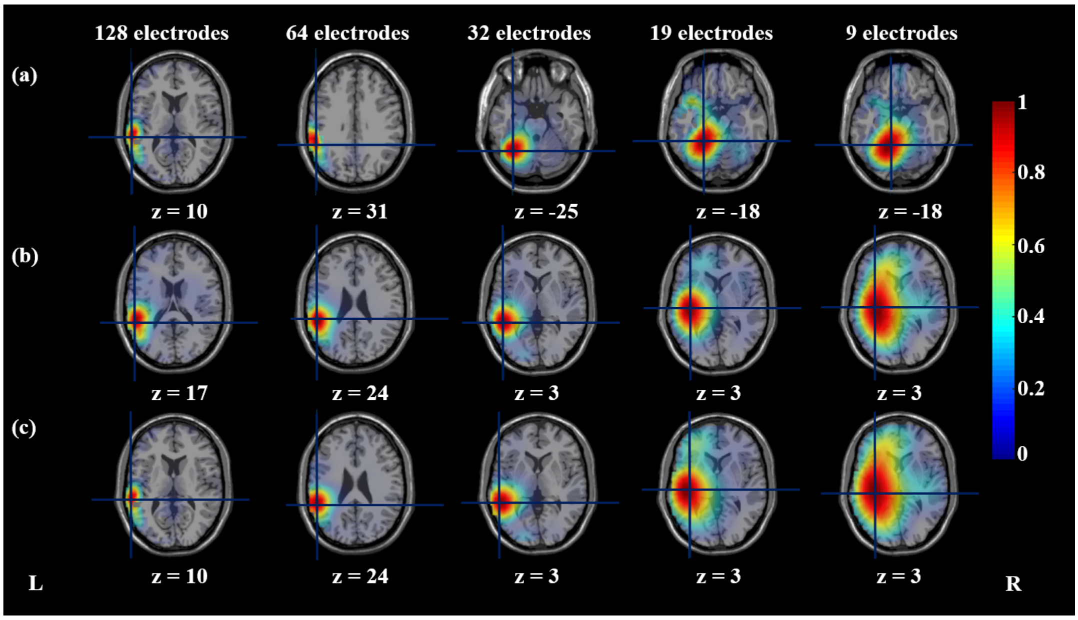

.

Figure 3.21: *EEG source imaging results via STKF of an averaged spike selected from the EEG dataset, which was generated from the left lateral temporal source with 10 cm^2 source area. STKF results using a gray-matter 3D grid and the classical Laplacian matrix are depicted in (a). Results using a full-brain 3D grid and the classical Laplacian matrix are shown in (b). For the results shown in (c), a full-brain grid and the modified Laplacian matrix were used. The results from the 128-, 64-, 32-,19-, and 9-electrode datasets are shown in columns 1-5 from the left, respectively. The results are visualized as axial MRI slices at each spike's peak, and the cursor is placed at the maximum of the estimated current density. Additionally the z-coordinates of the axial slices are shown in MNI coordinates. The source imaging results were visualized using the Fieldtrip software [OFMS11]*

LORETA Results	128 electrodes	64 electrodes	32 electrodes	19 electrodes	9 electrodes
Gray-matter grid and classical Laplacian matrix	Temporal Sup L, Temporal Mid L -C- -48394.7897	Supramarginal L -DC- 8000.0068	Cerebellum 6 L -DC- 13368.819	Cerebellum 4 5 L -DC- 10861.8629	Cerebellum 4 5 L -DC- 6093.9409
Full-brain grid and classical Laplacian matrix	Temporal Sup L -C- -34523.7982	Temporal Sup L -C- 19031.7098	Temporal Sup L -C- 14391.6222	Heschl L -DC- 11620.431	Thalamus L -DC- 6562.3066
Full-brain grid and modified Laplacian matrix	Temporal Sup L, Temporal Mid L -C- -35198.4592	Temporal Sup L -C- 18171.785	Temporal Sup L, Temporal Mid L -C- 13445.7436	N \A -DC- 10496.0427	Thalamus L -DC- 6562.6093
STKF Results	**128 electrodes**	**64 electrodes**	**32 electrodes**	**19 electrodes**	**9 electrodes**
Gray-matter grid and classical Laplacian matrix	Temporal Sup L, Temporal Mid L -C- -189014.3159	Supramarginal L -DC- -72558.7959	Cerebellum 6 L -DC- -27746.9318	Cerebellum 4 5 L, Fusiform L -DC- -8944.1465	Cerebellum 4 5 L -DC- -3114.6007
Full-brain grid and classical Laplacian matrix	Temporal Sup L -C- -164069.4727	Temporal Sup L, Supramarginal L -C- -59984.3882	Temporal Mid L -C- -22036.5176	Temporal Sup L, Heschl L -C- -7304.5565	N \A -DC- -2353.8784
Full-brain grid and modified Laplacian matrix	Temporal Sup L, Temporal Mid L -C- -165083.9879	Temporal Sup L, Supramarginal L -C- -61545.6871	Temporal Mid L -C- -23633.9804	Temporal Sup L, Heschl L -C- -8505.0157	Insula L, Heschl L -DC- -2383.993

Table 3.11: *EEG source imaging results of an averaged spike from an extended source in the left lateral temporal region with a source area of 10 cm^2. LORETA and STKF results of the spike with 128 electrodes, 64 electrodes, 32 electrodes, 19 electrodes, and 9 electrodes are listed in the table. The results for different grids and Laplacian matrices were visualized at the peak of each spike. For the maximum source activation, anatomical labels from the AAL atlas are shown. If the maximum of the estimated source activity falls within the simulated region, the result is concordant, -C-, with the simulated region; if the maximum does not fall within the simulated region, the result is disconcordant, -DC-, with the simulated region.*

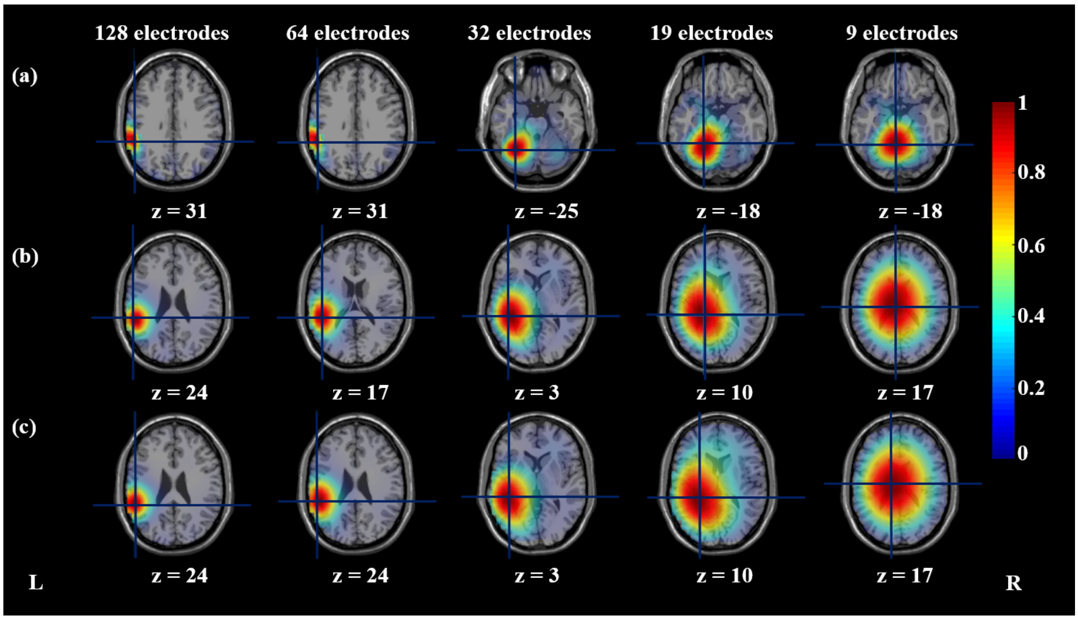

.

Figure 3.22: *EEG source imaging results via LORETA of a non-averaged spike selected from the EEG dataset, which was generated from the left lateral temporal source with 10 cm^2 source area. LORETA results using a gray-matter 3D grid and the classical Laplacian matrix are depicted in (a). Results using a full-brain 3D grid and the classical Laplacian matrix are shown in (b). For the results shown in (c), a full-brain grid and the modified Laplacian matrix were used. The results from the 128-, 64-, 32-,19-, and 9-electrode datasets are shown in columns 1-5 from the left, respectively. The results are visualized as axial MRI slices at each spike's peak, and the cursor is placed at the maximum of the estimated current density. Additionally the z-coordinates of the axial slices are shown in MNI coordinates. The source imaging results were visualized using the Fieldtrip software [OFMS11]. The figures concerning the analyses with full-brain grids and the modified Laplacian matrix and the low-resolution EEG datasets were adapted from figures published by the author in in [HAFM$^+$17a]*

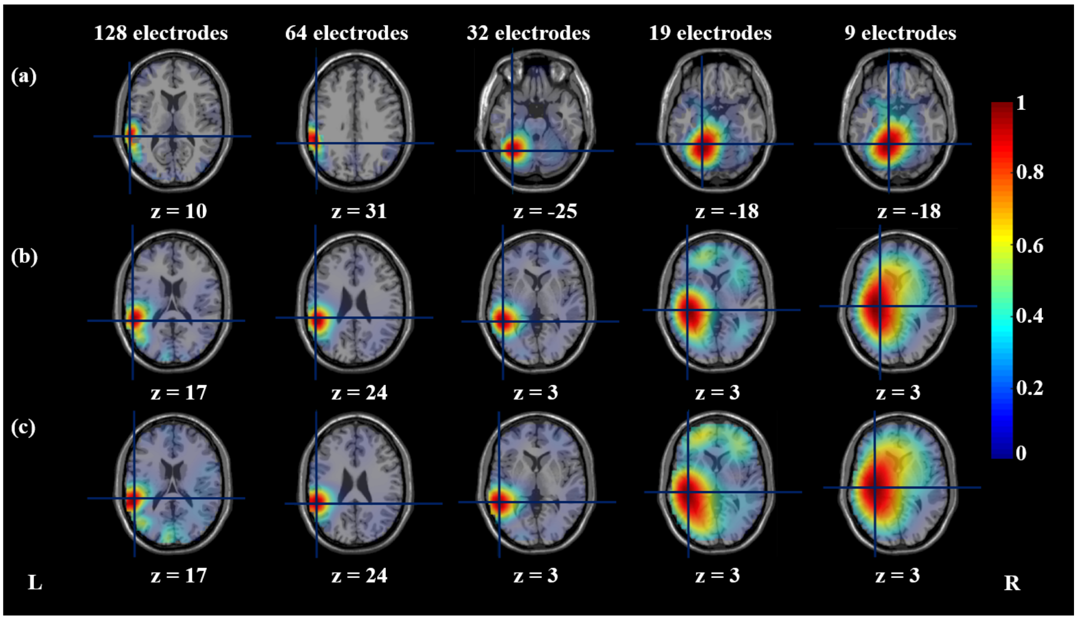

.

Figure 3.23: *EEG source imaging results via STKF of a non-averaged spike selected from the EEG dataset, which was generated from the left lateral temporal source with 10 cm^2 source area. STKF results using a gray-matter 3D grid and the classical Laplacian matrix are depicted in (a). Results using a full-brain 3D grid and the classical Laplacian matrix are shown in (b). For the results shown in (c), a full-brain grid and the modified Laplacian matrix were used. The results from the 128-, 64-, 32-,19-, and 9-electrode datasets are shown in columns 1-5 from the left, respectively. The results are visualized as axial MRI slices at each spike's peak, and the cursor is placed at the maximum of the estimated current density. Additionally the z-coordinates of the axial slices are shown in MNI coordinates. The source imaging results were visualized using the Fieldtrip software [OFMS11]. The figures concerning the analyses with full-brain grids and the modified Laplacian matrix and the low-resolution EEG datasets were adapted from figures published by the author in in [HAFM$^+$17a]*

LORETA Results	128 electrodes	64 electrodes	32 electrodes	19 electrodes	9 electrodes
Gray-matter grid and classical Laplacian matrix	Supramarginal L -DC- 7779.6704	Supramarginal L -DC- 21732.1432	Cerebellum 6 L -DC- 19629.9852	Cerebellum 4 5 L -DC- 13486.8701	Cerebellum 4 5 L -DC- 6708.5435
Full-brain grid and classical Laplacian matrix	Temporal Sup L, Supramarginal L -C- 16925.4685	Temporal Sup L -C- 26240.4157	N \A -DC- 21116.4223	Hippocampus L -DC- 13930.0653	Thalamus L -DC- 6825.9724
Full-brain grid and modified Laplacian matrix	Temporal Sup L, Supramarginal L -C- 15613.0316	Temporal Sup L, Supramarginal L -C- 25190.259	N \A -DC- 20142.2775	N \A -DC- 13468.7672	Thalamus L -DC- 6826.3922
STKF Results	128 electrodes	64 electrodes	32 electrodes	19 electrodes	9 electrodes
Gray-matter grid and classical Laplacian matrix	Temporal Sup L, Temporal Mid L -C- -62851.0645	Supramarginal L -DC- -15503.3826	Cerebellum 6 L -DC- -4717.0806	Cerebellum 4 5 L -DC- 1145.6556	Cerebellum 4 5 L -DC- 1124.3325
Full-brain grid and classical Laplacian matrix	Temporal Sup L -C- -41368.239	Temporal Sup L, Supramarginal L -C- -5423.1516	Temporal Mid L -C- 2100.8592	Temporal Sup L -C- 3707.4609	N \A -DC- 1736.6021
Full-brain grid and modified Laplacian matrix	Temporal Sup L -C- -41833.4802	Temporal Sup L, Supramarginal L -C- -6727.2723	Temporal Mid L -C- 494.1835	Temporal Sup L -C- 2587.2983	Insula L, Heschl L -DC- 1696.9468

Table 3.12: *EEG source imaging results of a non-averaged spike from an extended source in the left lateral temporal region with a source area of 10 cm^2. LORETA and STKF results of the spike with 128 electrodes, 64 electrodes, 32 electrodes, 19 electrodes, and 9 electrodes are listed in the table. The results for different grids and Laplacian matrices were visualized at the peak of each spike. For the maximum source activation, anatomical labels from the AAL atlas are shown. If the maximum of the estimated source activity falls within the simulated region, the result is concordant, -C-, with the simulated region; if the maximum does not fall within the simulated region, the result is disconcordant, -DC-, with the simulated region.*

region. For the left temporal spikes, the STKF results of the first model were wrong. STKF starts to perform better than LORETA with the 32-electrode datasets. LORETA results becomes less focal than those of STKF.

The results of the 19-channel EEG datasets in the lateral frontal lobe via STKF are mostly in the white matter in the direct neighborhood of the gray matter of the target area. We expect that imperfect matching of the analysis and visualization grids during the visualization process may have caused these anatomical labels. LORETA results are further away from the target region and the sources are strongly smeared. The performance of STKF in the left temporal area is even better compared to LORETA.

In the case of the 9-electrode datasets, results of LORETA were always wrong, smeared and shifted to the center of the brain. STKF managed to remain in the same hemisphere and lobe as the target region.

Model comparison favored STKF over LORETA. The STKF outperforms LORETA in case of low-resolution EEG data. This is interesting since many clinics and research centers possess large databases of 32- and 19-electrode data. Wearable EEG, smartphones, and gaming applications may require an even smaller number of EEG electrodes. The results are promising since we are only using a very simple dynamical model with non-adaptive parameters. Since the performance of the Kalman filters improves with better dynamical models, we may have a reliable dynamical inverse solutions that is suitable for low-resolution EEG.

The additional temporal constraints of the STKF and the modified definition of the Laplacian matrix both help to improve the spatial resolution of the estimated brain sources and lead to more focal sources. There is an unavoidable loss of spatial resolution when the number of electrodes is decreased. Investment in better dynamical models of the STKF may help counter this effect.

The count numbers of the sources that were within the desired area showed an improved performance of both LORETA and STKF when the full-brain grid is combined with the modified definition of the Laplacian matrix. This was also revealed by model comparison, especially for STKF. We have not investigated the combination of the modified Laplacian matrix with gray-matter grids that have a higher resolution, which may solve the problem of thin regions. The avoidance of the classical Laplacian matrix may prevent the bias due to the suppression of activity on the inner and outer borders of the grid. The use of thick gray-matter grids may prevent localizations in the white matter or CSF.

The hypotheses were mainly backed by the results. We did not expect spike averaging to be beneficial to the performance of the STKF, since averaging removes a large portion of the interesting dynamics from the signal. Here we did not average hundreds of spikes, so moderate averaging may still be preferable to the analysis of non-averaged spikes via STKF.

This study suffers from some limitations. First we have not quantified the simulated region as a segmented volume and we have not used distance or overlap measures to evaluate the performance of LORETA and STKF. Second we did not analyze multiple spikes from the same area to investigate the consistency of the source analysis results. The analysis of average and non-averaged spikes in addition to the ones generated by sources with different source areas in this study, however, may have been a small step in that direction. In the next chapter we will analyze clinical spikes to try to confirm the results of this chapter using clinical EEG data.

In summary, in this part we investigated for the first time several factors that may influence the performance of STKF, compared to that of LORETA, and studied the grid choice, the Laplacian matrix, spike averaging, and the number of electrodes. The combination of full-brain grids and the modified Laplacian matrix led to the best localization results, spatial resolution, and AIC values. Additionally, STKF was found to be more robust to the reduction in the number of electrodes than LORETA. This result may find applications in the analysis of low-resolution EEG. Moderate spike averaging may improve the results of STKF over those of non-averaged spikes.

3.3 Stabilization of the STKF and Reduction of Computational Time via Dimensionality Reduction

The EEG source imaging results of the non-averaged spikes, which were generated from sources with 5 cm^2 source area in the lateral frontal region, were published by the author in [HAFM$^+$17b]. Only the analyses with full-brain grids and the modified Laplacian matrix were published.

3.3.1 Methods

We perform two experiments in this part. In the first experiment we investigate how to integrate the spatial projection step for the first time within the pipeline of the STKF. We aim at suppressing information redundancy, thus stabilizing the STKF and improving the accuracy of EEG source imaging via STKF. We will comment on any additional benefits of dimensionality reduction via spatial projection regarding computational time and optimization. We would like to answer the question whether we need to apply spatial projection on the LFM before the spatial whitening transformation that is performed on the LFM using the Laplacian matrix or after this transformation. For spatial transformation we will use the standard threshold value of 1.2×10^{-7} that is used in the SPM8 software [LMK$^+$11, LLE$^+$14]. We apply these two scenarios to the 128-electrode preprocessed non-averaged spike from the left lateral frontal region with a source area of 5cm^2. For comparison purposes, we use the results of the 64-electrode, 32-electrode, and 19-electrode datasets from the same spike. In the head modeling step, we use the LFM that was generated for this dataset in section 3.2 of this chapter in addition with the full-brain grid and the modified Laplacian matrix. An overview of the analysis procedure can be seen in Fig 3.24. We are interested in comparing the results of pre-transformation, and post-transformation spatial projection to each other and to the results of 64-electrode, 32-electrode, and 19-electrode datasets with respect to the location of the strongest source and the presence of spurious or ghost sources. Additionally, we count the number of optimization steps until the

AIC value converges and the computational time (s) of a single call of the STKF. MATLAB profiler was used to evaluate the computational time on a 64-bit Windows machine with MATLAB R2011a. The machine had a RAM of 128 GB and the CPU was Intel Xeon E5-2640 v3 with 62.6 GHz.

In the second experiment, we apply post-transformation spatial projection to the 128-electrode dataset using the following threshold values: 10^{-16}, 10^{-15}, 10^{-14}, 10^{-13}, 10^{-12}, 10^{-11}, 10^{-10}, 10^{-9}, 10^{-8}, and 10^{-7}. We are interested in the effect of the choice of the threshold on the accuracy of EEG source imaging via STKF and on the presence of ghost sources. The source imaging results were also visualized using the Fieldtrip toolbox [OFMS11]. Any changes in the figures or anatomical labels of the results, compared to the author's previous published work in [HAFM+17a, HAFM+17b], can only be attributed to continuous improvements in the visualization step.

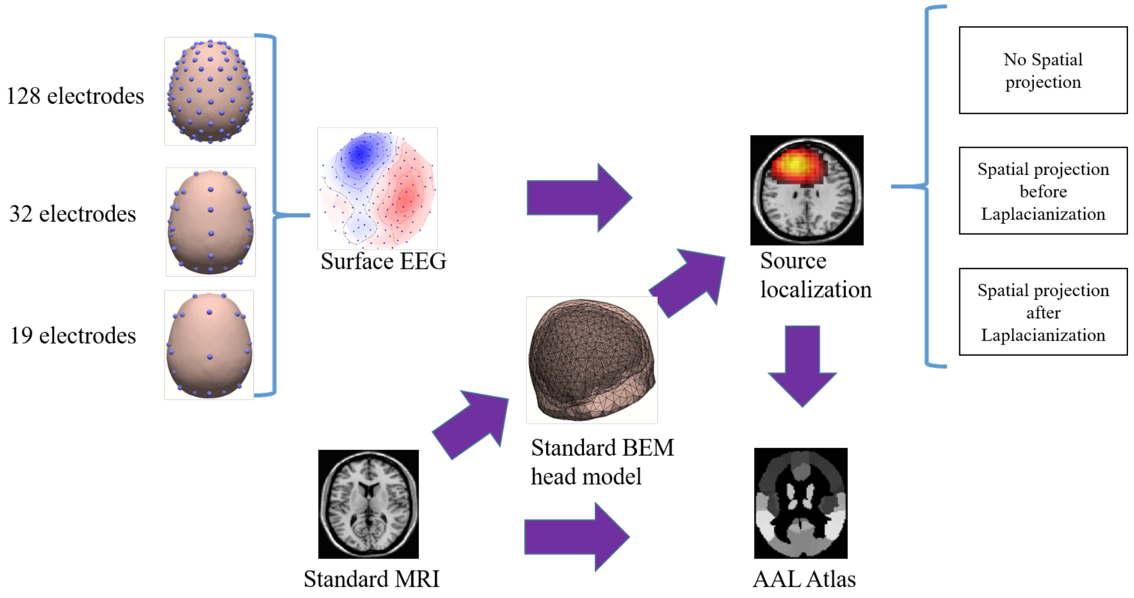

__Figure 3.24:__ A summary of the analysis pipeline is shown which includes EEG preprocessing, head modeling, source imaging via STKF with and without spatial projection, and evaluation based on an anatomical atlas. The images were produced using CURRY7.

3.3.2 Results

The results of the first experiment, compared to the results of STKF without spatial projection, are shown in Fig 3.25. The anatomical labels of each source are listed in Table 3.13. Pre-transformation spatial projection, which resulted in 88 orthogonal channels, produced four sources. The strongest of these sources was localized in the left lateral frontal region. The other three sources were localized in the right frontal and right parietal regions. In contrast, post-transformation spatial projection, which resulted in 26 orthogonal channels, showed a single source in the left lateral frontal region. For the purpose of comparison, the analysis of the 128-electrode dataset without spatial projection resulted in three sources. The strongest of these sources was localized in the right frontal region. The second source was found in the left lateral frontal region. The last source was located again in the right frontal region. The EEG source imaging of the 64-electrode dataset produced two sources. The first source was estimated in the mesial frontal region while the second source was estimated in the left lateral frontal region. Each of the 32-electrode and 19-electrode datasets produced a single source either in the left lateral frontal region, in the case of the former dataset, or in the white matter in the neighborhood of the left lateral frontal area, in the case of the latter dataset.

The results of the comparison of the computational time of a single run of the STKF indicate that the 19-electrode dataset took the lest amount of time followed by the 128-electrode dataset with post-transformation spatial projection, the 32-electrode dataset, the 128-electrode dataset with pre-transformation spatial projection, and the 128-electrode dataset without spatial projection. Regarding the parameter estimation step, the 19-electrode dataset required the smallest number of optimization steps. The 128-electrode datasets with pre- and post-transformation spatial projection in addition to the 32-electrode dataset required a slightly larger number of optimization steps. The 128-electrode dataset without spatial projection required the largest number of optimization steps. The results regarding the computational times and number of optimization steps are summarized in Table 3.14.

The results of the second experiment are shown in Fig 3.26. The anatomical labels of the strongest source and the resulting number of orthogonal channels are listed in Table 3.15. The following threshold values resulted in a single source in the left lateral frontal area with no ghost sources: 10^{-10}, 10^{-9}, 10^{-8}, and 10^{-7}. Each of the threshold values of 10^{-16}, 10^{-15}, 10^{-14}, 10^{-13}, 10^{-12}, and 10^{-11} produced the strongest source in the right frontal, right frontal, right frontal, left lateral frontal, right parietal, and left occipital regions, respectively. Additionally, the analyses using the last six threshold values showed ghost sources in addition to the strongest source.

3.3.3 Discussion

In this dataset, the use of high-resolution EEG with 128 and 64 electrodes to measure the activity of a small region in the brain with a source area of 5cm^2, a very small area, may have introduced information redundancy due to the decrease of distance between measurement points and the increase in regional correlations [LLE+14]. Additionally the small source area in combination with more electrodes decreases the SNR of the desired signal and increases the unwanted behavior of algorithms due to the presence of more noise. We suppressed information redundancy by using dimensionality reduction. In addition to redundancy removal, the application of dimensionality reduction, in the field of signal processing, may solve the issues caused by noise, numerical instabilities, and large computation times [HDN14].

The results of the first experiment show that both pre- and post-transformation spatial pro-

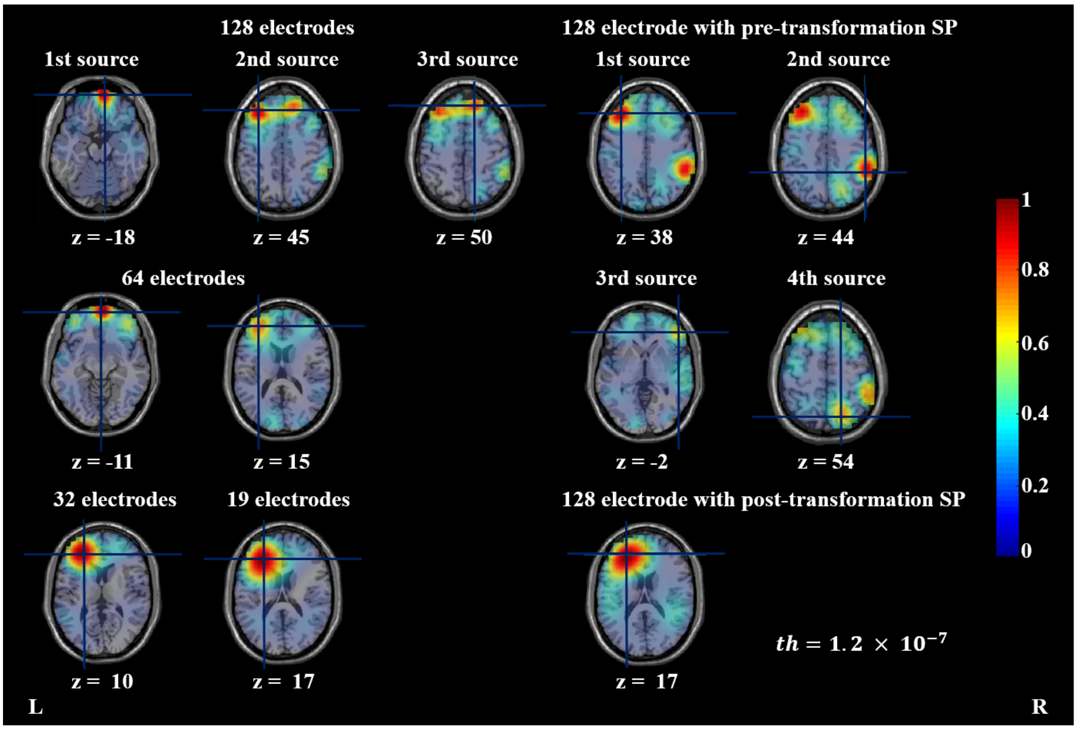

.

Figure 3.25: *EEG source imaging results of a non-averaged spike, which was generated from the left lateral frontal source with 5 cm^2 source area. In the top row to the left the results of the 128-electrode EEG dataset without spatial projection are shown. The results of the 64-electrode dataset are shown in the middle row to the left. The reconstructed sources from the 32- and 19-electrode datasets are shown in the bottom row to the left. In the first two rows to the right the results of the 128-electrode EEG dataset with pre-transformation spatial projection are shown. In the bottom row to the right the reconstructed activity from the 128-electrode EEG dataset with post-transformation spatial projection is displayed. The results are visualized as axial MRI slices at each spike's peak, and the cursor is placed at the maximum of the estimated current density. Additionally the z-coordinates of the axial slices are shown in MNI coordinates. The source imaging results were visualized using the Fieldtrip software [OFMS11]. The figure was adapted from a previous publication by the author [HAFM$^+$17b]*

EEG Datasets	First source	Second source	Third Source	Fourth Source
128-electrode dataset	Frontal Sup Orb R, Rectus R -DC-	Frontal Mid L -C-	Frontal Sup R -DC-	-
128-electrode dataset with pre-transformation spatial projection	Frontal Mid L -C-	Supramarginal R, Parietal Inf R -DC-	Frontal Inf Tri R, Frontal Inf Orb R -DC-	Frontal Sup R -DC-
128-electrode dataset with post-transformation spatial projection	Frontal Mid L -C-	-	-	-
64-electrode dataset	Frontal Med Orb L, Frontal Med Orb R -DC-	Frontal Mid L -C-	-	-
32-electrode dataset	Frontal Mid L -C-	-	-	-
19-electrode dataset	N \A -DC-	-	-	-

Table 3.13: *EEG Source Imaging results of a non-averaged spike from an extended source in the left lateral frontal region with a source area of 5 cm^2. STKF results of the spike with 128 electrodes without spatial projection, 128 electrodes with pre-transformation spatial projection, 128 electrodes with post-transformation spatial projection, 64 electrodes, 32 electrodes, and 19 electrodes are listed in the table. For the strongest source and other ghost sources, anatomical labels from the AAL atlas are shown. If the maximum of the estimated source activity falls within the simulated region, the result is concordant, -C-, with the simulated region; if the maximum does not fall within the simulated region, the result is disconcordant, -DC-, with the simulated region. The table was adapted from a previous publication by the author [HAFM$^+$17b]*

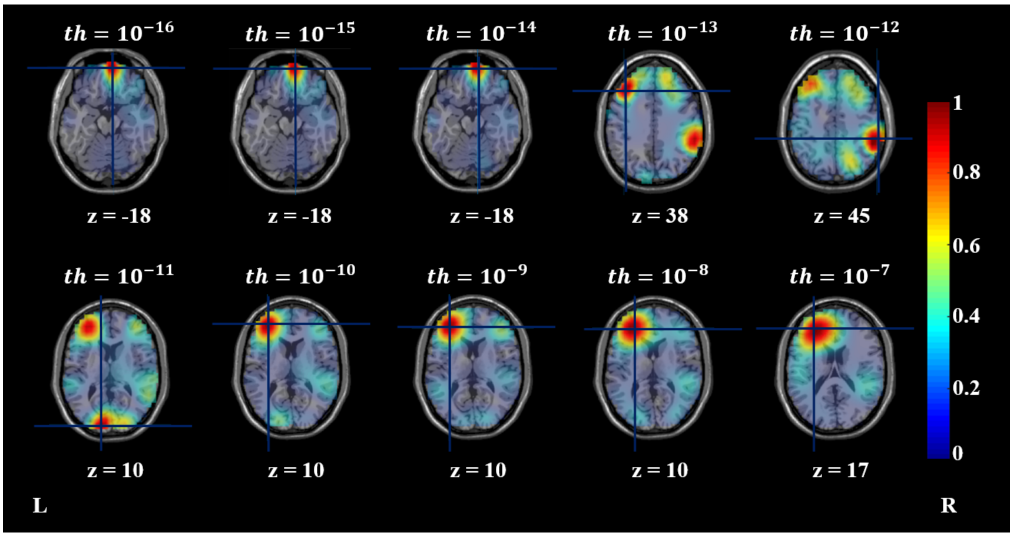

.

Figure 3.26: *EEG source imaging results of a non-averaged spike, which was generated from the left lateral frontal source with 5 cm*^{2} *source area. In the top row the reconstructed activity from the 128-electrode EEG dataset with post-transformation spatial projection with threshold values of* 10^{-16}, 10^{-15}, 10^{-14}, 10^{-13}, *and* 10^{-12} *is displayed. In the bottom row the results from the same dataset with threshold values of* 10^{-11}, 10^{-10}, 10^{-9}, 10^{-8}, *and* 10^{-7} *are shown. The results are visualized as axial MRI slices at each spike's peak, and the cursor is placed at the maximum of the estimated current density. Additionally the z-coordinates of the axial slices are shown in MNI coordinates. The source imaging results were visualized using the Fieldtrip software [OFMS11]*

EEG Datasets	Number of optimization steps until convergence	Computational time (s) of a single STKF call
19-electrode dataset	28	84.339
128-electrode dataset with post-transformation spatial projection	34	86.609
32-electrode dataset	34	92.838
128-electrode dataset with pre-transformation spatial projection	34	158.577
128-electrode dataset	76	239.767

Table 3.14: *Computational time (s) of a single STKF run and the number of optimization steps till convergence of EEG source imaging results via STKF of a non-averaged spike from an extended source in the left lateral frontal region with a source area of 5 cm^2. STKF results of the spike with 128 electrodes without spatial projection, 128 electrodes with pre-transformation spatial projection, 128 electrodes with post-transformation spatial projection, 64 electrodes, 32 electrodes, and 19 electrodes are listed in the table. The table was adapted from a previous publication by the author [HAFM$^+$17b]*

jection applied to the 128-electrode dataset using the standard threshold value from SPM8 produced the strongest source in the left lateral frontal region. The results of the post-transformation spatial projection were, however, without any ghost sources. Only the 128-electrode dataset with post-transformation spatial projection, the 32-electrode datasets, and the 19-electrode dataset resulted in accurate source localization with no ghost sources. So we conclude that the application of post-transformation spatial projection to the 128-electrode dataset solved the localization issues of both the 128-electrode and 64-electrode datasets. The application of spatial projection to the spatially-whitened LFM seems more natural since it is the LFM in the spatially-whitened state-space model. Additionally post spatial whitening, the spatially-projected LFM will not be subjected to any further linear transformation. This makes the interpretation and investigation of the transformed LFM easier. We conclude that spatial projection should happen after spatial whitening within the pipeline of the STKF.

Additionally, the application of post-transformation spatial projection led to a reduction of the computational time of a single STKF run by a factor of 2.7684. It is interesting to note that this computational time is comparable to that of the 19-electrode dataset, which is understandable since the standard threshold resulted in 26 orthogonal channels. The reduction in the number of necessary optimization steps until convergence by a factor of 2.2353 was similar for both pre- and post-transformation spatial projection. The first hypothesis was supported by the results of the first experiment if we choose to use post-transformation spatial projection.

The results of the second experiment showed that the standard threshold value produced a current density distribution that was somewhere between the results of the 19-electrode and

Threshold for spatial projection	Number of channels corresponding to the threshold	Anatomical label of strongest source	Presence of ghost sources
10^{-16}	127	Frontal Sup Orb R, Rectus R -DC-	yes
10^{-15}	125	Frontal Sup Orb R, Rectus R -DC-	yes
10^{-14}	120	Frontal Sup Orb R, Rectus R -DC-	yes
10^{-13}	106	Frontal Mid L -C-	yes
10^{-12}	89	Parietal Inf R, Supramarginal R -DC-	yes
10^{-11}	71	Occipital Sup L, Calcarine L -DC-	yes
10^{-10}	56	Frontal Mid L -C-	no
10^{-9}	44	Frontal Mid L, Frnotal Inf Tri L -C-	no
10^{-8}	34	Frontal Mid L -C-	no
10^{-7}	27	Frontal Mid L -C-	no

Table 3.15: *EEG Source Imaging results of a non-averaged spike from an extended source in the left lateral frontal region with a source area of 5 cm^2. The table lists the STKF results of the spike with 128 electrodes after applying post-transformation spatial projection using threshold values of 10^{-16}, 10^{-15}, 10^{-14}, 10^{-13}, 10^{-12}, 10^{-11}, 10^{-10}, 10^{-9}, 10^{-8}, and 10^{-7}. The number of channels that resulted from each threshold value is listed in the table. For the strongest source, anatomical labels from the AAL atlas and result evaluation are shown. If the maximum of the estimated source activity falls within the simulated region, the result is concordant, -C-, with the simulated region; if the maximum does not fall within the simulated region, the result is disconcordant, -DC-, with the simulated region.*

the 32-electrode datasets. A decrease in the threshold values until 10^{-10}, i.e., including more singular values, improves the accuracy and spatial resolution of the results. Additional increases in the threshold value results in a wrong localization of the strongest source in addition to ghost sources. We expected this result since the standard threshold in SPM8 was not optimally adapted to our 3D volumetric grids or LFMs. The decay of the singular values of the LFM needs to be studied for each LFM before deciding for the threshold value. These results confirmed the second hypothesis because the decrease of the threshold did improve the accuracy and spatial resolution of the STKF compared to the results obtained using the standard threshold from SPM8.

This study was performed only on simulated EEG data. In the future, the application of spatial projection to the STKF analyses of clinical EEG, MEG and simultaneous MEG-EEG data needs to be investigated. The study was also performed only on a BEM head model. The effects of detailed state-of-the-art FEM models on the stability of STKF and the application of spatial projection in conjunction with these head models will be studied in the future. Additionally, further investigations into the choice of the optimal threshold need to be conducted.

To summarize, we have combined spatial projection for the first time with the STKF to suppress information redundancy, ghost sources, and improve the accuracy of EEG source imaging via STKF in case of high-resolution EEG. First the optimal order of the STKF pipeline after the introduction of spatial projection was studied and we found out that it should be performed after spatial whitening. We also observed a reduction in the computational speed and the number of optimization steps required in the state-space parameter estimation step. Finally, we observed that a careful choice of the threshold of spatial projection can lead to improved accuracy and spatial resolution of STKF results.

Chapter 4

Source Imaging of Clinical EEG Data via the Spatiotemporal Kalman Filter

4.1 Motivation

We have seen in the previous chapter that the use of full-brain grids may improve the accuracy of both LORETA and STKF by avoiding very thin regions in the grid and spurious sources that results from the division of a single source into multiple sources because of grid density. Additional improvement of the localization accuracy may be obtained by the use of the modified Laplacian matrix which avoids the disadvantage of the classical Laplacian matrix that forces the current density to be zero at the borders of the grid. Finally the dynamical nature of the STKF leads to more focal and accurate sources. These results were obtained using simulated spikes.

In the first part of this chapter we try to reproduce the above mentioned results using clinical data of epileptic spikes from two patients of epilepsy. We hypothesize that the localization performance of both LORETA and STKF will improve after using full-brain grids and the modified Laplacian matrix. We also expect a superior performance of the STKF compared to LORETA with respect to model comparison and source localization.

In the second part we perform a similar analysis to the one from the first part to localize the onset of a focal seizure and investigate the effects of grid choice on the performance of LORETA and STKF. We hypothesize that the introduction of full-brain grids will improve the accuracy of both LORETA and STKF. Additionally, we expect STKF to produce more accurate results due to the additional temporal smoothness constraints in its state-space model. We also expect STKF to outperform LORETA in model comparison by showing smaller AIC values compared to LORETA's ABIC values.

In the final part we perform multimodal fusion by generalizing the STKF's measurement model measurement model in order to use simultaneous MEG-EEG measurements and compare the localization results of the EEG-only, MEG-only and simultaneous MEG-EEG datasets. We hypothesize that the combined information from both modalities, compared to the data from each separate modality, will stabilize and improve the localization performance of the STKF.

4.2 Source Imaging of Epileptiform Discharges via the Spatiotemporal Kalman Filter

EEG Source imaging results via LORETA and STKF at the spike peaks from Patient 1 were published by the author in [HHJ$^+$15].

4.2.1 Methods

Patient 1 is a male child who was diagnosed with drug-resistant temporal lobe epilepsy that was caused by a focal cortical dysplasia (FCD) in the right temporal lobe. The preoperative evaluation showed EEG activity in the right temporal lobe. After two operations, the outcome was Engel class IIb [EJ93]. This outcome means that the patient suffered from only 20 % of the original number of seizures that was registered before the operation.

Patient 2 is a teenage female patient suffering from hippocampal sclerosis in the left temporal lobe which caused drug-resistent mesial temporal lobe epilepsy (TLE). The patient was diagnosed according to the clinical guidelines in [Eng01]. During the preoperative evaluation, the patient's EEG showed interictal and ictal activity in the left temporal area. Hippocampal sclerosis was detected using the patient's MRI in addition to changes in caput hippocampi and the amygdala. The patient was then operated and areas from the amygdala and hippocampus were resected.The outcome of the operation was Engel Ib [EJ93] and it led to seizure-freedom.

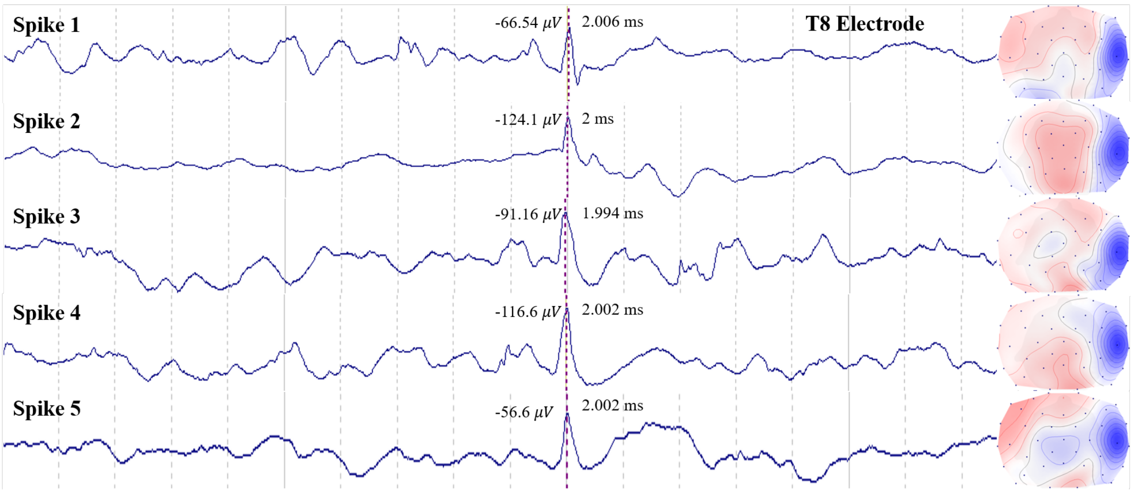

.

Figure 4.1: *The time series of the dominant electrode showing five non-averaged spikes, selected from the EEG recording of Patient 1. The cursor is located at each spike's peak. Additionally, the time (in ms) at each spike's peak is shown to the left of each respective peak. The EEG amplitudes at the spike peaks are shown to the right of each peak point. In the right column the voltage maps (positive in red, negative in blue) corresponding to the spike peaks are shown. The images were produced using CURRY7. The figure was inspired by the figures published by the author in [HHJ$^+$15]*

The presurgical EEG recordings of Patients 1 and 2 were performed with 40 electrodes and a sampling frequency of 500 Hz using the Nikon Kohden System (http://www.nihonkohden.com). The electrode layout is displayed in Fig 4.3. Power-supply artifacts were removed using a Butterworth notch filter with a cut-off frequency of 50 Hz. The removal of drifts in the data was performed using a high-pass Butterworth filter with a cut-off frequency of 0.53 Hz. The filters were applied only in the forward direction. After that, five artifact-free EEG segments from each patient's recording were marked and visually selected, each of which contained a non-averaged spike. The spike waveforms from Patient 1 are shown in Fig 4.1 and the waveforms from Patient 2 are shown in Fig 4.2 with markers and voltage maps at the spike peaks. The signals of the T8 electrode for Patient 1 and the T7 electrode for Patient 2 were used to mark the spike onset at 50 of the spike's rise time. Each segment was then standardized and average-referenced before source analysis. The SNR of each spike was calculated using the method described in section 2.1.

The preoperative MRIs of Patient 1 and Patient 2 were recorded in Kiel using a 3-Tesla MR scanner (Philips Achieva; Philips, Best, The Netherlands). The T1-weighted MRIs of both patients had a resolution of 0.8752×1 mm^3. Before the application of automatic segmentation algorithms from CURRY7, both MRIs were preprocessed using SPM8 (Wellcome Trust Centre for Neuroimaging, University College, London) in order to remove inhomogeneity artifacts that negatively influence automatic segmentation. For each patient, a realistic and individual BEM head model was computed in CURRY7. Both head models had inner skull, outer skull, and scalp compartments with conductivity values of 0.33 S/m, 0.0042 S/m, and 0.33 S/m, respectively. In the head model of Patient 1 the inner skull, outer skull, and scalp were meshed using 3168, 1931, and 1942 nodes, respectively. Two grids with 7 mm grid resolution were defined. A slightly-thickened gray-matter grid was created with 3816 points and a full-brain grid was also created with 4783 points. Similarly for Patient 2, the inner skull, outer skull, and scalp were described by 1993, 1261, and 1503 nodes, respectively. After that, a slightly-thickened gray-matter grid with 2667 grid points and a full-brain grid with 4208 points were defined. Both grids had a resolution of 7 mm.

Source analysis was performed using LORETA and STKF on the data of Patient 1 and Patient 2. The STKF's dynamical model was chosen to be an autoregressive model of first order. Three models were used for the analysis based on the grid choice and the definition of the Laplacian matrix. The first model used a gray-matter grid while the other two models used a full-brain grid. The first two models used the classical definition of the Laplacian matrix while the third one used the modified definition of the Laplacian matrix. The whole procedure is shown in Fig 4.4.

4.2.2 Results

We will start with the results from Patient 1's data. The SNR values of the spikes considering only the background activity of the signal from electrode T8 were 16.0755 dB, 12.966 dB, 16.2521 dB, 16.6015 dB, and 15.3805 dB, respectively. At the spikes' onset points, LORETA

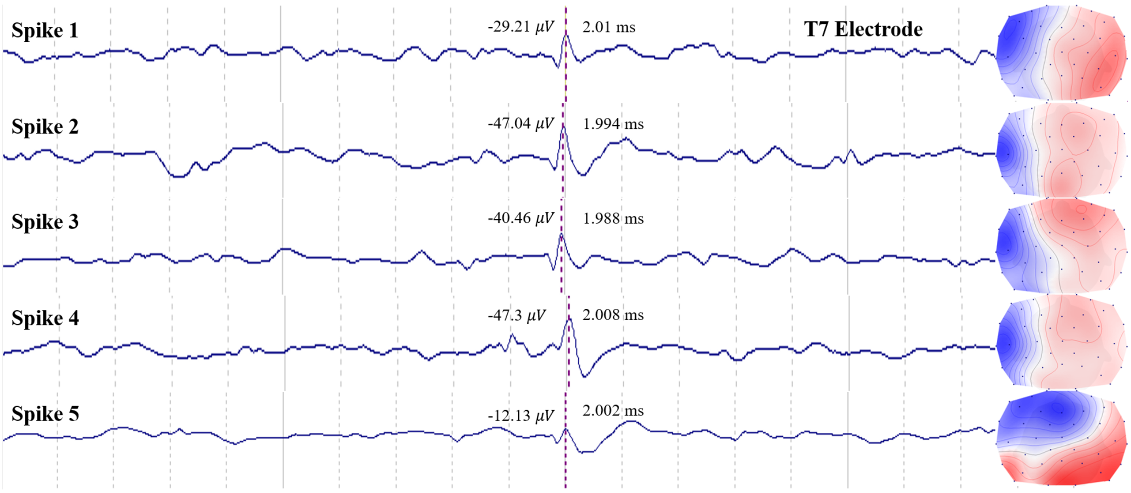

.

Figure 4.2: *The time series of the dominant electrode showing five non-averaged spikes, selected from the EEG recording of Patient 2. The cursor is located at each spike's peak. Additionally, the time (in ms) at each spike's peak is shown to the left of each respective peak. The EEG amplitudes at the spike peaks are shown to the right of each peak point. In the right column the voltage maps (positive in red, negative in blue) corresponding to the spike peaks are shown. The images were produced using CURRY7.*

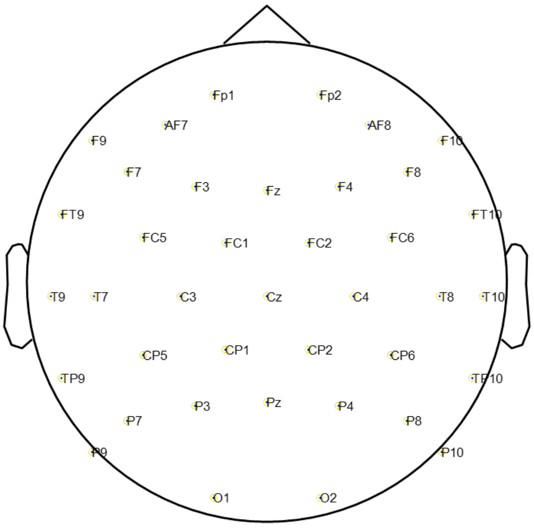

.

Figure 4.3: *The figure displays 39-channel EEG electrode layout used for recording EEG datasets of Patient 1 and Patient 2. The layout was visualized using the Fieldtrip Software [OFMS11].*

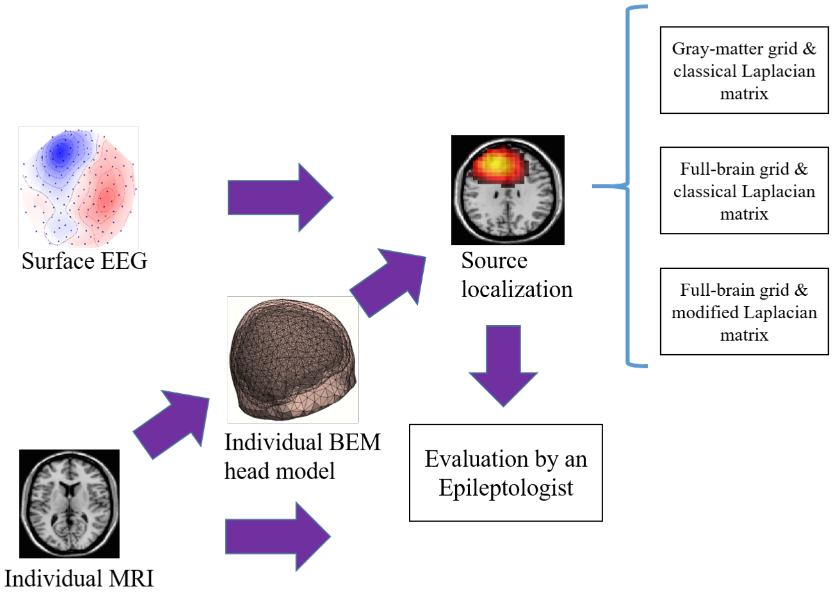

Figure 4.4: *An overview of the analysis pipeline is shown which includes EEG preprocessing, MRI preprocessing, individual head modeling, source imaging via LORETA and STKF, and evaluation by an expert epileptologist. The images were produced using CURRY7.*

showed sources in the right hemisphere in 2/5 spikes using the first model. The results of the second model were similar to the first one. Using the third model, LORETA produced sources in the right hemisphere in 3/5 spikes. EEG source imaging results of LORETA at the spikes' onset points are shown in Fig 4.5. EEG source imaging via STKF showed localization results in the right hemisphere in 3/5 spikes for the first model. The application of the second model resulted in activity in the right hemisphere in 4/5 cases. Finally, the third model showed right-hemispheric sources in 3/5 spikes. STKF results at the spikes' onsets are displayed in Fig 4.6.

At the spikes' peaks, LORETA resulted in sources in the right hemisphere for 5/5 spikes using the first and third models. The second model resulted in right-hemispheric sources in 4/5 spikes. These results are summarized in Fig 4.7. The application of STKF with the first model at the spikes' peaks estimated the sources in the right hemisphere in 4/5 spikes. The application of the second and third models showed the sources in the right hemisphere for all spikes. The results of STKF are shown in Fig 4.8. Sources from the first model were the most focal ones for both LORETA and STKF. The sources from the second and third models were closer to the target area and more focal in STKF results compared to those of LORETA.

The ABIC results of LORETA and AIC results of STKF are summarized and listed in Table 4.1 and Table 4.2. STKF results had consistently lower AIC compared to LORETA's ABIC values. Additionally, the use of the modified Laplacian matrix resulted in lower ABIC or AIC values compared to the use of the classical Laplacian matrix.

For Patient 2, the SNR values of the spikes computed using the background activity of the

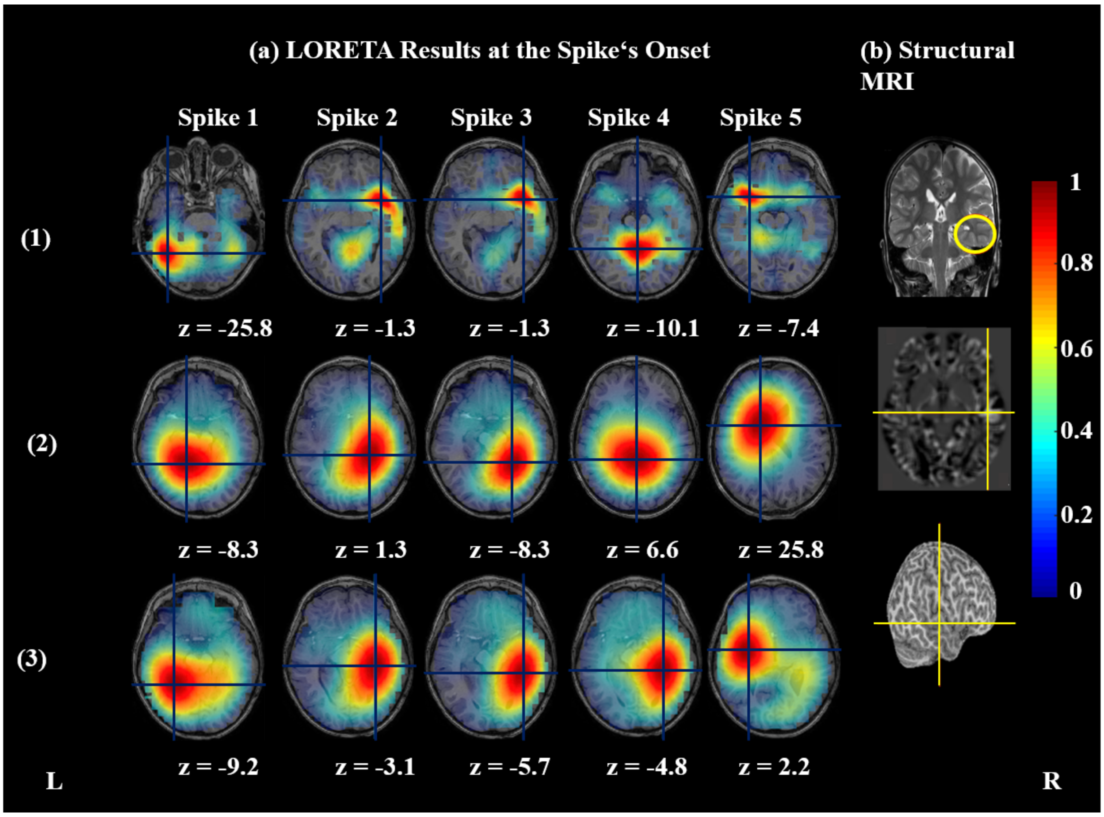

.

Figure 4.5: *(a) Results of EEG source imaging via LORETA of 5 non-averaged spikes from the EEG recordings of Patient 1. LORETA results using a gray-matter 3D grid and the classical Laplacian matrix are depicted in (1). Results using a full-brain 3D grid and the classical Laplacian matrix are shown in (2). For the results shown in (3), a full-brain grid and the modified Laplacian matrix were used. From left to right the results of Spikes 1-5 are shown in columns 1-5, respectively. The results are visualized as axial MRI slices at each spike's onset,which is defined as 50% of the spike's rise time, and the cursor is placed at the maximum of the estimated current density. Additionally the z-coordinates of the axial slices are shown in Montreal Neurological Institute (MNI) coordinates. In (b) The location and the extent of the FCD on a coronal slice from the patient's preoperative T2-weighted MRI is shown and marked with a yellow circle (top). Additionally in (b), the centers of the yellow cursor mark the detected FCD on an axial slice after morphometric Huppertz MRI analysis [HGF*$^{+}$*05] (middle) and the FCD on the brain's cortical surface after morphometric Huppertz MRI analysis [HGF*$^{+}$*05] (bottom). The source imaging results were visualized using the Fieldtrip software [OFMS11]. The figure was adapted from the figures published by the author in [HHJ*$^{+}$*15]*

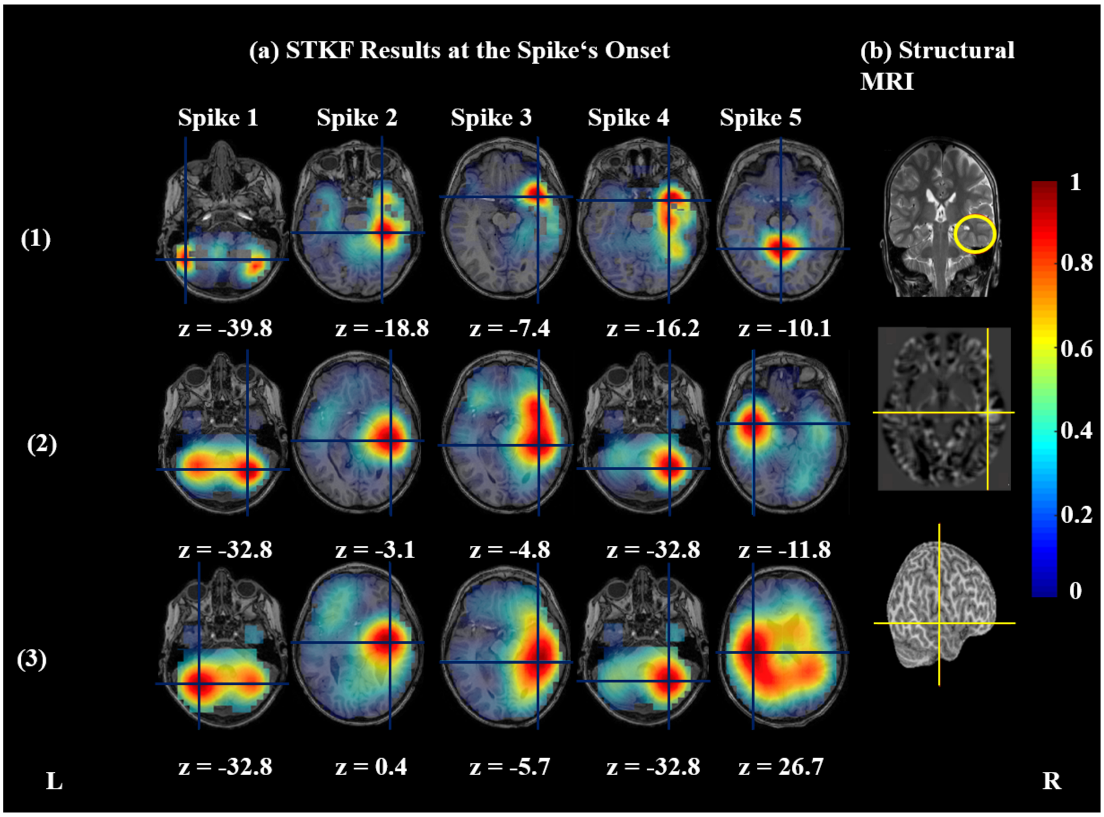

.

Figure 4.6: *(a) Results of EEG source imaging via STKF of 5 non-averaged spikes from the EEG recordings of Patient 1. STKF results using a gray-matter 3D grid and the classical Laplacian matrix are depicted in (1). Results using a full-brain 3D grid and the classical Laplacian matrix are shown in (2). For the results shown in (3), a full-brain grid and the modified Laplacian matrix were used. From left to right the results of Spikes 1-5 are shown in columns 1-5, respectively. The results are visualized as axial MRI slices at each spike's onset,which is defined as 50% of the spike's rise time, and the cursor is placed at the maximum of the estimated current density. Additionally the z-coordinates of the axial slices are shown in Montreal Neurological Institute (MNI) coordinates. In (b) The location and the extent of the FCD on a coronal slice from the patient's preoperative T2-weighted MRI is shown and marked with a yellow circle (top). Additionally in (b), the centers of the yellow cursor mark the detected FCD on an axial slice after morphometric Huppertz MRI analysis [HGF$^+$05] (middle) and the FCD on the brain's cortical surface after morphometric Huppertz MRI analysis [HGF$^+$05] (bottom). The source imaging results were visualized using the Fieldtrip software [OFMS11]. The figure was adapted from the figures published by the author in [HHJ$^+$15]*

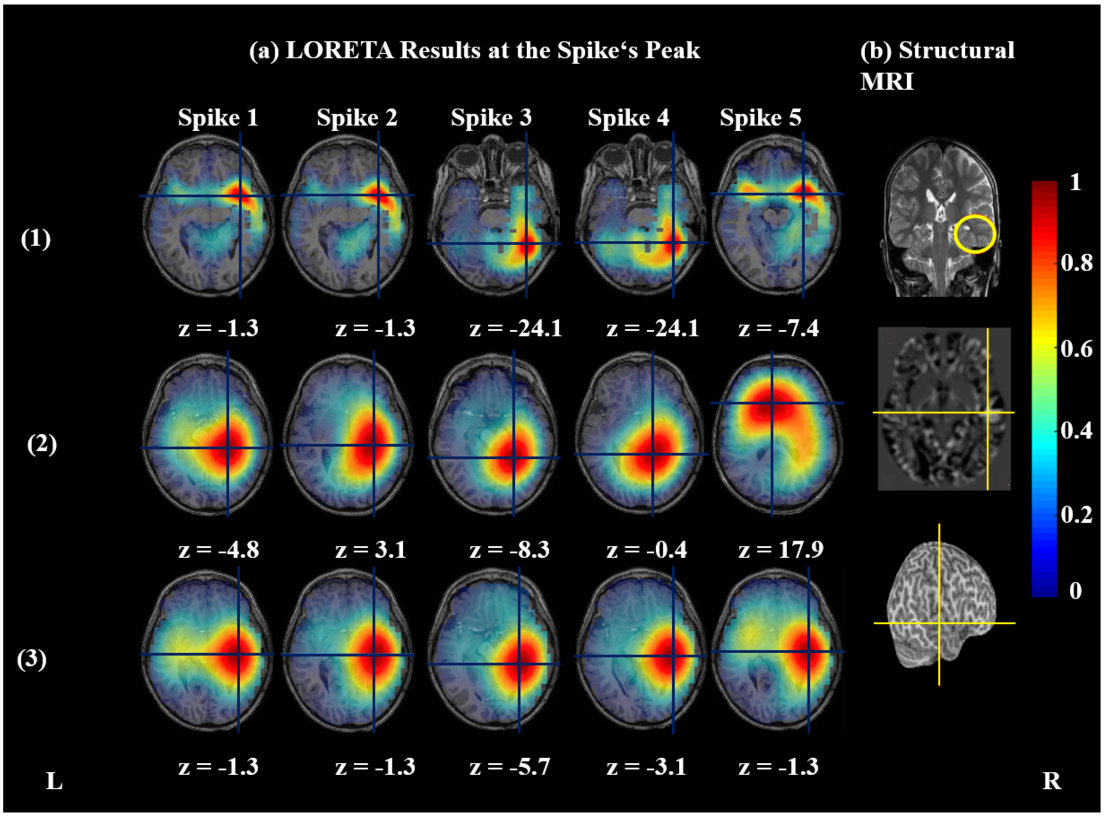

.

Figure 4.7: *(a) Results of EEG source imaging via LORETA of 5 non-averaged spikes from the EEG recordings of Patient 1. LORETA results using a gray-matter 3D grid and the classical Laplacian matrix are depicted in (1). Results using a full-brain 3D grid and the classical Laplacian matrix are shown in (2). For the results shown in (3), a full-brain grid and the modified Laplacian matrix were used. From left to right the results of Spikes 1-5 are shown in columns 1-5, respectively. The results are visualized as axial MRI slices at each spike's peak and the cursor is placed at the maximum of the estimated current density. Additionally the z-coordinates of the axial slices are shown in Montreal Neurological Institute (MNI) coordinates. In (b) The location and the extent of the FCD on a coronal slice from the patient's preoperative T2-weighted MRI is shown and marked with a yellow circle (top). Additionally in (b), the centers of the yellow cursor mark the detected FCD on an axial slice after morphometric Huppertz MRI analysis [HGF$^+$05] (middle) and the FCD on the brain's cortical surface after morphometric Huppertz MRI analysis [HGF$^+$05] (bottom). The source imaging results were visualized using the Fieldtrip software [OFMS11]. The figure was adapted from the figures published by the author in [HHJ$^+$15]*

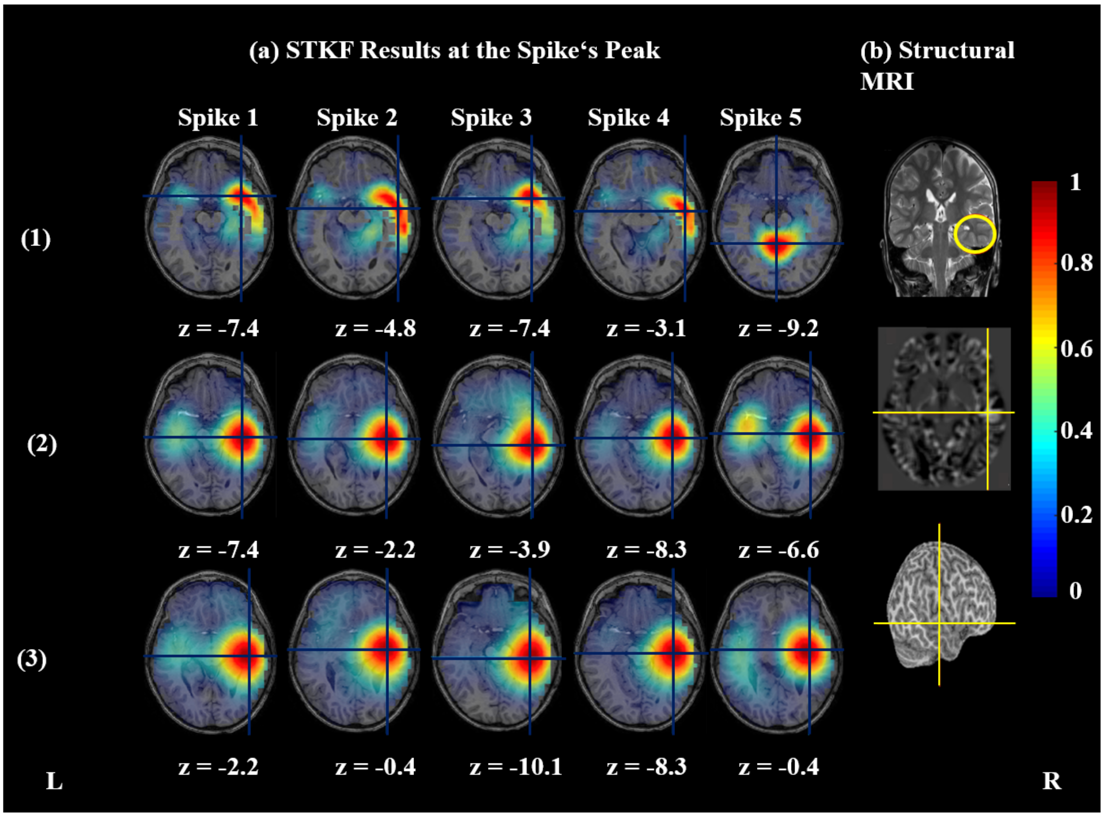

.

Figure 4.8: *(a) Results of EEG source imaging via STKF of 5 non-averaged spikes from the EEG recordings of Patient 1. STKF results using a gray-matter 3D grid and the classical Laplacian matrix are depicted in (1). Results using a full-brain 3D grid and the classical Laplacian matrix are shown in (2). For the results shown in (3), a full-brain grid and the modified Laplacian matrix were used. From left to right the results of Spikes 1-5 are shown in columns 1-5, respectively. The results are visualized as axial MRI slices at each spike's peak and the cursor is placed at the maximum of the estimated current density. Additionally the z-coordinates of the axial slices are shown in Montreal Neurological Institute (MNI) coordinates. In (b) The location and the extent of the FCD on a coronal slice from the patient's preoperative T2-weighted MRI is shown and marked with a yellow circle (top). Additionally in (b), the centers of the yellow cursor mark the detected FCD on an axial slice after morphometric Huppertz MRI analysis [HGF$^+$05] (middle) and the FCD on the brain's cortical surface after morphometric Huppertz MRI analysis [HGF$^+$05] (bottom). The source imaging results were visualized using the Fieldtrip software [OFMS11]. The figure was adapted from the figures published by the author in [HHJ$^+$15]*

Datasets	Spike 1	Spike 2	Spike 3	Spike 4	Spike 5
Gray-matter grid, classical Laplacian matrix	17329.3666	37091.9908	16407.0575	20149.3177	13568.5419
Full-brain grid, classical Laplacian matrix	18015.3764	39764.8359	17457.8974	20660.0842	14317.6504
Full-brain grid, modified Laplacian matrix	15274.8085	33641.2593	12852.1926	15440.6389	9965.6777

Table 4.1: *The table lists ABIC values resulting from EEG source imaging via LORETA of five non-averaged spikes from Patient 1. The first analysis was performed using a gray-matter grid and the classical Laplacian matrix. The second analysis was performed using a full-brain grid and the classical Laplacian matrix. The third analysis was performed using using a full-brain grid and the modified Laplacian matrix.*

Datasets	Spike 1	Spike 2	Spike 3	Spike 4	Spike 5
Gray-matter grid, classical Laplacian matrix	7332.4385	4071.8944	1616.5824	6222.8869	-2578.3523
Full-brain grid, classical Laplacian matrix	11701.7231	14726.2873	7059.5908	11710.1292	3482.3567
Full-brain grid, modified Laplacian matrix	8375.7396	9779.5817	3491.0327	7117.8335	-70.4493

Table 4.2: *The table lists AIC values resulting from EEG source imaging via STKF of five non-averaged spikes from Patient 1. The first analysis was performed using a gray-matter grid and the classical Laplacian matrix. The second analysis was performed using a full-brain grid and the classical Laplacian matrix. The third analysis was performed using using a full-brain grid and the modified Laplacian matrix.*

Datasets	Spike 1	Spike 2	Spike 3	Spike 4	Spike 5
Gray-matter grid, classical Laplacian matrix	30860.0509	20605.4178	26023.2922	29466.0151	39716.214
Full-brain grid, classical Laplacian matrix	32354.2004	22137.9289	26796.3081	30935.2978	40728.2336
Full-brain grid, modified Laplacian matrix	19752.4203	11018.88	15202.7629	16054.2245	22380.4173

Table 4.3: *The table lists ABIC values resulting from EEG source imaging via LORETA of five non-averaged spikes from Patient 2. The first analysis was performed using a gray-matter grid and the classical Laplacian matrix. The second analysis was performed using a full-brain grid and the classical Laplacian matrix. The third analysis was performed using using a full-brain grid and the modified Laplacian matrix.*

dominant electrode T7 were 18.5746 dB, 17.1866 dB, 21.1336 dB, 19.9886 dB, and 9.0586 dB, respectively. The EEG source imaging results of Patient 2's spikes via LORETA at the onset of each spikes are shown in Fig 4.9. The application of the first, second, and third models resulted in sources in the left hemisphere in 2/5, 1/5, and 4/5 spikes, respectively. The STKF results at the spikes' onset points after applying the first, second, and third models resulted in left-hemispheric sources in 3/5, 1/5, and 5/5 spikes, respectively. These results are summarized and plotted in Fig 4.10.

At the spikes' peaks, results of LORETA are shown in Fig 4.11 while the results of STKF are summarized in Fig 4.12. Both LORETA and STKF show sources in the left hemisphere in 5/5 spikes. Compared to LORETA, STKF produces more consistent and more focal sources. Additionally, STKF sources were closer to the target area than those produced by LORETA.

The ABIC results of LORETA are listed in Table 4.3 while the AIC results of STKF are shown in Table 4.4. STKF's AIC results are always lower than ABIC values of LORETA. Additionally, the lowest ABIC or AIC values were obtained when the modified Laplacian matrix was used and not the classical Laplacian matrix.

4.2.3 Discussion

Both hypotheses were confirmed by the source reconstruction of EEG data from Patients 1 and 2. For Patient 1, the LORETA results benefited more from the combined use of the full-grid with the modified Laplacian than from the full-grid with the classical Laplacian matrix. STKF results using the full grid with the classical or modified Laplacian were comparable or better than those

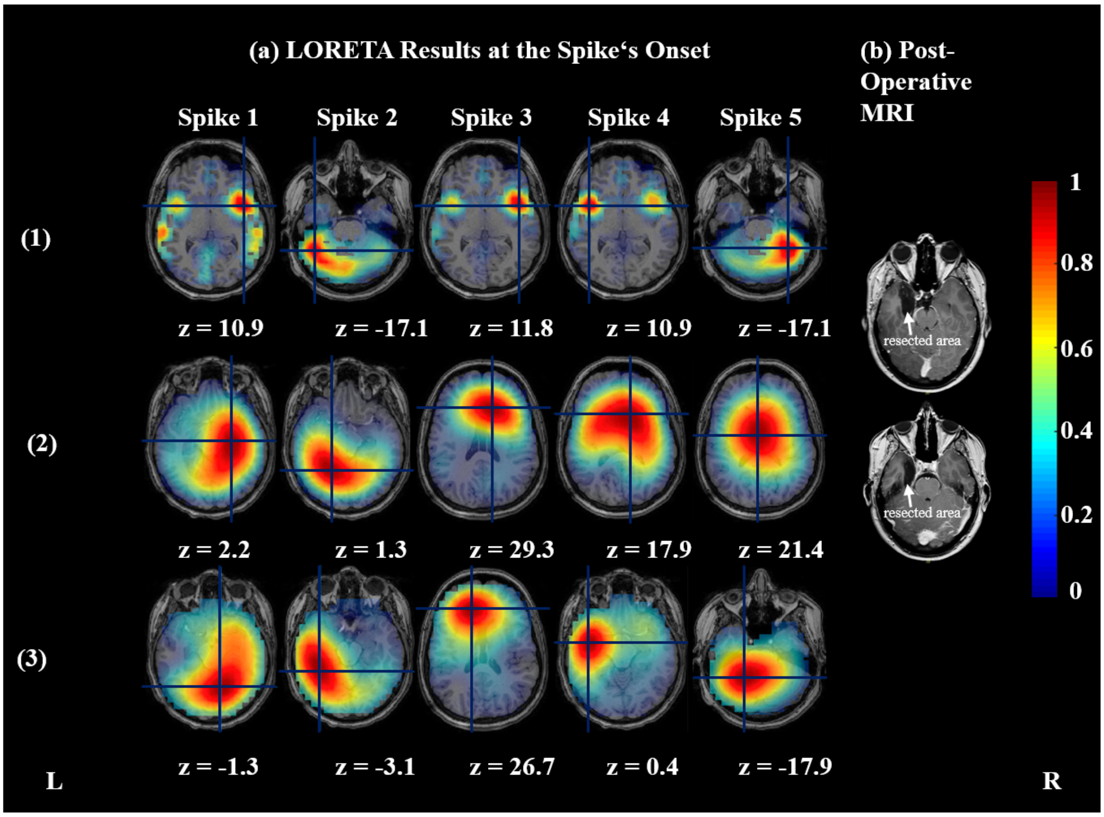

.

Figure 4.9: *(a) Results of EEG source imaging via LORETA of 5 non-averaged spikes from the EEG recordings of Patient 2. LORETA results using a gray-matter 3D grid and the classical Laplacian matrix are depicted in (1). Results using a full-brain 3D grid and the classical Laplacian matrix are shown in (2). For the results shown in (3), a full-brain grid and the modified Laplacian matrix were used. From left to right the results of Spikes 1-5 are shown in columns 1-5, respectively. The results are visualized as axial MRI slices at each spike's onset,which is defined as 50% of the spike's rise time, and the cursor is placed at the maximum of the estimated current density. Additionally the z-coordinates of the axial slices are shown in Montreal Neurological Institute (MNI) coordinates. (b) The location and the extent of the resected region in two axial slices from the patient's postoperative MRI. The source imaging results were visualized using the Fieldtrip software [OFMS11]*

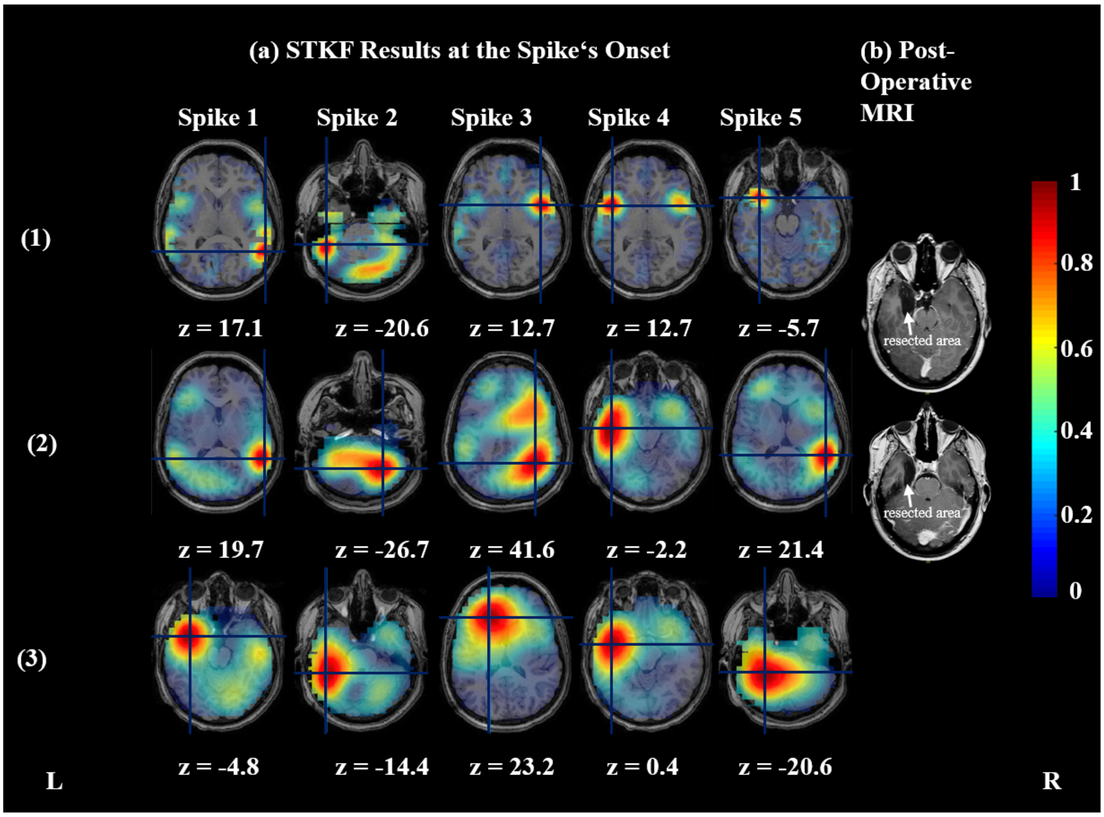

Figure 4.10: *(a) Results of EEG source imaging via STKF of 5 non-averaged spikes from the EEG recordings of Patient 2. STKF results using a gray-matter 3D grid and the classical Laplacian matrix are depicted in (1). Results using a full-brain 3D grid and the classical Laplacian matrix are shown in (2). For the results shown in (3), a full-brain grid and the modified Laplacian matrix were used. From left to right the results of Spikes 1-5 are shown in columns 1-5, respectively. The results are visualized as axial MRI slices at each spike's onset,which is defined as 50% of the spike's rise time, and the cursor is placed at the maximum of the estimated current density. Additionally the z-coordinates of the axial slices are shown in Montreal Neurological Institute (MNI) coordinates. (b) The location and the extent of the resected region in two axial slices from the patient's postoperative MRI. The source imaging results were visualized using the Fieldtrip software [OFMS11]*

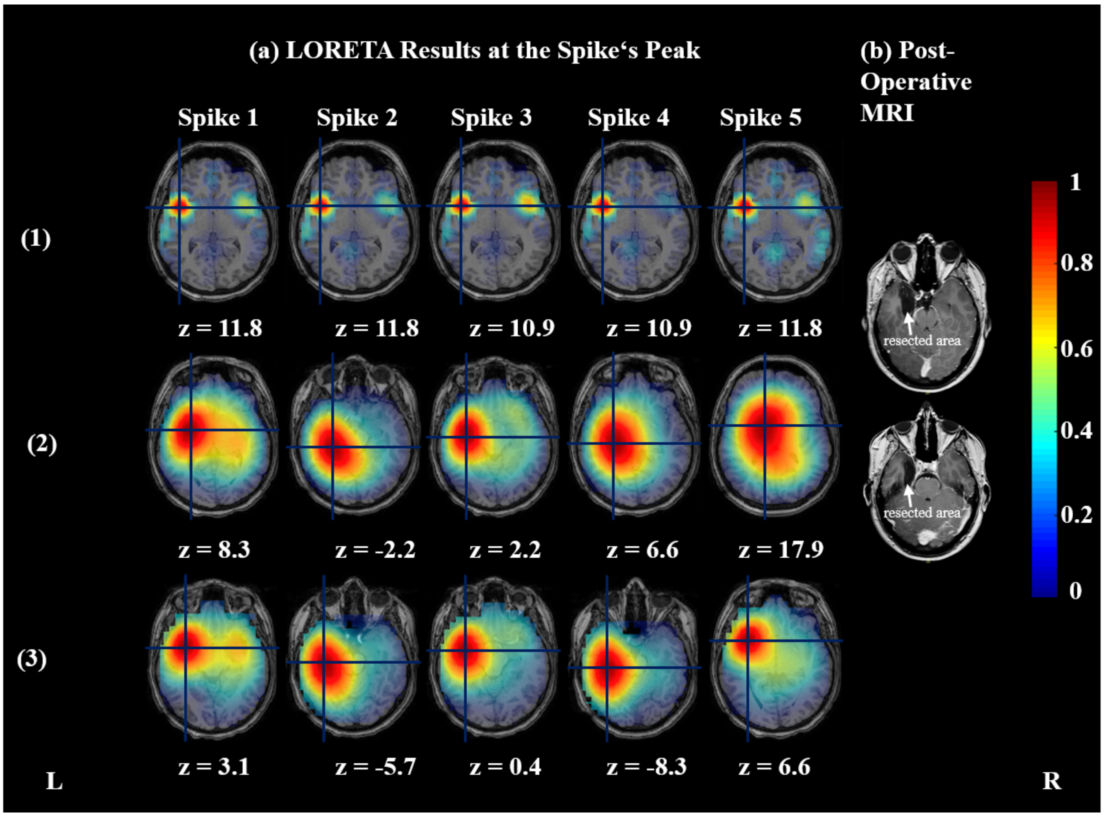

Figure 4.11: *(a) Results of EEG source imaging via LORETA of 5 non-averaged spikes from the EEG recordings of Patient 2. LORETA results using a gray-matter 3D grid and the classical Laplacian matrix are depicted in (1). Results using a full-brain 3D grid and the classical Laplacian matrix are shown in (2). For the results shown in (3), a full-brain grid and the modified Laplacian matrix were used. From left to right the results of Spikes 1-5 are shown in columns 1-5, respectively. The results are visualized as axial MRI slices at each spike's peak and the cursor is placed at the maximum of the estimated current density. Additionally the z-coordinates of the axial slices are shown in Montreal Neurological Institute (MNI) coordinates. (b) The location and the extent of the resected region in two axial slices from the patient's postoperative MRI. The source imaging results were visualized using the Fieldtrip software [OFMS11]*

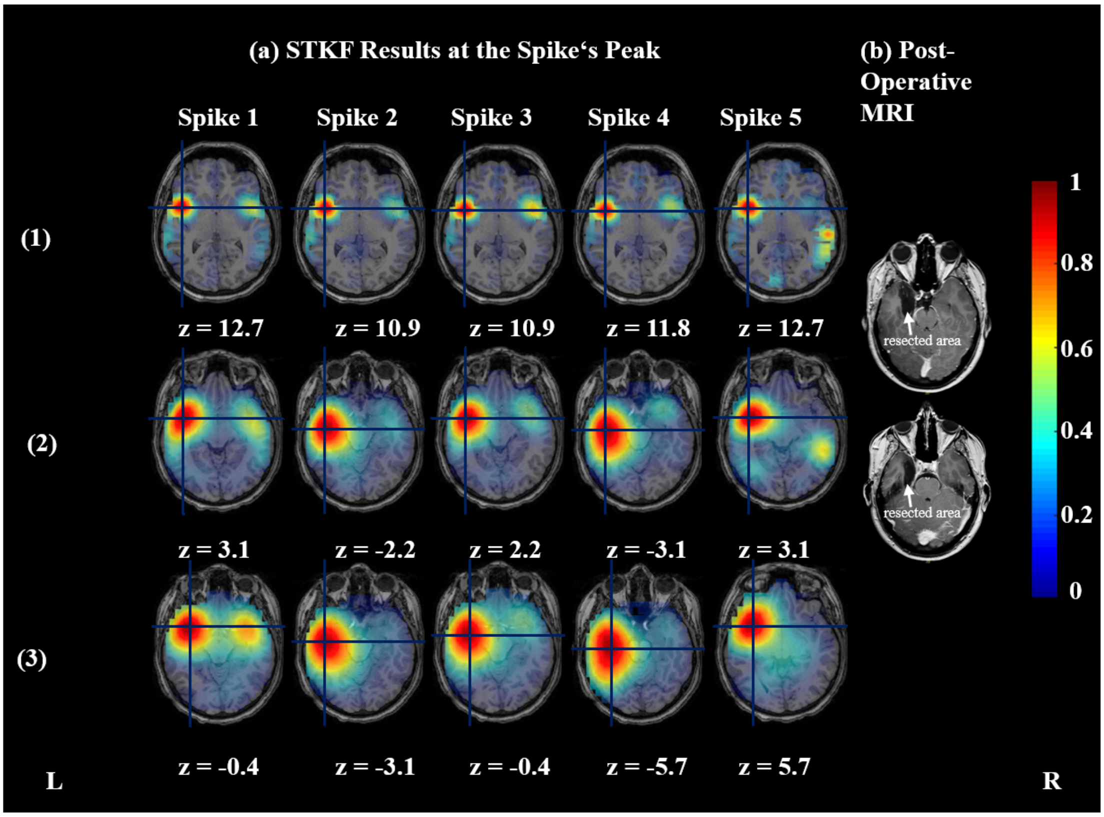

.

Figure 4.12: *(a) Results of EEG source imaging via STKF of 5 non-averaged spikes from the EEG recordings of Patient 2. STKF results using a gray-matter 3D grid and the classical Laplacian matrix are depicted in (1). Results using a full-brain 3D grid and the classical Laplacian matrix are shown in (2). For the results shown in (3), a full-brain grid and the modified Laplacian matrix were used. From left to right the results of Spikes 1-5 are shown in columns 1-5, respectively. The results are visualized as axial MRI slices at each spike's peak and the cursor is placed at the maximum of the estimated current density. Additionally the z-coordinates of the axial slices are shown in Montreal Neurological Institute (MNI) coordinates. (b) The location and the extent of the resected region in two axial slices from the patient's postoperative MRI. The source imaging results were visualized using the Fieldtrip software [OFMS11]*

Datasets	Spike 1	Spike 2	Spike 3	Spike 4	Spike 5
Gray-matter grid, classical Laplacian matrix	1557.5862	-3417.7676	-1386.9827	-2223.1803	5733.7182
Full-brain grid, classical Laplacian matrix	10180.1116	3901.8276	5902.2392	5253.6733	13466.4633
Full-brain grid, modified Laplacian matrix	1528.2345	-3250.4733	-1987.9493	-471.274	3690.7039

Table 4.4: *The table lists AIC values resulting from EEG source imaging via STKF of five non-averaged spikes from Patient 2. The first analysis was performed using a gray-matter grid and the classical Laplacian matrix. The second analysis was performed using a full-brain grid and the classical Laplacian matrix. The third analysis was performed using using a full-brain grid and the modified Laplacian matrix.*

using the gray-matter grid. In general, STKF produced comparable or better results than those of LORETA. Additionally, sources estimated by STKF were more focal and closer to the lateral temporal region than the sources estimated by LORETA. Statistical model comparison favored the STKF, since the AIC values were consistently lower than LORETA's ABIC. Additionally, model comparison showed that the use of the full-brain grid with the modified Laplacian matrix explained the data better since it resulted in the lowest ABIC or AIC values compared to the case of the full-brain grid and the classical Laplacian matrix.

For Patient 2 at the spikes' onsets, the combination of full-brain grid and modified Laplacian matrix outperformed the other two models. Additionally, STKF showed better results than those of LORETA for the first and third models. STKF, using the second and third models at the spikes' peaks, is more consistent and has better spatial resolution compared to LORETA. Statistical model comparison showed again the STKF described the data better than LORETA. The results of model comparison regarding the choice of the Laplacian matrix are similar to those that were obtained using EEG data from Patient 1.

In evaluating the results we preferred to use the information about the hemisphere in which the source was located in order to get more general results about the effects of the grid choice, Laplacian matrix, and source imaging method. For Patient 1, being in the right hemisphere almost always meant being close to or within the target area in the right lateral temporal lobe, since the source was superficial. Using the real epileptogenic zone for Patient 2 would make all results disconcordant with the resected volume in the amygdalo-hippocampal complex, since the source is small and deep in the brain. The simplified evaluation model helps us, however, to see the gradual improvement in the localization. The onset points seem to have a very small

SNR which leads to variability in the reconstructed source locations. The concept of the onset points is used more often in conjunction with averaged spikes with much higher SNR than non-averaged spikes. For non-averaged spikes it is often not clear how to define the onset point. Here we defined it based on the signal from the dominant electrode. The results at the peak seem to be more accurate and more consistent.

The study suffered from some limitations. The use of a larger group of patients and more spikes from each patient would improve the evaluation of the performance of LORETA and STKF with the different grids and Laplacian matrices. Additionally, the use of postoperative MRIs to segment the lesion and quantify the distance of the reconstructed current density distribution to the resected volume would give a better idea about the accuracy of each method. Finally, we may improve the accuracy and spatial resolution of the STKF further if we permit multiple regions in the brain to have their own dynamics within the state-space model. This model will be used on the five spikes from Patient 2 in Chapter 5.

In summary we applied the STKF and LORETA to non-averaged epileptic spikes from the EEG recordings of two patients with temporal lobe epilepsy. We aimed at studying the influence of grid choice and Laplacian matrix. the introduction of full-grids alone did not help improve the accuracy of localization. Only when the full-grid was combined with the modified Laplacian matrix did the results start to improve. This was also backed by model comparison, Additionally, STKF benefited from its dynamical nature and showed improved accuracy, spatial resolution, and consistency of localization, compared to LORETA. STKF also outperformed LORETA in model comparison.

4.3 Source Imaging of Focal Seizure Onset via the Spatiotemporal Kalman Filter

The analyses with gray-matter and full-brain grids in conjunction with the classical Laplacian matrix were produced in the master thesis of Masoud Sarabi [Sar14] under the author's supervision. The author published the results of this section in [HSJ$^+$15].

4.3.1 Methods

The focal seizure was registered in EEG recordings of Patient 3, who is a teenage male patient of epilepsy. In this patient's case, a large FCD that extended over the left temporal, parietal, and occipital regions was the cause of drug-resistant epilepsy. The EEG recording of Patient 3 was performed with 45 electrodes and a sampling frequency of 500 Hz using the Nikon Kohden System (http://www.nihonkohden.com). The electrode layout can be seen in Fig 4.13. A slow and high-amplitude oscillation was noticed in the frontal channels as the seizure began. In the same time, channels P9 and PO7 showed a low-amplitude and fast oscillation that was typical of the temporal, parietal, and occipital electrodes. The oscillation from channel P9 is displayed in Fig 4.14 with a labeling of the first oscillatory 6 peaks. Since we wanted to emphasize the latter type of oscillation in the beta band, we used a low-pass Butterworth filter with a cut-off frequency of 35 Hz. This led also to the removal of power-supply artifacts. The removal of drifts in the data was performed using a high-pass Butterworth filter with a cut-off frequency of 1 Hz. The filters were applied only in the forward direction. After that, a single focal seizure from Patient 3 was marked and selected. Finally, the EEG data was then standardized and average-referenced before source analysis.

The patient's preoperative T1-weighted MRI (1 mm^3) was recorded in Kiel using a 3-Tesla MR scanner (Philips Achieva; Philips, Best, The Netherlands). The RF inhomogeneity artifacts were suppressed using SPM8 (Wellcome Trust Centre for Neuroimaging, University College, London). The segmentation and meshing of the individual MRI were performed using CURRY7. After that, a realistic head model that included the scalp, outer skull, and inner skull compartments was computed using the boundary element method. The conductivities of the aforementioned compartments were set to 0.33 S/m, 0.0042 S/m, and 0.33 S/m, respectively. For the source space, a slightly thickened gray-matter volumetric grid with 1917 grid points and 7 mm grid spacing was generated first. In addition to that, a full-brain grid with 7 mm resolution and 3290 points was generated. In the inverse modeling step, EEG source imaging was performed first via LORETA using three analysis models. In the first model a gray-matter grid and the classical Laplacian matrix were used. In the second model a full-brain grid was used along with the classical Laplacian matrix. These models were also used for source imaging via STKF. The dynamical model of the STKF was an autoregressive model of second order, since we are interested in the localization of a brain oscillation.

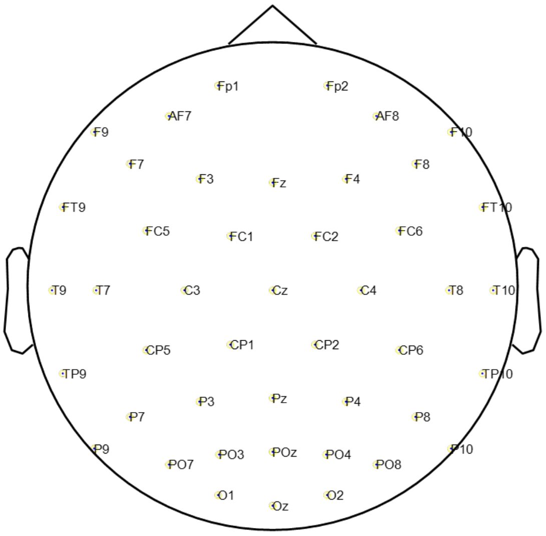

Figure 4.13: *The figure displays 45-channel EEG electrode layout used for recording EEG dataset of Patient 3. The layout was visualized using the Fieldtrip Software [OFMS11].*

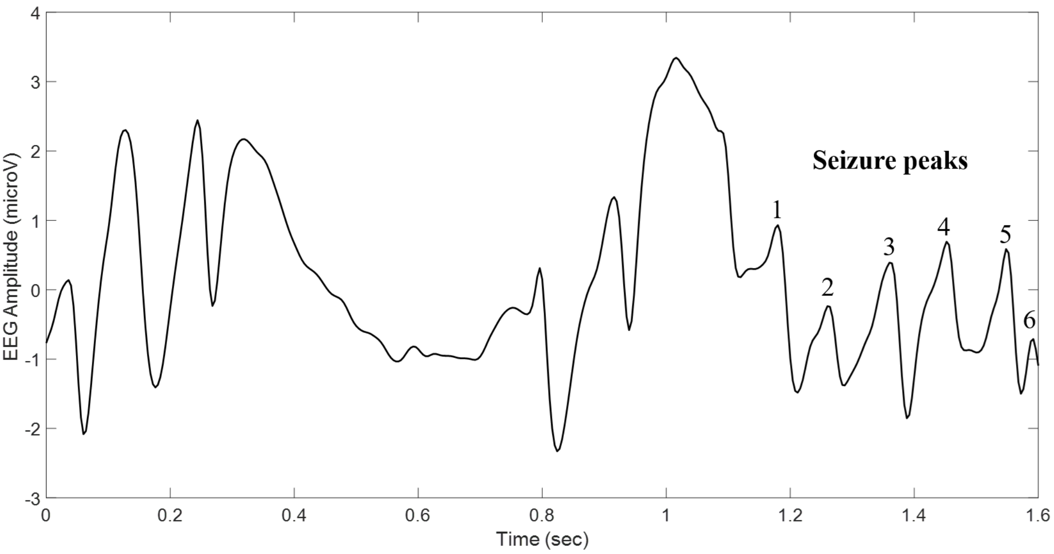

Figure 4.14: This figure shows the six peaks from the seizure onset phase that were used to visualize the EEG source imaging results. The time series of the P9 electrode was used for visualization. The figure was adapted from the figures supervised or published by the author in [Sar14, HSJ^{+}15]

4.3.2 Results

EEG source imaging via LORETA using the gray-matter grid produced sources that were in different regions, mostly in the frontal region, in the left and also the right hemispheres. The sources were localized in the left hemisphere in 4/6 cases. The use of the full-brain grid slightly improved the consistency of the localization across the six peaks, since now the sources were localized in the left hemisphere in 5/6 cases. The results of LORETA are visualized in Fig 4.15. The resulting ABIC values are listed in Table 4.5.

The application of STKF to the seizure EEG data in conjunction with the gray-matter grid produced consistent localization across all oscillatory peaks. The reconstructed sources were all localized in the left fronto-temporal region. The use of the full-brain grid resulted in consistent locations of sources in the left temporal lobe for the second model. The sources were localized in the left hemisphere in 6/6 cases for all three models. The results of STKF are visualized in Fig 4.16 and the resulting AIC values are listed in Table 4.5. The AIC values of the STKF were always smaller than the ABIC results of LORETA.

4.3.3 Discussion

The evaluation of the source imaging results of LORETA showed that the sources were always localized outside the FCD. Additionally, we observed a variability in the localization of the seizure onset. The use of the full-brain grid slightly decreased the variability but did not improve

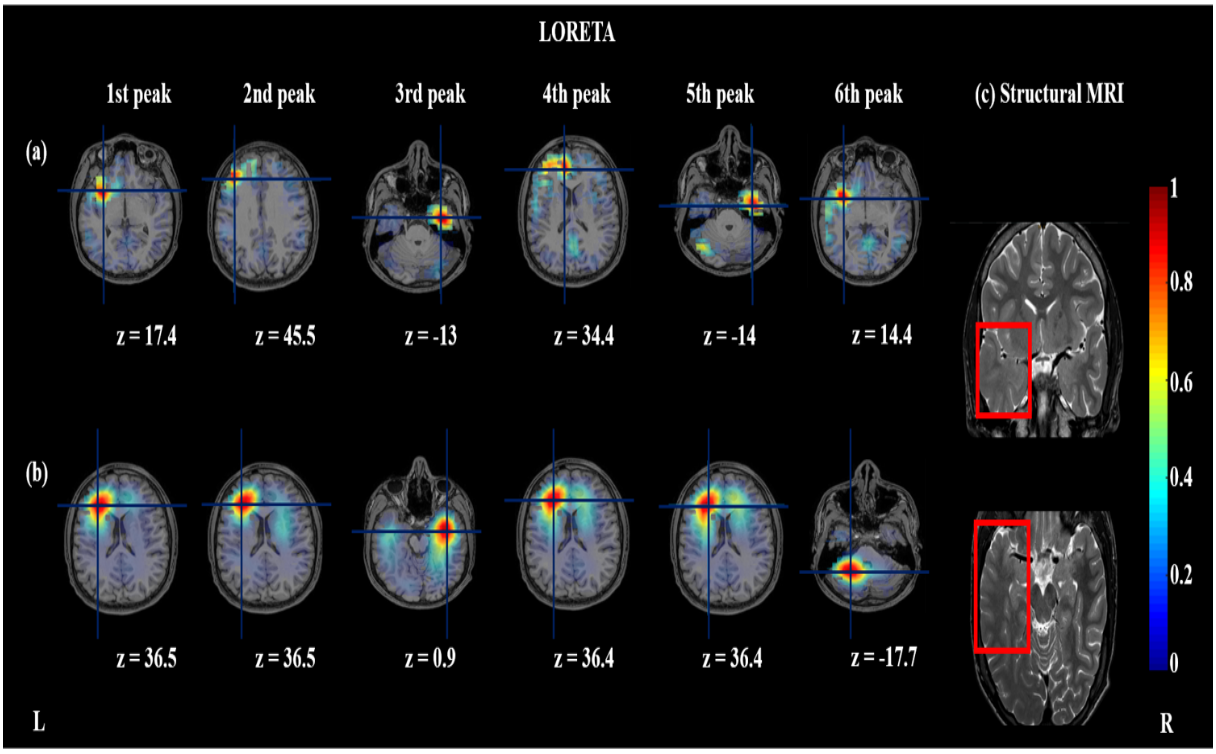

.

Figure 4.15: *Results of EEG source imaging via LORETA of a single focal seizure from the EEG recordings of Patient 3. LORETA results using a gray-matter 3D grid and the classical Laplacian matrix are depicted in (a). Results using a full-brain 3D grid and the classical Laplacian matrix are shown in (b). From left to right the results of seizure peaks 1-6 are shown in columns 1-6, respectively. The results are visualized as axial MRI slices at each seizure peak and the cursor is placed at the maximum of the estimated current density. Additionally the z-coordinates of the axial slices are shown in Montreal Neurological Institute (MNI) coordinates. (c) The location and the extent of the FCD on a coronal (top) and an axial (bottom) slice from the patient's preoperative T2-weighted MRI are shown and marked with red squares. The source imaging results were visualized using the Fieldtrip software [OFMS11]. The figure was adapted from the figures supervised or published by the author in [Sar14, HSJ$^+$15]*

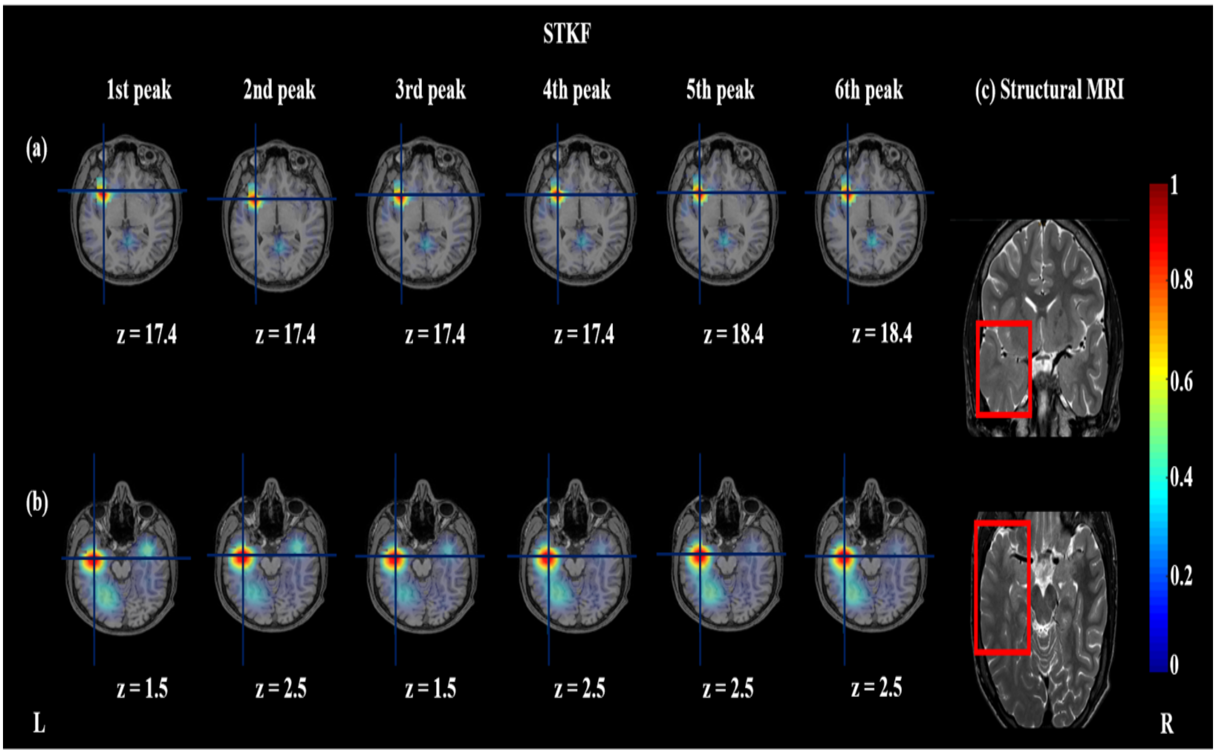

.

Figure 4.16: *Results of EEG source imaging via STKF of a single focal seizure from the EEG recordings of Patient 3. STKF results using a gray-matter 3D grid and the classical Laplacian matrix are depicted in (a). Results using a full-brain 3D grid and the classical Laplacian matrix are shown in (b). From left to right the results of seizure peaks 1-6 are shown in columns 1-6, respectively. The results are visualized as axial MRI slices at each seizure peak and the cursor is placed at the maximum of the estimated current density. Additionally the z-coordinates of the axial slices are shown in Montreal Neurological Institute (MNI) coordinates. (c) The location and the extent of the FCD on a coronal (top) and an axial (bottom) slice from the patient's preoperative T2-weighted MRI are shown and marked with red squares. The source imaging results were visualized using the Fieldtrip software [OFMS11]. The figure was adapted from the figures supervised or published by the author in [Sar14, HSJ$^+$15]*

Datasets	ABIC values of LORETA Results	AIC values of STKF Results
Gray-matter grid, classical Laplacian matrix	14135.1657	-28378.8322
Full-brain grid, classical Laplacian matrix	13306.4868	-19264.8368

Table 4.5: *The table lists ABIC and AIC values resulting from EEG source imaging via LORETA and STKF of the focal seizure from Patient 3. The first analysis was performed using a gray-matter grid and the classical Laplacian matrix. The second analysis was performed using a full-brain grid and the classical Laplacian matrix.*

the accuracy of the localization. We may interpret the assignment of the sources to the frontal lobe by LORETA to the bias introduced by the presence of the stronger oscillations in the frontal electrodes. The variability may have also resulted from the lack of temporal smoothness in the constraints used by LORETA. The slight improvement in consistency of localization after the use of full-brain grids may partially confirm the first hypothesis.

The STKF results were all consistently localized in the left hemisphere.The variability of localization was not observed here. The fronto-temporal source that was shown by the results of the gray-matter grid was outside the FCD and it may have been caused by the presence of thin regions due to spatial sampling of the grid and by the bias introduced by the use of the classical Laplacian matrix that forces the activity at the borders of the grid to be zero. The results of the second model were inside the FCD and this improvement in accuracy may have been the result of the use of full-brain grids in addition to the temporal smoothness constraints of the STKF that are imposed by the dynamical AR(2) model. The STKF results confirm both hypotheses.

We would like to mention some of the limitations of the study. Since this is a proof-of-concept study, we used only a single focal seizure. The consistency and accuracy of the STKF can be better studied within the framework of a larger study that includes multiple subjects with several focal seizure per subject. The oscillatory seizure pattern here was successfully analyzed by the linear STKF. The investigation of more complex focal seizure patterns may require the application of non-linear Kalman filters such as the extended [SSM62, McE66] or unscented Kalman filters [JUDW95]. The former works well in the presence of weak non-linearities while the latter is used in the case of strong non-linear behavior [Sch12].

To summarize, this is the first application of the STKF to the localization of the onset of a focal seizure. The STKF results were compared to those of LORETA. STKF produced correct results only when a full-brain grid was used. STKF outperformed LORETA, probably due to the dynamical nature of the STKF, with respect to the accuracy and consistency of localization for all six oscillatory peaks.

4.4 MEG-EEG Fusion via the Spatiotemporal Kalman Filter

The results in this section were published by the author in [HAW$^+$13].

4.4.1 Methods

The spikes were extracted from the recordings of Patient 4, a teenage female patient with drug-resistant mesial temporal lobe epilepsy. The source of the epilepsy is an FCD in the left temporal lobe. Evaluation of EEG recordings showed left fronto-temporal activity in interictal EEG and left frontal activity in ictal EEG. PET recordings show a deactivation in the left mesial temporal area.

Our cooperation partners from the "Institute for Biomagnetism and Biosignalanalysis" at the University of Münster recorded 500 s of simultaneous MEG-EEG at a sampling frequency of 1.2 KHz. The recording was made using a 275-sensor CTF MEG device (CTF, MEG International Services Limited, Coquitlam, Canada). A 74-electrode EEG was recorded simultaneously with the MEG within the shielded chamber. The layouts of the MEG sensors and EEG electrodes are displayed in Fig 4.17.

Three kinds of MRIs (T1-weighted MRI, T2-weighted MRI, and DT-MRI) were registered using a 3.0 Tesla machine (Gyroscan Intera/Achieva 3.0T (Philips, Best, NL)). The T1-weighted and T2-weighted MRIs had resolutions of ($1.17 \times 1.04 \times 1.04$ mm^3) and ($1.17 \times 1.17 \times 1.17$ mm^3), respectively. The DT-MRI had a resolution of ($1.875 \times 1.875 \times 1.875$ mm^3). In the first step the T2-weighted MRI was coregistered to the T1-weighted MRI and the betsurf tool [JPS$^+$05] from the FSL software [JBB$^+$12] was used to segment the scalp, outer skull, and inner skull. The FAST tool [ZBS01] also from FSL was then used to extract the brain's white matter, CSF, and gray matter. The spongy skull bone is detected using threshold-based segmentation of the T2-weighted image followed with constraints from a morphologically-transformed skull overlay. The recording and processing of DT-MRI are explained in detail in [AVK$^+$14, AVD$^+$15]. The conductivity tensors that describe the anisotropy of the gray- and white matter was extracted from the ST-MRI after preprocessing and coregistration to the T2-weighted MRI. Finally, SimBio-VGRID [C$^+$00] is used to compute a 6-compartment hexahedral mesh with white- and gray-matter anisotropy and adaptation of geometry. SimBio [C$^+$00] was used to compute the magnetic and electrical LFMs with conductivity values of 0.43 S/m, 0.007 S/m, 0.025 S/m, 0.14 S/m, 0.33 S/m, and 1.79 S/mm for scalp, compact skull bone, spongy skull bone, white matter, gray matter and CSF, respectively. The conductivity of the skull was adapted to the patient's anatomy using skull conductivity estimation from additional simultaneous measurements of sensory evoked fields and potentials.

The simultaneous MEG-EEG recordings were preprocessed and the spikes were marked by expert epileptologists. For the analysis, we chose a spike that was visible in both MEG and EEG. The chosen spike was strongest in the MEG MLT21 channel and in the EEG FT9 electrode as can be seen in Fig 4.18 [1]. Please note that the peak of the MEG spike at T_M precedes that

---

[1] In this figure, the negative spike peak in the EEG dataset is plotted pointing downwards.

of the EEG spike at T_E by 20 ms. Additionally, the stronger distortion of surface EEG by volume conduction makes the EEG spike look more smeared compared to the MEG spike. We then reduced the number of channels to 64 MEG and 64 EEG channels, and then standardized the data from each modality. The EEG data was then average-referenced. The SNR values of the MEG and EEG spikes were calculated according to the procedure explained in section 2.1. The 64-channel MEG, 64-channel EEG, and the 128-channel simultaneous MEG-EEG datasets were analyzed using STKF with an autoregressive model as the dynamical model. The source space was defined using a gray-matter grid with 4.5648 mm resolution and the classical Laplacian matrix was used. The results were visualized at the peak T_M of the MEG spike and at the peak T_E of the EEG spike. An overview of the MEG-EEG source imaging procedure is available in Fig 4.20. The results were visualized using the Fieldtrip Software [OFMS11].

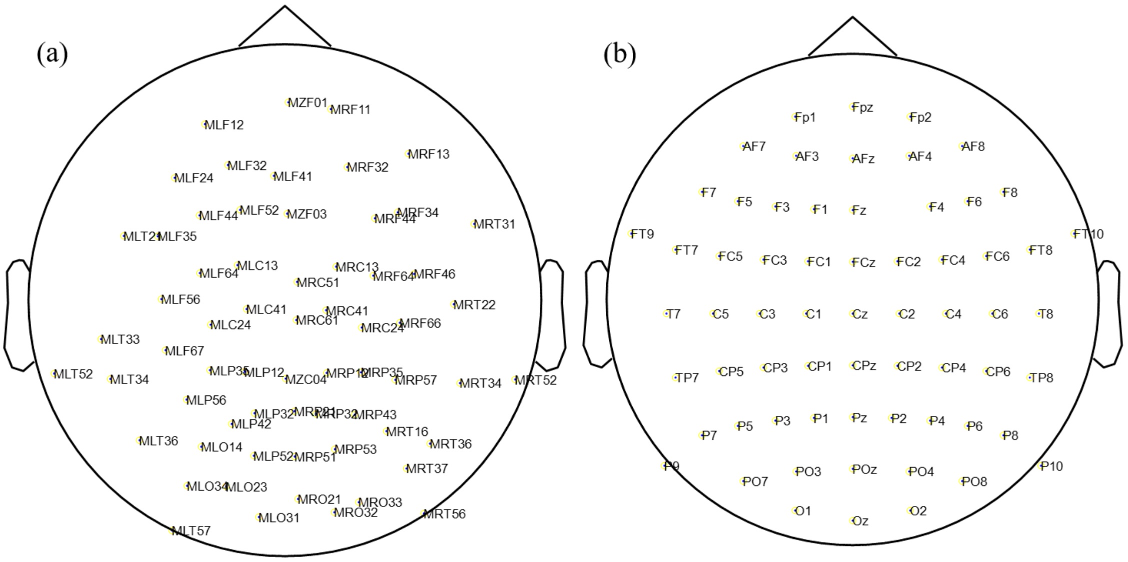

.

Figure 4.17: *(a)The figure displays the 64-channel MEG sensor layout that was used to select 64 out of 271 MEG channels from Patient 4's recordings. In (b) the 64-channel electrode layout that was used to select 64 out of 74 EEG channels from Patient 4's recordings is shown. The layouts were visualized using the Fieldtrip software [OFMS11].*

4.4.2 Results

For the MEG spike, the SNR value when only the background signal of sensor MLT21 is taken into account is 20.9987 dB. The SNR value of the EEG spike at electrode FT9 is 15.6855 dB. The source imaging results via STKF of MEG-only, EEG-only, and MEG-EEG datasets are shown in Fig 4.21. Using the EEG-only dataset, we can see that at the MEG peak T_M, STKF finds the source in the right occipital lobe. At the EEG peak T_E, STKF estimates the source in

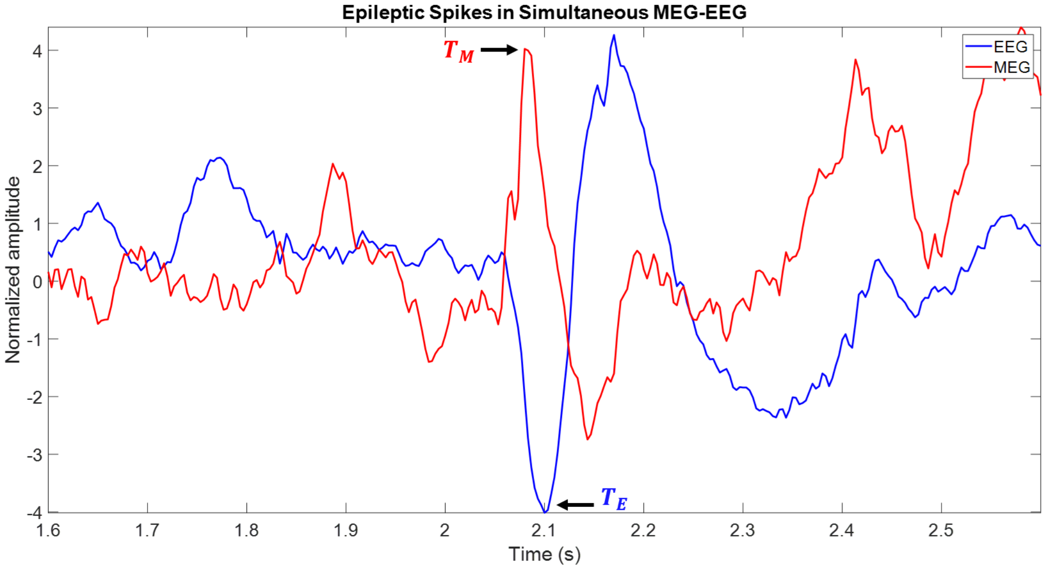

.

Figure 4.18: *The epileptic spikes from the time series of MEG channel MLT21 (in red) and EEG channel FT9 (in blue) are shown.* T_M *marks the peak of the MEG spike and* T_E *marks the peak point of the EEG spike. The figure was adapted from a publication by the author [HAW*$^+$*13].*

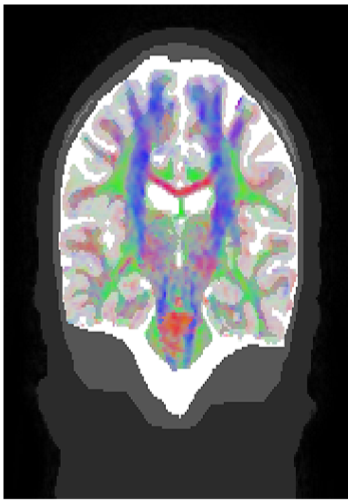

Figure 4.19: *The figure shows the 6-compartment calibrated finite element head model that was generated from Patient 4's structural T1-weighted, T2-weighted and DTI MRI recordings. The colors red, blue, and green indicate right to left, superior to inferior, and anterior to posterior directions, respectively.*

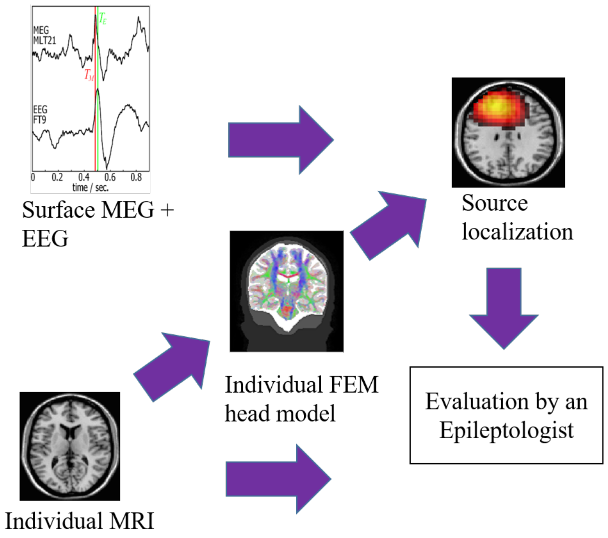

Figure 4.20: A summary of the analysis pipeline is presented which includes MEG-EEG preprocessing, MRI preprocessing, finite element individual head modeling, source imaging via STKF, and evaluation based by an expert epileptologist. The images were produced using CURRY7.

the left lateral temporal lobe. The results of the MEG-only dataset at the MEG peak T_M show a single source in the left lateral temporal lobe. At the EEG peak T_E, the source was localized in the left cerebellum. Using the MEG-EEG dataset, STKF found the source in the left lateral temporal lobe at both peaks.

If we concentrate only at the expected area in the left lateral frontal area we find a weak activation from the EEG-only dataset at the MEG peak T_M that does not appear as the strongest source. The same can be said for the result from the MEG-only dataset at the EEG peak T_E.

4.4.3 Discussion

In this study, MEG-EEG fusion was performed in the forward as well as in the inverse modeling steps. In the forward model a 6-compartment anisotropic FEM head model with calibrated skull conductivity was computed to account for the different sensitivities of MEG and EEG to the human skull. In the inverse step, the measurement model of the state-space model that underlies the STKF was generalized to describe both MEG and EEG. The results show improved accuracy and consistency of the STKF when the simultaneous MEG-EEG dataset was analyzed, since this means that information from both modalities were available to the STKF. Since MEG is more sensitive to dipoles with a dominant tangential orientation and EEG is more sensitive to dipoles with a dominant radial orientation, MEG and EEG are complementary and MEG-EEG fusion would provide a more complete picture of the underlying current density distribution in the brain. The results support our hypothesis.

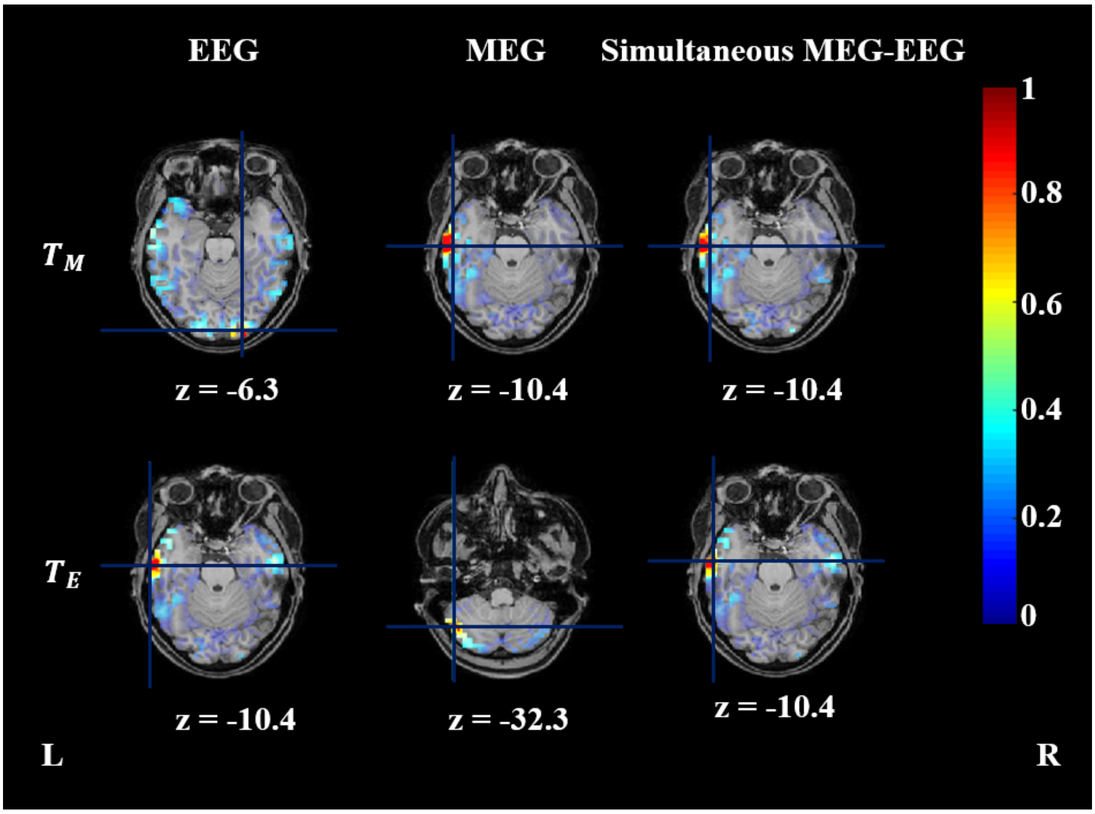

.

Figure 4.21: *Results of EEG source imaging via STKF of a non-averaged epileptic spike from the simultaneous MEG-EEG recordings of Patient 4. In the top row, STKF results are shown at the MEG peak* T_M*. STKF results at the EEG peak* T_E *are shown in the bottom row. From left to right the results of EEG, MEG and simultaneous MEG-EEG are shown, respectively. The results are visualized as axial MRI slices at each spike's peak and the cursor is placed at the maximum of the estimated current density. Additionally the z-coordinates of the axial slices are shown in Montreal Neurological Institute (MNI) coordinates. The source imaging results were visualized using the Fieldtrip software [OFMS11]. The figure was adapted from a publication by the author [HAW*$^{+}$*13].*

In this study only a single epileptic spike was analyzed. A large-scale study involving multiple subjects is required in order to study the consistency of the STKF's results in MEG-EEG fusion. Additionally, we only used 64 channels from each modality. In the future the inclusion of more channels may help to further improve the accuracy of STKF. The results from the gray-matter grid may be even further improved by using a full-brain grid. The combination of the full-brain grid with the modified definition of the Laplacian matrix may bring even better results. Finally, temporally- or spatially-adaptive dynamical models may outperform the current AR(1) dynamical model with constant parameters.

In summary, this is the first application of the STKF to simultaneous MEG-EEG. This has been done by generalizing the measurement equation from the state-space model. Additionally, a state-of-the-art 6-compartment anisotropic FEM head model with calibrated skull conductivity was used to improve forward modeling of simultaneous MEG-EEG data.The source imaging results of the MEG-EEG dataset were more accurate than those of the MEG-only or EEG-only datasets. This may have been the case due to the complementarity of MEG and EEG recordings.

Chapter 5

Source Imaging of Simulated and Clinical EEG Data via the Regional Spatiotemporal Kalman Filter

5.1 Motivation

The STKF is limited by the decision to keep its state-space model parameters constant in time and in space. The first experiments with spatially-heterogeneous parameters were performed within the framework of the diploma thesis of Philipp Stern [Ste08]. In this diploma thesis, he implemented the first regional STKF (RSTKF). In order to test the new algorithm, two regions were defined in the brain. The first region included the left and right thalami while the second region included the rest of the brain's gray matter. He chose to use region-specific dynamical noise variance parameters, since this parameter was found, in practice, to be more important for state-space modeling of EEG data. The cerebellum was excluded from the source space. In his thesis, Philipp Stern used a standard 3-spheres head model and a gray-matter grid. He also used the classical Laplacian matrix throughout the thesis. He first worked on simulated EEG data from a rotating dipole in the thalamus. Stern hypothesized that the stochastic change of the orientation uses the fact that the EEG is highly sensitive to the dipole orientation. The dynamical nature of the Kalman filter would then assume a deep source with a changing orientation rather than a cortical patch that spans the whole cortex.

RSTKF was successful in localizing the thalamic source while LORETA and STKF failed in this task. Compared to the rest of the brain, the optimization step resulted in a larger dynamical noise variance in the thalamus. In the rest of the thesis he also tested simulated EEG data where a cortical and a thalamic source were simultaneously active, which led to a masking of the activity of the deeper source. In this case, prior separation of the activity of both sources using frequency-domain filtering was enough to obtain accurate results via the RSTKF. He also analyzed two clinical EEG datasets. In the first dataset he tried to localize a thalamic source from the EEG recordings of a opiate-dependent patient undergoing rapid detoxification.

RSTKF was successful in localizing the thalamic source, which was believed to be the only active source in the brain. The second dataset was an EEG recording of sleep spindles. In this case, the thalamic source was found after multiple processing stages including regional definition, frequency-domain filtering to exclude masking effects, and an initial grid search followed by quasi-Newton BFGS optimization.

In the above-mentioned thesis, the author limited the RSTKF to two regions. No individual or realistic head models were used by the author. He also did not investigate the effects of the grid choice or the Laplacian matrix on the RSTKF. Additionally, the applicability of the new method to epileptology was not investigated.

In this work, we wanted to apply the RSTKF to simulated as well as clinical EEG data of epileptic spikes. We also wanted to increase the number of regions from two to seven and check whether this negatively influences the optimization process, since we don't perform the optimization in two stages namely, a global optimization and then a regional one. We also wanted to investigate the applicability of the RSTKF to the localization of other interesting subcortical regions such as the putamen or the amygdalo-hippocampal complex. In contrast to Philipp Stern's thesis, we use realistic head models and different grids that include the cerebellum and the white matter. We also decided to constrain our investigation to the localization of single sources. A subset of the results of this chapter that is related to the analysis of the simulated EEG from the thalamic source was produced in the master thesis of Nawar Habboush [Hab14], which was supervised by the author within the framework of this doctoral thesis. The results of this chapter were submitted by the author as a journal paper to PLOS ONE and the paper is currently under review.

We hypothesize that RSTKF will perform similarly to STKF and LORETA with respect to cortical sources. With increasing depth of sources, we expect RSTKF to become more accurate. We also expect RSTKF to show improved accuracy, consistency of localization, and spatial resolution in case of small lesions such as hippocampal sclerosis. Finally, we expect a better performance of RSTKF in statistical model comparison compared to that of STKF or LORETA.

5.2 Methods

5.2.1 Simulated EEG Data

In this section two experiments were performed. In the first experiment, three simulated EEG datasets were generated from rotating dipoles that were placed in the frontal lobe, putamen, and thalamus, respectively. The increase in the depth of the sources was used to test the localization performance of LORETA, STKF, and RSTKF(7), which denotes a 7-region RSTKF. In the second experiment, the simulated EEG datasets from a rotating dipole in the thalamic source was used to test the localization performance of RSTKF with two to seven regions.

The source dynamics in the brain were generated with a frequency of 4.8 Hz and a sampling frequency of 256 Hz using an autoregressive model of second order. This signal was used to simulate a single dipole first in the left frontal lobe, then in the left putamen, and finally in the left thalamus, respectively. The source orientation varied stochastically in the plane around the line extending between the left and right ears. An example of a rotating dipole and its source dynamics is shown in Fig 5.1.

The LFM was computed from the standard realistic BEM head model from the Neuroscan Curry software (Compumedics Neuroscan, version 7.0). The three-compartment head model includes the skin, outer skull, and inner skull compartments which were triangulated using 1504, 2681, and 3858 nodes, respectively. Their conductivity values were set to 0.33 S/m, 0.0042 S/m, and 0.33 S/m, respectively. The brain was discretized using a volumetric grid with a grid resolution of 5 mm. The electrode positions were described by the layout depicted in 5.2.

The three simulated EEG datasets were then generated by the multiplication of the brain signals with the resulting LFM and the subsequent addition of -80 dB white Gaussian measurement noise. The resulting SNR values of the EEG datasets from the sources in the frontal lobe, putamen, and thalamus were 45.77 dB, 44.05 dB, and 42.62 dB, respectively. The simulated EEG data sets are shown in Fig 5.3.

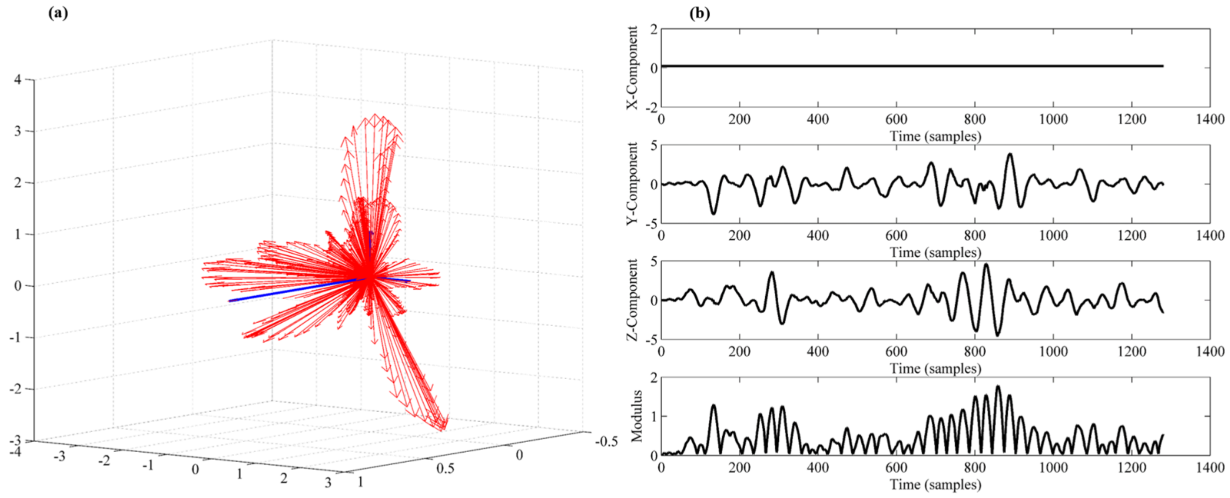

.

Figure 5.1: (a) An example of the simulated rotating current dipole in the thalamus and (b) the x-, y- and z-components in addition to the modulus of the thalamic source current density $(\mu A/mm^2)$.

In the preprocessing step, standardization of data was performed to zero mean and unit variance. Additionally, the data was re-referenced to the common average reference. In the inverse modeling step, we performed EEG source imaging in the first experiment via LORETA, STKF, and RSTKF(7). The simulated EEG datasets from the sources in the frontal lobe, putamen, and thalamus were used for the analysis. In the second experiment, the EEG dataset from the thalamic source was analyzed via LORETA and RSTKF(2-7). No five-region model was used in this experiment. An autoregressive model of second order was used for the dynamical models of STKF and RSTKF. The standard BEM head model from CURRY7 was also used here. An

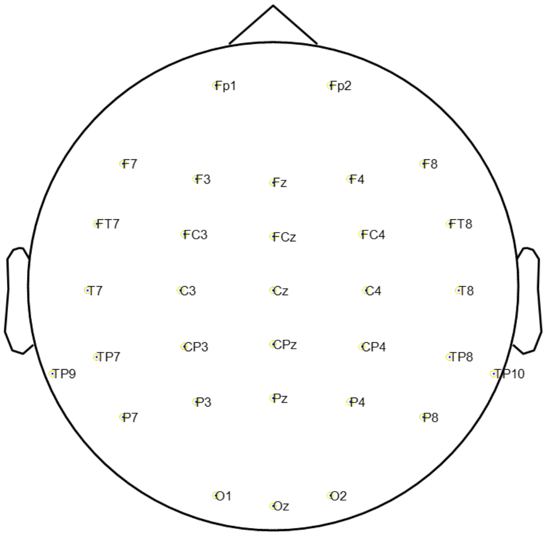

.

Figure 5.2: *The 32-channel EEG electrode layout used for generating the simulated EEG datasets. The layout was visualized using the Fieldtrip Software [OFMS11].*

overview of the source imaging pipeline is shown in Fig 5.4.

The source grid points needed to be grouped into different regions based on the Talairach Atlas from CURRY7. We started with a similar model like the one used in Philipp Stern's thesis [Ste08]. The thalamus was distinguished from the rest of the brain in the two-region model. In the three-region model, the rest of the brain was divided into left and right hemispheres in addition to the thalamic area. The hippocampus was added in the four-region model. The cerebellum and the putamen were included in the six-region model and, finally, the seventh region was chosen to be the caudate nucleus in the seven-region model. We did not divide the subcortical structures into left and right regions. The choice of the thalamus, hippocampus, putamen, and caudate nucleus was based on [ABY$^+$07, AMFD12, Ste08]. The cerebellum was modeled because of its connectivity with the cortex and its participation in the areas of language and attention [MI16].

The grid spacing differed in the different RSTKF analyses. The grid resolution in the inverse modeling step was never set to 5 mm to avoid inverse crime where the same model is used for both simulation and source reconstruction. The classical 7 mm resolution was used for the six- and seven-region analyses. The four-region model was analyzed using a grid with 6 mm resolution. Finally, 14 mm resolution was used for the two- and three-region models. This variability in the grid resolution resulted from considerations about computational time. After that, we experimented with the grid resolution to model longitudinal brain regions such as the hippocampus, since they were discontinuously sampled or did not have enough grid points when a coarse grid resolution was used. We finally settled on 7 mm resolution with additional dilation and smoothing of the small and longitudinal subcortical structures.

In order to be able to compare the localization and ABIC and AIC results of LORETA

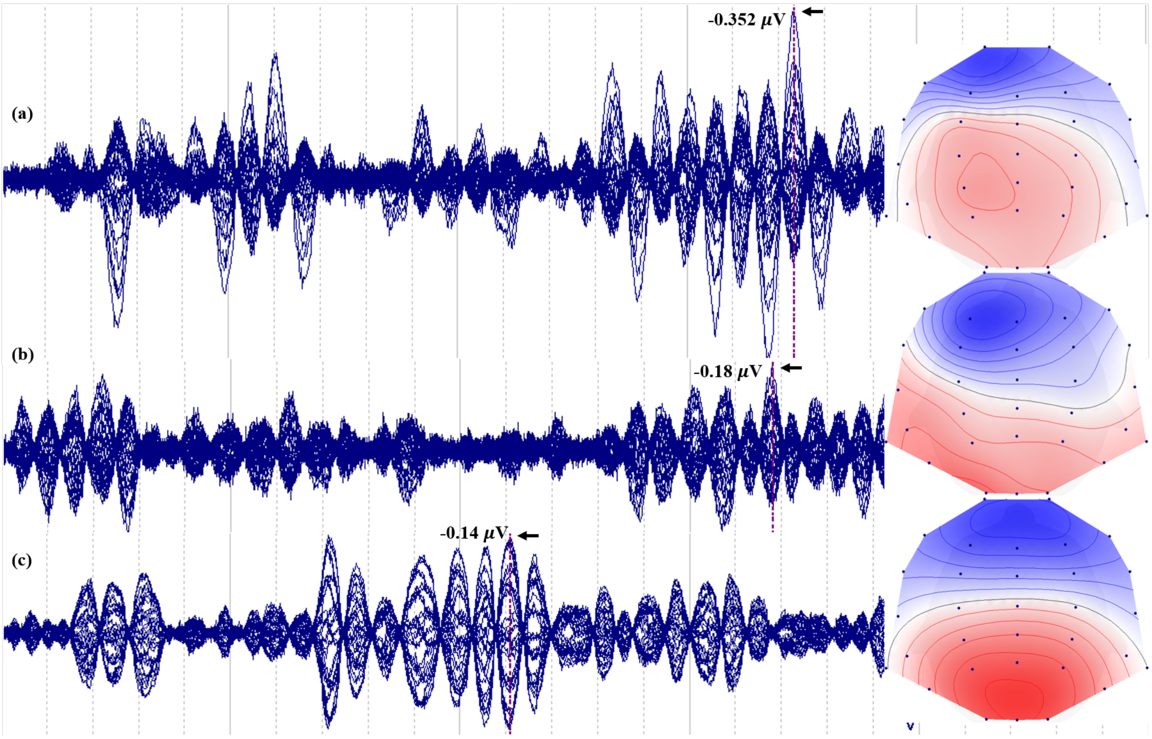

.

Figure 5.3: *The simulated 32-channel EEG data sets from a single rotating dipole in (a) the frontal lobe, (b) putamen, and (c) thalamus. For each dataset, the oscillatory peaks that were used to visualize the source imaging results are shown using cursors and arrows. The EEG amplitudes at the oscillatory peaks are shown next to the peak points. In the right column the voltage maps of the largest negative peaks of every data set are shown. The images were produced using CURRY7.*

and RSTKF(2-7), the six- and seven-region models were computed out-of-sample because they were optimized using another interval from the dataset compared to the other four models.

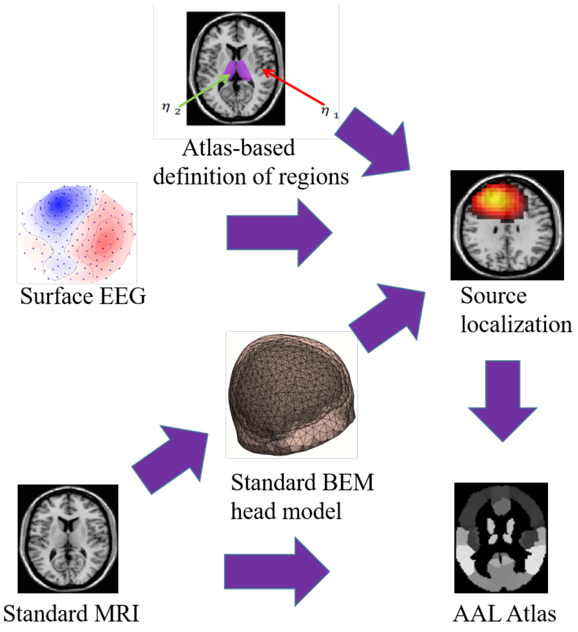

.

Figure 5.4: *A summary of the analysis pipeline is shown which includes EEG preprocessing, head modeling, division of brain grid into regions based on atlas information, source imaging, and evaluation based on an anatomical atlas. The images were produced using CURRY7.*

5.2.2 Clinical EEG Data

We have seen in section 4.2 that neither LORETA nor STKF were successful in demonstrating good accuracy and spatial resolution using EEG recordings from Patient 2, since the resected area was small and deep. In this section we decided to test the new RSTKF method using the same data from Patient 2 and compare the results to those of LORETA and STKF. In the preprocessing step, the data were also standardized and re-referenced to the common average reference. Unlike the analyses in 4.2, we used here the standard 3-compartment BEM head model from CURRY7, since it was easier to perform the regional grouping of grid points into regions using the standard head. Additionally, we also used a full-brain grid with 7 mm grid resolution in addition to the classical Laplacian matrix.

The 7-region model was used here for RSTKF and it included the thalamus, the amygdalo-hippocampal complex, the putamen, the caudate nucleus, the cerebellum, and the remainder of the brain which was divided into left and right hemispheres. No left and right distinctions were used for the subcortical areas. Since we used a grid resolution of 7 mm, we needed to use dilation and smoothing to make sure that every subcortical region was correctly meshed.

Method	Euclidean distance (in mm) between the simulated and reconstructed sources in the frontal lobe	Euclidean distance (in mm) between the simulated and reconstructed sources in the putamen	Euclidean distance (in mm) between the simulated and reconstructed sources in the thalamus
LORETA	12.8062	20.8327	25.7099
STKF	15.2971	20.3224	24.5967
RSTKF	12.8062	16.0935	11.3578

Table 5.1: *Euclidean distances (in mm) between the maxima of the simulated and the maxima of the sources reconstructed via LORETA, STKF, and RSTKF.*

The results of LORETA, STKF, and RSTKF(7) were evaluated using visual inspection, since the post-surgical resection as seen in the patient's MRI is available, and atlas labels of the maxima of the reconstructed activity using the anatomical automatic labeling (AAL) atlas [TMLP$^+$02]. The anatomical descriptions of the AAL labels are listed in Table 3.1, Table 3.2, and Table 3.3.

5.3 Results

5.3.1 Simulated EEG Data

For all simulated datasets, the optimization step did not become slow near convergence or fall in a local minimum very early in the optimization process. For the EEG dataset from the frontal lobe, LORETA localized the source in the white matter near the gray matter in the left frontal area. LORETA localized the source from the putamen in the white matter. The thalamic source was localized by LORETA in the left putamen. STKF localized the frontal source in the white matter in the left frontal region. The source from the putamen was localized by STKF in the white matter. STKF localized the source from the thalamus in the left putamen. RSTKF(7) localized the frontal source in the white matter near the gray matter in the left frontal area. The source from the putamen was localized in the left putamen. The thalamic source was localized in the left thalamus.

The lowest AIC values were produced by RSTKF(7) followed by STKF. ABIC values of LORETA were the highest. The distances between the simulated and the maxima of the reconstructed current density distributions are listed in Table 5.1. The source imaging results of these analyses can be seen in Fig 5.5 and the resulting anatomical labels, AIC values and evaluation are listed in Table 5.2. The regional dynamical noise standard deviations are listed in Table 5.3. We observe here that the dynamical noise variance parameter of the simulated region had a higher value as a result of the optimization step compared to the dynamical noise variances of the other six regions.

EEG source imaging results from the second experiment can be seen in Fig 5.5. The anatom-

Datasets	Anatomical labels of LORETA result	Anatomical labels of STKF result	Anatomical labels of RSTKF result
7-region grid, EEG from the source in the frontal lobe	N \A -DC- 8877.9711	N \A -DC- 2242.2276	N\A -DC- 1678.4294
7-region grid, EEG from the source in the putamen	N \A -DC- 6077.9396	N \A -DC- 2588.3301	Putamen L -C- 2434.9579
7-region grid, EEG from the source in the thalamus	Putamen L -DC- -3015.4937	Putamen L -DC- -7506.8781	Thalamus L -C- -7584.5813

Table 5.2: *EEG source imaging results via LORETA, STKF, and RSTKF of three simulated EEG datasets generated from sources in the frontal lobe, putamen, and thalamus, respectively. For the maximum source activation, anatomical labels from the AAL atlas are shown. If the maximum of the estimated source activity falls within the simulated region, the result is concordant, -C-, with the simulated region; if the maximum does not fall within the simulated region, the result is disconcordant, -DC-, with the simulated region.*

Regions	Frontal lobe	Putamen	Thalamus
Thalamus	-14.456	-17.087	-5.019
Hippocampus	-15.091	-17.378	-39.974
Cerebellum	-17.637	-5.491	-49.723
Putamen	-17.432	-4.972	-39.867
Caudate nucleus	-14.393	-21.835	-5.916
Cortex left	-3.988	-5.699	-7.373
Cortex right	-8.506	-19.946	-7.656

Table 5.3: *The table shows the RSTKF's regional dynamical noise standard deviations estimated from the simulated EEG dataset from the sources in the frontal lobe, putamen, and thalamus. For each value, the natural logarithm of the standard deviation is shown. The number of regions was set to seven in the analyses.*

ical labels and the evaluation are shown in Table 5.4.The regional dynamical noise standard deviations that resulted from the parameter estimation step are listed in Table 5.6. The thalamus was correctly localized by RSTKF with two to seven regions. While RSTKF(4) localized the source maximum in the right thalamus, all other models localized the source maxima in the left thalamus. The AIC values of RSTKF were always lower than the ABIC results of LORETA. These values are listed in Table 5.5. Additionally, the regional dynamical noise variance of the thalamus was always higher than the dynamical noise variances of the other regions.

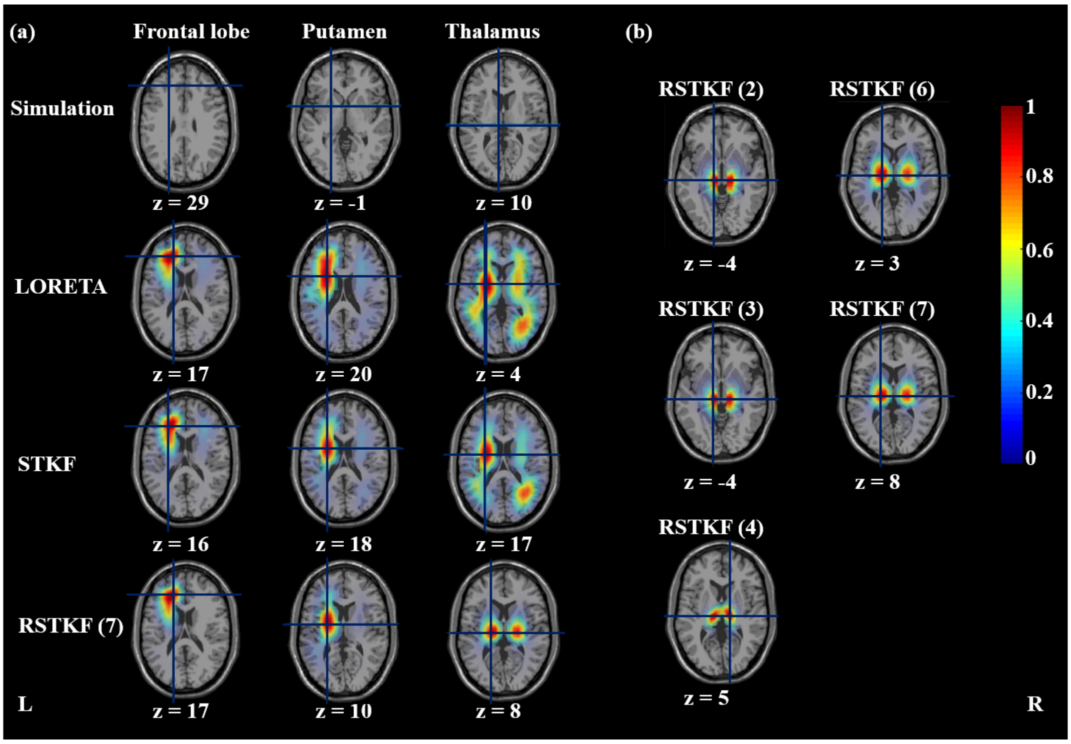

.

Figure 5.5: (a) The first row shows the locations of the simulated dipoles in the left frontal lobe (left), left putamen (center) and thalamus (right). In the second row the EEG source imaging results of LORETA for the sources in the frontal lobe, putamen, and thalamus are displayed. In the third row the EEG source imaging results of STKF for the sources in the frontal lobe, putamen, and thalamus are displayed. In the bottom row the EEG source imaging results of the RSTKF(7) for the sources in the frontal lobe, putamen, and thalamus are shown. (b) EEG source imaging results of the RSTKF(i), where $i = 2,,7$, for the simulated thalamic source. The results are visualized as axial MRI slices, and the cursor is placed at the maximum of the estimated current density. Additionally the z-coordinates of the axial slices are shown in Montreal Neurological Institute (MNI) coordinates. The source imaging results were visualized using the Fieldtrip software [OFMS11].

Datasets	Anatomical labels of RSTKF result
2-region grid, EEG from the thalamic source	Thalamus L -C-
2-region grid, EEG from the thalamic source	Thalamus L -C-
4-region grid, EEG from the thalamic source	Thalamus R -C-
6-region grid, EEG from the thalamic source	Thalamus L -C-
7-region grid, EEG from the thalamic source	Thalamus L -C-

Table 5.4: *EEG source imaging results via RSTKF of the simulated EEG dataset from the thalamic source. For the maximum source activation, anatomical labels from the AAL atlas are shown. If the maximum of the estimated source activity falls within the simulated region, the result is concordant, -C-, with the simulated region; if the maximum does not fall within the simulated region, the result is disconcordant, -DC-, with the simulated region.*

Datasets	ABIC values of LORETA result	AIC values of RSTKF result
2-region grid, EEG from the thalamic source	-2812.5595	-7854.0669
3-region grid, EEG from the thalamic source	-2812.5595	-7825.7634
4-region grid, EEG from the thalamic source	-2515.0444	-7680.7137
6-region grid, EEG from the thalamic source	-3015.4937	-7589.3317
7-region grid, EEG from the thalamic source	-3015.4937	-7584.5813

Table 5.5: *The table lists ABIC and AIC values resulting from EEG source imaging via LORETA and RSTKF of the simulated EEG dataset from the thalamic source. ABIC values of LORETA vary because more than one grid was used for the analysis with different number of regions. The number of regions was varied from 2 to 7 in the analyses.*

Regions	2 regions	3 regions	4 regions	6 regions
Thalamus	-4.684	-4.486	-5.638	-5.284
Hippocampus	-	-	-15.084	-37.666
Cerebellum	-	-	-	-6.797
Putamen	-	-	-	-6.630
Caudate nucleus	-	-	-	-
Cortex left	-23.500	-14.703	-9.948	-7.351
Cortex right	-23.500	-14.534	-8.607	-7.559

Table 5.6: *The table shows the RSTKF's regional dynamical noise standard deviations estimated from the simulated EEG dataset generated from the thalamic source. For each value, the natural logarithm of the standard deviation is shown. The number of regions was varied from two to six in the analyses.*

5.3.2 Clinical EEG Data

The source reconstruction results via LORETA, STKF, and RSTKF at onset of the five spikes from Patient 2 are shown in Fig 5.6. The anatomical labels of the source maxima, the AIC results, and the evaluation of the accuracy of LORETA, STKF, RSTKF are listed in Table 5.7. The regional dynamical noise standard deviations that resulted from the parameter estimation step are listed in Table 5.9. At spike onset, LORETA localized the source in the right calcarine, white matter, white matter, middle temporal region, and in the left cerebellum, for the five spikes, respectively. STKF produced localizations for spikes 1, 2, 4, and 5 in the middle temporal region. The onset of spike 3 was localized in the left inferior triangular frontal region. RSTKF localized the sources in the left amygdalo-hippocampal complex for spikes 1, 3, 4, and 5. The onset of spike 2 was localized in the left hippocampus.

At the spike peak the EEG source imaging results of LORETA, STKF, and RSTKF are displayed in Fig 5.7. The anatomical labels of the source maxima, AIC values, and evaluation of accuracy of LORETA, STKF, and RSTKF are listed in Table 5.8. LORETA localized the sources of the first and fifth spikes in the white matter. The sources of the second and fourth spikes were found in the left middle temporal region by LORETA. The result of spike 3 was estimated in the left inferior temporal region. STKF produced localizations for the second spike in the left middle temporal region. The source of the fourth spike was localized by STKF in the left inferior temporal region. The sources for the first, third and fifth spikes were all estimated in the white matter. RSTKF localized the source maxima at the spike peaks in the left amygdalo-hippocampal complex for all five spikes. The lowest AIC values were shown by RSTKF(7). The AIC results of STKF were higher and ABIC results of LORETA were even higher. The amygdalo-hippocampal complex had the highest dynamical noise variance parameters compared to those of the other regions for all five spikes. The optimization process for the clinical spikes finished without slow convergence or early local minima.

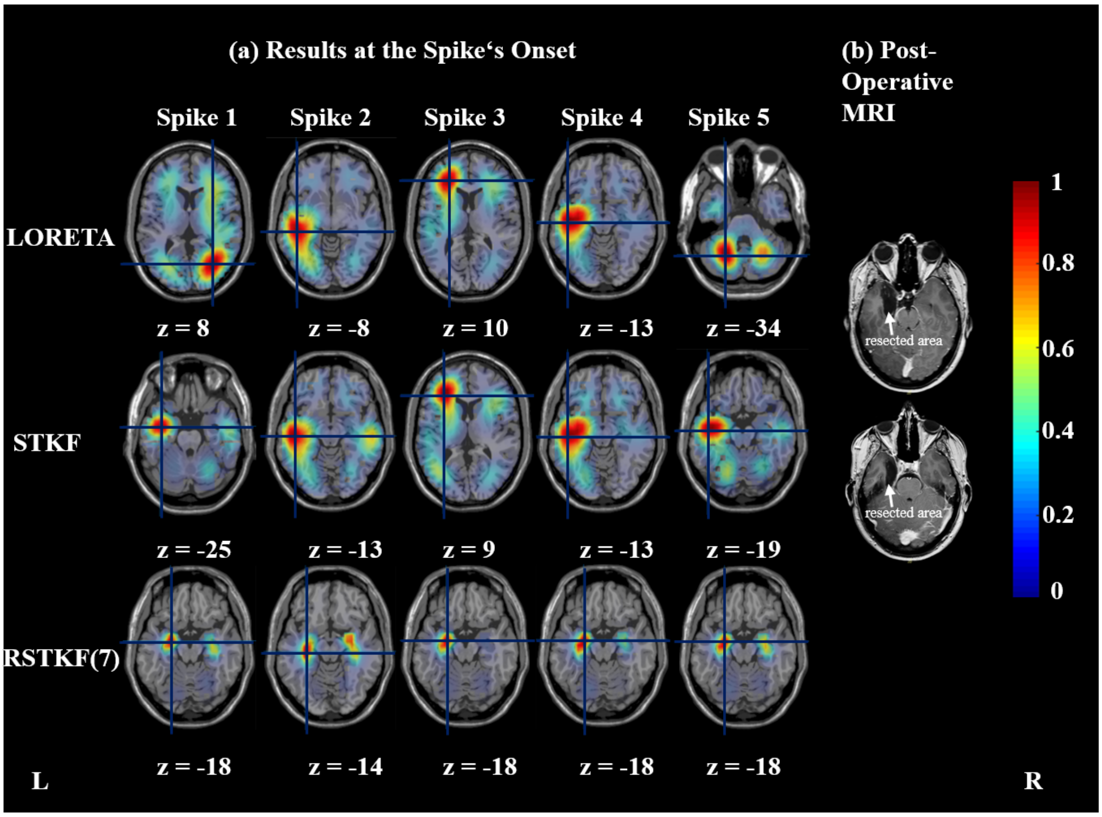

.

Figure 5.6: *(a) EEG source imaging results of 5 non-averaged spikes using LORETA (top row), STKF (middle row) and RSTKF (bottom row). The results are visualized as axial MRI slices at each spike's onset,which is defined as 50% of the spike's rise time, and the cursor is placed at the maximum of the estimated current density. Additionally the z-coordinates of the axial slices are shown in Montreal Neurological Institute (MNI) coordinates. (b) The location and the extent of the resected region in two axial slices from the patient's postoperative MRI. The source imaging results were visualized using the Fieldtrip software [OFMS11]*

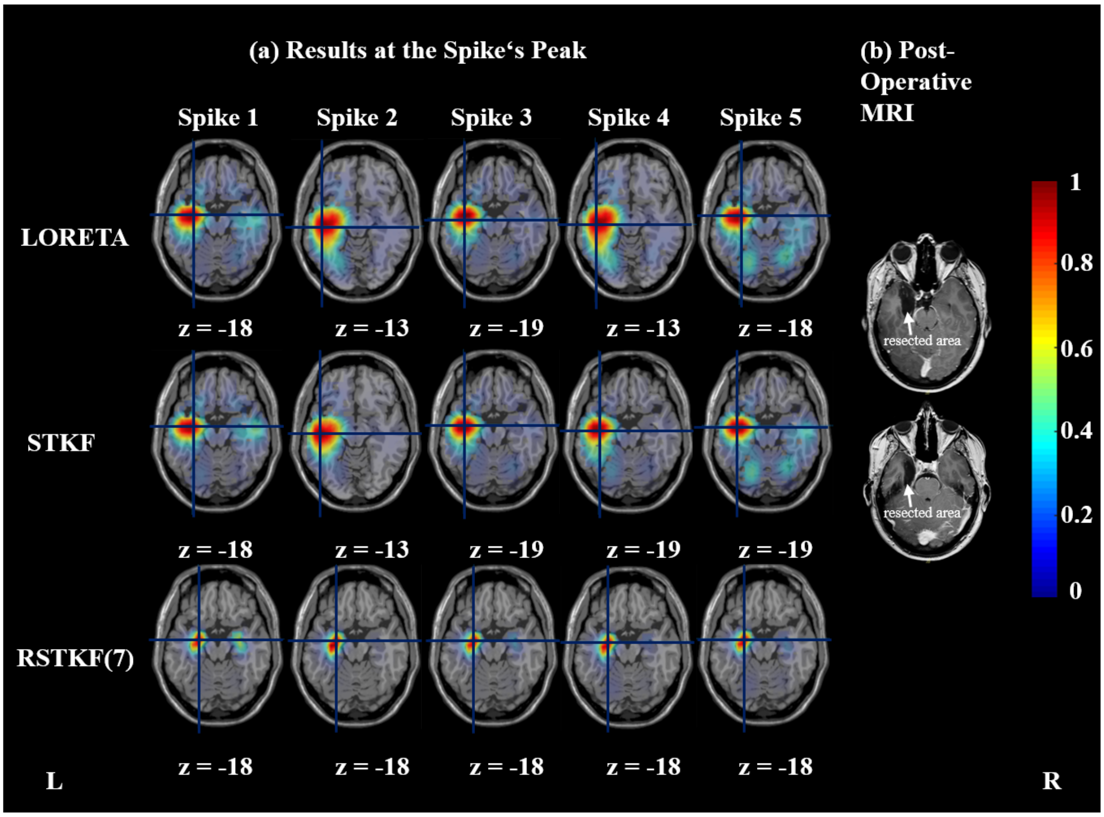

.

Figure 5.7: *(a) EEG source imaging results of 5 non-averaged spikes using LORETA (top row), STKF (middle row) and RSTKF (bottom row). The results are visualized as axial MRI slices at each spike's peak, and the cursor is placed at the maximum of the estimated current density. Additionally the z-coordinates of the axial slices are shown in MNI coordinates. (b) The location and the extent of the resected region in two axial slices from the patient's postoperative MRI. The source imaging results were visualized using the Fieldtrip software [OFMS11]*

Datasets	Anatomical labels of LORETA result	Anatomical labels of STKF result	Anatomical labels of RSTKF result
Spike 1 onset	Calcarine R -DC- 18667.6483	Temporal Mid L -DC- -993.0394	Amygdala L, Hippocampus L -C- -4735.7374
Spike 2 onset	N \A -DC- 9392.563	Temporal Mid L -DC- -6822.979	Hippocampus L -C- -9206.4559
Spike 3 onset	N \A -DC- 14457.6143	Frontal Inf Tri L -DC- -3778.4027	Amygdala L, Hippocampus L -C- -5381.7106
Spike 4 onset	Temporal Mid L -DC- 13791.1576	Temporal Mid L -DC- -4129.7397	Amygdala L, Hippocampus L -C- -6875.335
Spike 5 onset	Cerebellum 6 L, Cerebellum Crus 1 L -DC- 20987.8525	Temporal Mid L -DC- -0.97601	Amygdala L, Hippocampus L -C- -2488.1555

Table 5.7: *EEG source imaging results of five non-averaged spikes selected from the EEG recording of Patient 2. The epileptic focus lies in the amygdalo-hippocampal area. The results were visualized at the spikesâ onsets defined as 50% of the spike's rise time. For the maximum source activation, anatomical labels from the AAL atlas are shown. If the maximum of the estimated source activity falls within the resected region, the result is concordant, -C-, with the resected region; if the maximum does not fall within the resected region, the result is disconcordant, -DC-, with the resected region.*

Datasets	Anatomical labels of LORETA result	Anatomical labels of STKF result	Anatomical labels of RSTKF result
Spike 1 peak	N \A -DC- 18667.6483	N \A -DC- -993.0394	Amygdala L, Hippocampus L -C- -4735.7374
Spike 2 peak	Temporal Mid L -DC- 9392.563	Temporal Mid L -DC- -6822.979	Amygdala L, Hippocampus L -C- -9206.4559
Spike 3 peak	Temporal Inf L -DC- 14457.6143	N \A -DC- -3778.4027	Amygdala L, Hippocampus L -C- -5381.7106
Spike 4 peak	Temporal Mid L -DC- 13791.1576	Temporal Inf L -DC- -4129.7397	Amygdala L, Hippocampus L -C- -6875.335
Spike 5 peak	N \A -DC- 20987.8525	N \A -DC- -0.97601	Amygdala L, Hippocampus L -C- -2488.1555

Table 5.8: *EEG source imaging results of five non-averaged spikes selected from the EEG recording of Patient 2. The epileptic focus lies in the amygdalo-hippocampal area. The results were visualized at the spikesâ peaks. For the maximum source activation, anatomical labels from the AAL atlas are shown. If the maximum of the estimated source activity falls within the resected region, the result is concordant, -C-, with the resected region; if the maximum does not fall within the resected region, the result is disconcordant, -DC-, with the resected region.*

Regions	Spike 1	Spike 2	Spike 3	Spike 4	Spike 5
Thalamus	-16.709	-35.204	-13.555	-25.246	-28.605
Amygdalo-hippocampal complex	-2.787	-3.443	-3.281	-3.385	-3.010
Cerebellum	-3.432	-4.569	-4.420	-4.357	-4.157
Putamen	-21.059	-19.277	-17.383	-28.641	-15.765
Caudate nucleus	-16.638	-16.316	-18.224	-25.500	-24.884
Cortex left	-5.450	-5.881	-5.357	-5.837	-5.447
Cortex right	-5.548	-6.162	-5.647	-5.988	-5.605

Table 5.9: *The table shows the RSTKF's regional dynamical noise standard deviations estimated from the clinical EEG data of five epileptic spikes. For each value, the natural logarithm of the standard deviation is shown. The number of regions was set to seven during the analyses.*

5.4 Discussion

In order to better describe regional dynamics and functional specialization in the brain, a generalization of the STKF was first introduced in [Ste08] and then further developed within the framework of this thesis. Simulated EEG datasets were first used to test the performance of RSTKF and compare it to that of STKF and LORETA. RSTKF had similar results to those of LORETA and STKF in the case of the frontal source. In the case of the sources in the putamen and thalamus, only RSTKF was successful in accurately localizing these sources. The distances between the simulated and reconstructed sources via LORETA and STKF grew larger, as the depth of the sources increased. The results of the simulated data confirmed our first two hypotheses. The application of RSTKF to the localization of five non-averaged spikes from Patient 2 and the comparison of the results to those of LORETA and STKF demonstrated that, for all spikes, RSTKF localized the source in the amygdalo-hippocampal complex. Unlike LORETA and STKF, RSTKF was both accurate and more focal at the spikes' onset and peak time points. Since we are dealing with a small lesion here, both accuracy and spatial resolution are needed in the inverse solution. The third hypothesis was confirmed by the results of the clinical spikes analysis. The final hypothesis was laos confirmed for both simulated and clinical EEG datasets, since RSTKF resulted in the smallest AIC values while LORETA showed the highest ABIC values. The number of EEG channels used for the imaging of simulated and clinical EEG data was smaller than 64. This makes the analyses in this chapter fall under the category of low-resolution EEG analyses. We would like to point out that RSTKF performed well even when the data had less than 64 channels. Additionally, we did not need the routine practice of spike averaging to obtain accurate results via RSTKF, since the use of non-averaged spikes was enough to obtain accurate localization results. Although the SNR value of simulated EEG was unrealistically high in this chapter, the RSTKF performed equally well when it was applied to the clinical spikes in this study that had realistic SNR.

The RSTKF has some advantages compared to other methods. First, RSTKF is used in conjunction with a standard head model that uses a 3D volumetric grid with a moderate number of grid points (3000-5000). No cortical meshes with a large number of points or a constraint on the dipole orientations are used by the RSTKF. Additionally, no special modeling of deep brain structures, as is the case of the deep brain activity (DBA) model [ABY$^+$07, AMFD12], or exclusion of the cerebellum, as is used in the CARTOOL software [BMM11], are needed. RSTKF seems much less affected by the grid choice and the choice of the Laplacian matrix, compared to LORETA and STKF. Compared to the popular time- or frequency domain beamformers, such as linearly-constrained minimum variance (LCMV) [VVVDYS97] and dynamic imaging of coherent sources (DICS) [GKH$^+$01], RSTKF does not need large segments of recordings that are needed to estimate the data's covariance or cross-spectral density matrix. Finally, RSTKF is a dynamical inverse solution which distinguishes the method from other approaches based on hierarchical Bayesian modeling (HBM) [LPBW12] and maximum entropy on the mean

This study suffers from some limitations. First the analyses were performed using a standard head model. In the future we intend to use the individual MRI and use a coregistered atlas to create the regional definitions. We only used 7 regions in this study. The definitions of more regions may be beneficial for explorative analyses in resting-state and task-related EEG recordings. The introduction of more regions may lead to problems in the optimization stage and this in turn would necessitate the use of better optimization methods. We used here dilation and smoothing since the grid spacing was 7 mm. This can be avoided if a grid resolution of 5 mm will be used. Finally, a group analysis with more subjects and more epochs per subject would give a better idea about the variability of the localization accuracy and consistency of RSTKF. The consistency of spike localization in this chapter may be a first confirmation for the lack of or small variability of localization of RSTKF.

In summary, we presented a generalization of the STKF with spatially-heterogeneous state-space model parameters and compared it to both LORETA and STKF using simulated and clinical EEG datasets. RSTKF outperformed both LORETA and STKF with respect to accuracy, consistency of localization, and spatial resolution. The results are promising since the method was able to localize deep sources and activity from small lesions, worked with low-resolution EEG data, and performed well with non-averaged spikes. The method may find application in the field of epileptology, especially in the source imaging of small lesions in mesial frontal and mesial temporal lobe epilepsies.

Chapter 6

Conclusions

6.1 Summary

Drug-resistant epilepsy may be treated by surgery in case of the correct identification of a single epilepsy generator in the brain. For that purpose, different neuroimaging modalities are used to localize the epileptogenic zone in the brain. Electroencephalography (EEG) and magnetoencephalography (MEG) are electrophysiological measures that have a high temporal resolution and are non-invasive. EEG is currently more in widespread use due to its cost effectiveness, mobility, and flexible usage without the need for shielding or cooling. New MEG sensors such as the optically-pumped magnetometers (OPM) operate in room temperature and may be placed on or closer to the human scalp compared to the standard superconducting quantum interference device (SQUID) MEG sensors. Although both EEG and MEG show a high temporal resolution, they have a low spatial resolution, since they measure the current density in the brain only indirectly. The presence of multiple head tissues with varying conductivity profiles leads to the distortion of the surface potentials or fields by volume conduction. The effect of volume conduction may be significantly suppressed by solving the M/EEG inverse problem to estimate the current density in the brain from measured M/EEG measurements and the solution of the M/EEG forward problem. Multiple studies have shown that EEG source imaging has comparable, or better, sensitivity and specificity in localizing the epileptogenic zone, compared to other non-invasive neuroimaging modalities [BLS$^+$09, BSL$^+$11, LPV$^+$16].

Distributed source methods are some of the most common methods that are used to solve the M/EEG inverse problem. These methods need to use a-priori information to solve the heavily underdetermined M/EEG inverse problem. The type of priors used by each method determines the performance and meaningfulness of the results of source reconstruction produced by that respective method. Some of the most common distributed source methods include minimum norm estimate (MNE) [Häm84], which uses minimum energy as a constraint, and low-resolution electromagnetic brain tomography (LORETA) [PMML94], which uses spatial smoothness as a constraint. The majority of the methods in this category are static or instantaneous inverse methods, i.e., they neglect the temporal information in the M/EEG time series and localize the sources at a single time point. In contrast to these methods, a dynamical inverse solution takes the time-series aspect of the M/EEG measurements into account when reconstructing the current density in the brain. Different strategies may be used to impose temporal smoothness constraints on the inverse solution. State-space modeling is a very flexible and powerful modeling tool to incorporate temporal smoothness constraints by having an explicit dynamical model, in addition to the measurement model, that describes the spatiotemporal evolution of the hidden variable, here the brain's current density, which is indirectly measured by M/EEG. Assuming the availability of a state-space model, a time-varying estimate of the hidden state is obtained via the Kalman filter [Kal60]. For medium and high-dimensional inverse problems, the use of the standard Kalman filter may become infeasible and reduced-rank versions or other modifications of the standard Kalman filter are used instead.

A modified version of the standard Kalman filter, called the spatiotemporal Kalman filter (STKF), which was suited to the high-dimensional M/EEG inverse problem, was suggested in [GYO$^+$04b]. In this algorithm, the fully-coupled state-space model is transformed via a linear transformation, the so-called spatial whitening transformation, into a weakly-coupled state-space model where only nearest-neighbor interactions are preserved. Local low-dimensional Kalman filters are then used at each voxel in the brain to estimate the local current density in the transformed state-space. At the end of the estimation process, the results are transformed back into the fully-coupled state-space model. Before state estimation is performed via the STKF, state-space model parameters are estimated via maximum likelihood (ML). Maximum likelihood estimation is performed via direct minimization of the Akaike information criterion (AIC). Additionally, AIC is also used for model comparison to evaluate how well the measurements are described by each inverse solution. One limitation of the STKF approach is the limitation of the state-space model parameters to be time-invariant and spatially-homogeneous.

One generalization of the STKF, the STKF with state-space generalized autoregressive conditional heteroskedasticity (GARCH) [GYO04a, WGYO06], may alleviate the above-mentioned limitation of the STKF. In this approach a spatiotemporal adaptation of the dynamical noise variance state-space model parameter was implemented in order to improve the accuracy, spatial resolution, and reconstruction of time courses in the brain. This generalization of the STKF is meant to improve the modeling of non-stationary data. The new algorithm was applied in [GOM$^+$08] on a clinical dataset containing a non-averaged epileptic spike and it outperformed LORETA in statistical model comparison, accuracy, spatial resolution, and reconstruction of dipole time courses. The algorithm suffers currently from numerical instability due to the high dimensionality of the M/EEG inverse problem.

Another solution to the limited nature of the model with temporally- and spatially- constant parameters is the regional STKF (RSTKF) that was first implemented in [Ste08]. In this algorithm, the dynamical noise variance parameter is defined individually for each brain region. The author in [Ste08] used only two brain regions that included both thalami, as the first region, and the rest of the brain as a second region. The method outperformed both LORETA and STKF in the localization of deep brain sources from simulated as well as clinical EEG data of sleep spindles and bursts. Additionally, model comparison showed the superiority of the novel algorithm to both LORETA and STKF.

Prior to the work presented here, the above-mentioned dynamical inverse methods were not investigated in detail regarding the factors that influence the accuracy, spatial resolution, and reconstruction of time courses in the brain. Additionally, they were not applied in conjunction with individual and realistic head models. No comparison of the performance of the algorithms in high-resolution EEG to that in low-resolution EEG was made. In addition to that, they were not applied to epileptic seizures or simultaneous MEG-EEG data. No dimensionality reduction approaches were used together with these methods to denoise the data or reduce the computational time.

The aim of this thesis was to improve the applicability of the STKF and the RSTKF in the field of epileptology and to continue the algorithmic development of the STKF and its regional variant, the RSTKF, by using state-of-the-art simulation models, realistic head models, and clinical recordings of epileptic spikes and seizures. The evaluation of the source imaging results was performed using postoperative MRIs, brain atlases, results of other neuroimaging modalities, and visual inspection by expert epileptologists.

Within the framework of this thesis, we aimed at improving the inverse-modeling step only. We did not use STKF with state-space GARCH in our analyses. Additionally, we decided to constrain ourselves to single-source scenarios. We mostly used EEG recordings for the analysis. Comparisons with other source imaging methods were limited only to LORETA, since it uses spatial smoothness constraints. Since the STKF uses temporal smoothness in addition to spatial smoothness constraints, the comparison with LORETA allows for the evaluation of the benefits of the additional temporal smoothness constraints.

The effects of grid choice and the definition of the Laplacian matrix on the performance of STKF were first investigated, for the first time, in chapter 3 using EEG data simulated via state-of-the-art neuronal population models [WBBC00, WHB$^+$05, CRBCW07, CRMB$^+$10] and realistic boundary-element (BE) head models. The neuronal population models allow for modeling the effects of excitation, inhibition, and connectivity among neuronal groups to generate normal background data, epileptic spikes, and different seizure patterns. The STKF results were compared to those of LORETA using model comparison, accuracy, and spatial resolution. The use of full-brain grids, instead of gray-matter ones, in conjunction with the modified definition of the Laplacian matrix, instead of the classical ones which assumes six neighbors for each voxel, produced the best accuracy and spatial resolution for STKF. In chapter 4 the same issue was investigated in section 4.2 using clinical EEG data from two epilepsy patients. Again the best results were obtained using a combination of a full-brain grid with the modified Laplacian matrix. This combination was found superior to the one with a full-brain grid and the classical Laplacian matrix by AIC model comparison for both simulated and clinical EEG data of spikes. In section 4.3 the effect of grid choice was investigated using an EEG recording of a focal seizure. The use of the full-brain grid produced the best localization results. The analyses via RSTKF in chapter 5 did not seem to be influenced by the grid choice or the definition of the

Laplacian matrix. This may indicate that the RSTKF is more robust to these factors than the STKF.

The question whether non-averaged or averaged spikes should be used in conjunction with the STKF was investigated in chapter 3. Spike averaging may be beneficial for improving the SNR. This, however, may lead to the suppression of interesting dynamics in the signal. Because of that we hypothesized that the STKF would work better with non-averaged spikes. The results of the investigation showed that moderate spike averaging (55 spikes in this thesis) improved the results of STKF and did not lead to a complete suppression of the signal dynamics in the pre- and post-spike periods. So STKF may be used together with non-averaged spikes or those that result from moderate averaging.

Most of the analyses in this thesis were performed using low-resolution EEG data, i.e., recordings with fewer than 64 electrodes. The reduction in the number of electrodes produced a more widespread activation and a shift towards the center of the brain. STKF was found to be more robust to this effect than LORETA. STKF results were more focal and closer to the original source than those of LORETA. The results do not only apply to the simulated spikes from chapter 3 . They also apply to the analyses of clinical spikes from section 4.2 as well as focal seizures in section 4.3 in chapter 4. We would like to mention here that STKF results were obtained with a very simple dynamical model. The improvements in the dynamical model may still improve STKF results with low-resolution EEG data. These results may have applications in EEG monitoring, wearable EEG, gaming and smartphone applications, and newborn EEG analyses. Additionally, large databases of 19-32 channel EEG recordings are available across the world in clinics and research centers.

When applying the STKF to two simulated high-resolution EEG datasets in chapter 3, instabilities that may have been caused by information redundancy led to incorrect localization and the appearance of spurious sources. In addition to that, the computational times of the STKF become much longer in case of high-resolution EEG data. Within the framework of this thesis, we used a dimensionality reduction approach, spatial projection [LLE$^+$14], that is based on singular value decomposition (SVD). This method was implemented in the SPM open-source toolbox and we wanted to integrate it, for the first time, within the STKF pipeline. In order to use the method in conjunction with our STKF, we needed to solve two problems. The first problem was about deciding whether to apply spatial projection before or after the spatial whitening transform. The second problem was about the choice of the threshold value for SVD truncation. The application of spatial projection gave the best results when it was performed after the spatial whitening transformation. Additionally, additional improvements in the accuracy and spatial resolution were obtained when the standard threshold value used in the SPM software was decreased down to a certain value. The application of spatial projection led to the suppression of spurious sources. The computational time of the STKF and the number of optimization steps required in the parameter estimation stage were both reduced due to the application of spatial projection.

In chapter 4, multimodal fusion of simultaneously-measured MEG-EEG was performed, for the first time, within the framework of source reconstruction via STKF in section 4.4. We generalized the measurement model of our state-space model to describe the data, lead field matrices, and measurement noises of simultaneously-measured MEG and EEG time series. For the M/EEG forward problem, we used a state-of-the-art six-compartment anisotropic finite-element (FE) head model whose skull conductivity was especially calibrated to account for the different sensitivities of MEG and EEG to the human skull's conductivity. In the inverse problem the STKF was applied on MEG-only, EEG-only, and on simultaneously-measured MEG-EEG datasets and the sources were localized at the spike peaks from MEG and EEG. The MEG-EEG datasets produced sources that were always in the expected area at both spike peaks. The use of MEG-only and EEG-only datasets produced accurate results only at the MEG peak, for the former datasets, and at the EEG peak, for the latter dataset, respectively. The complementary nature of simultaneous MEG-EEG may have contributed to the improvement in the STKF results when the generalized measurement model was used.

The regional STKF (RSTKF) was implemented by generalizing the dynamical model of the STKF's state-space model to include region-specific dynamical noise variances. In chapter 5 we increased the number of regions from two to seven and tested the RSTKF's performance on simulated EEG data. Additionally, we applied the RSTKF, for the first time, to epileptic spikes and compared its performance to that of LORETA and STKF. The RSTKF produced more accurate and consistent results, compared to those of LORETA and STKF, with increasing depth of sources. Additionally, its spatial resolution was better than that of the other two methods. Model comparison also favored RSTKF to LORETA and STKF. Similarly to STKF, RSTKF performed well in case of low-resolution EEG data and non-averaged epileptic spikes. Unlike STKF, the generalized algorithm was more suited to localize the epileptogenic zone when it has a smaller area or is identical with a subcortical brain structure. RSTKF may find application in the localization of epileptic generators that cause mesial frontal or mesial temporal epilepsies.

In summary, the performances of the STKF and RSTKF were investigated, mainly, for EEG generated from a single active source. The advantages of these methods, which are based on state-space modeling, were evaluated in comparison to LORETA, a well-established source imaging approach. For lateral brain sources, the STKF performed well, despite its simple dynamical model, the non-adaptive nature of the state-space model parameters, and the low-resolution EEG data. The brain grid and the Laplacian matrix need to be chosen with care. Among the different grids and definition of the Laplacian matrix that were used in this thesis, the combination of a full-brain grid and the modified definition of the Laplacian matrix led to the best STKF results. AIC model comparison may inform the choice of the Laplacian matrix when using the STKF. The additional temporal smoothness constraints, in the case of the STKF, improved the accuracy and consistency of the source reconstruction for epileptic spikes and focal seizures. STKF was mostly tested with low-resolution EEG data with up to 45 electrodes and was found to be more robust to the small number of electrodes than LORETA. Dimensionality reduction via spatial projection, which is based on singular value decomposition, was successfully combined with the STKF and has stabilized the STKF, suppressed spurious sources, and decreased the computational time. The use of STKF to analyze high-resolution EEG with 64-256 electrodes may be performed together with spatial projection. The acquisition of low-resolution EEG is still popular and practical in clinics, research centers, wearable EEG, and newborn monitoring. The reduction in SNR due to the use of non-averaged spikes did not lead to a significant performance drop for the STKF, although moderate spike averaging did lead to better STKF results. For simultaneously-measured MEG and EEG time series, MEG-EEG fusion via STKF is recommended over separate EEG or MEG analyses. For deep brain sources, the RSTKF is recommended because of its superiority in terms of accuracy, consistency, and spatial resolution. The STKF may find application in the analysis of spikes or focal seizures from lateral temporal or extratemporal sources. Deeper sources in mesial temporal or mesial frontal epilepsies may need a generalized version of the STKF such as the RSTKF.

6.2 Future Work

The investigations in this thesis were performed as a proof-of-concept. No large-scale group study, which involves multiple patients with several EEG segments, of epileptic spikes or focal seizures, per patient, was performed. Statistical validation of the STKF, or any of its generalized versions, requires this kind of study and using, in a similar fashion to [BSL$^+$11], the overlap of the reconstructed current density distribution with the segmented resected volume from postsurgical MRIs. Additionally, it could also be evaluated whether the maximum of the reconstructed current density distribution always falls within the resected volume or not. This kind of evaluation has been used in the last few years to evaluate source imaging results [WWY$^+$11, YWB$^+$11, LYW$^+$12]. These measures may also be used with simulated M/EEG data.

The use of full-brain grids has been shown to be an important factor in the STKF algorithm. Full-brain grids include white matter and CSF, which do not include any brain sources. Additionally, the use of full-brain grids will allow for source shifting outside the gray-matter, thus preventing the use of atlas comparisons. If we assume that the reason for the superior performance obtained when full-brain grids were used was the absence of thinly-sampled regions, since thin-sampling led to the shifting of the sources to other densely-sampled regions, then we may suggest the use of densely-sampled gray-matter grids. The performance of the STKF with this kind of grids still needs to be investigated. The modified definition of the Laplacian matrix solved the other problem of shifting sources, which was caused by the classical definition of the Laplacian matrix. This definition resulted in very low or zero current density at the borders of the grid. The modified definition of the Laplacian matrix was also, consistently for the STKF, favored by AIC model comparison. Other definitions of the Laplacian matrix that involve more than the six immediate neighbors on the x, y, and z axes may be investigated and selected via model comparison.

For each voxel, after spatial whitening, only the connections to the six immediate neighbors on the x, y, and z axes are retained. Since long-range connections also exist in the human cortex, structural information from DT-MRI may be used to include this information in the STKF's dynamical model. We assume that the absence of these connections in the current dynamical model of the STKF does not lead to wrong results. The inclusion of these connections may still help in modeling, e.g., propagation of epileptic activity during the occurrence of spikes or seizures more accurately. The effects of the anatomical complexity of the head model on STKF were not investigated here. A spherical model may, e.g., be compared with a 3-compartment realistic boundary-element model and with a 3-7 compartment realistic model based on finite elements or finite differences.

The dynamical nature of the RSTKF made it more robust to the small number of electrodes in this thesis, compared to LORETA. The robustness of the STKF to the presence of common artifacts such as eye-blink, eye-movement, muscle, and movement artifacts can also be investigated in a future study. Additionally, we get an idea in this thesis about the performance of the STKF and the RSTKF with different SNR values. A future study may apply STKF or RSTKF to data with very low SNR values, e.g., 0-8 dB.

The promising results of STKF in MEG-EEG fusion may encourage more studies regarding dimensionality reduction, since the total number of MEG and EEG sensors in simultaneous measurements is usually larger than 300. Additionally, MEG-EEG fusion may be combined with the generalized version of the STKF, e.g., the RSTKF, since they have improved dynamical models. The application of the STKF, or any of its variants, to high-resolution EEG or MEG needs further investigations to discover the advantages and possible problems that may result from the larger number of sensors.

For the RSTKF, CURRY7 offers the possibility of individual atlas generation for each individual MRI. This may allow for more accuracy, especially when the patient's anatomy strongly deviates from standard MRIs. Additionally, the addition of more regions to the RSTKF may be necessary to improve its applicability to cognitive brain research. The inclusion of more brain areas may create problems for the optimization algorithms. New and powerful optimization methods for global optimization can be tested in a future study.

This thesis covered M/EEG source imaging in case of a single active source. The assumption of multiple active sources is reasonable, especially in case of seizures, and the ability of a source imaging method to separate two sources at a small distance from each other is an important parameter in source imaging. An interesting question can be the possibility of detecting a deep source in the presence of one or more active superficial sources. Additional preprocessing steps that involve frequency-domain filtering or blind source separation may be necessary to separate the contributions of each source if the RSTKF fails to detect all the active sources.

Finally, the implementation of square-root versions of the STKF may improve numerical stability of the linear STKF by preserving the positive-definite characteristic of the STKF's covariance matrices. We have not implemented non-linear variants of the STKF. A future study may check whether certain seizure dynamics may benefit from the implementation of a state-space model with a non-linear dynamical model for the purpose of source imaging.

List of Figures

List of Tables

Bibliography

[ABY$^+$07] Y. Attal, M. Bhattacharjee, J. Yelnik, B. Cottereau, J. Lefèvre, Y. Okada, E. Bardinet, M. Chupin, and S. Baillet, “Modeling and detecting deep brain activity with MEG & EEG,” in *Engineering in Medicine and Biology Society, 2007. EMBS 2007. 29th Annual International Conference of the IEEE.* IEEE, 2007, pp. 4937–4940.

[Aka98] H. Akaike, “Information theory and an extension of the maximum likelihood principle,” in *Selected papers of hirotugu akaike*. Springer, 1998, pp. 199–213.

[Alf14] A. Alfarawn, “Comparison of static and dynamic source imaging of epileptiform discharges simulated using a neuronal population model,” master thesis, Digital Signal Processing and System Theory , Christian-Albrechts-University of Kiel, 2014.

[AMFD12] Y. Attal, B. Maess, A. Friederici, and O. David, “Head models and dynamic causal modeling of subcortical activity using magnetoencephalographic/electroencephalographic data,” *Reviews in the Neurosciences*, vol. 23, no. 1, pp. 85–95, 2012.

[AVD$^+$15] Ü. Aydin, J. Vorwerk, M. Dümpelmann, P. Küpper, H. Kugel, M. Heers, J. Wellmer, C. Kellinghaus, J. Haueisen, S. Rampp *et al.*, “Combined EEG/MEG can outperform single modality EEG or MEG source reconstruction in presurgical epilepsy diagnosis,” *PLoS One*, vol. 10, no. 3, p. e0118753, 2015.

[AVK$^+$14] Ü. Aydin, J. Vorwerk, P. Küpper, M. Heers, H. Kugel, A. Galka, L. Hamid, J. Wellmer, C. Kellinghaus, S. Rampp *et al.*, “Combining EEG and MEG for the reconstruction of epileptic activity using a calibrated realistic volume conductor model,” *PLoS One*, vol. 9, no. 3, p. e93154, 2014.

[BLS$^+$09] V. Brodbeck, A. M. Lascano, L. Spinelli, M. Seeck, and C. M. Michel, “Accuracy of EEG source imaging of epileptic spikes in patients with large brain lesions,” *Clinical Neurophysiology*, vol. 120, no. 4, pp. 679–685, 2009.

[BML01] S. Baillet, J. C. Mosher, and R. M. Leahy, “Electromagnetic brain mapping,” *IEEE Signal processing magazine*, vol. 18, no. 6, pp. 14–30, 2001.

[BMM11] D. Brunet, M. M. Murray, and C. M. Michel, “Spatiotemporal analysis of multichannel EEG: CARTOOL,” *Computational intelligence and neuroscience*, vol. 2011, p. 2, 2011.

[BRK$^+$09] M. J. Barton, P. A. Robinson, S. Kumar, A. Galka, H. F. Durrant-Whyte, J. Guivant, and T. Ozaki, “Evaluating the performance of Kalman-filter-based EEG source localization,” *IEEE transactions on biomedical engineering*, vol. 56, no. 1, pp. 122–136, 2009.

[BSL$^+$11] V. Brodbeck, L. Spinelli, A. M. Lascano, M. Wissmeier, M.-I. Vargas, S. Vulliemoz, C. Pollo, K. Schaller, C. M. Michel, and M. Seeck, “Electroencephalographic source imaging: a prospective study of 152 operated epileptic patients,” *Brain*, vol. 134, no. 10, pp. 2887–2897, 2011.

[C$^+$00] S. Consortium *et al.*, “SimBio: A generic environment for bio-numerical simulation,” 2000.

[Cha94] D. Chadwick, “Epilepsy.” *Journal of Neurology, Neurosurgery & Psychiatry*, vol. 57, no. 3, pp. 264–277, 1994. [Online]. Available: https://jnnp.bmj.com/content/57/3/264

[Com11] *CURRY7 User Guide*, Compumedics USA, Inc., 2011, www.neuroscan.com.

[CRBCW07] D. Cosandier-Rimélé, J.-M. Badier, P. Chauvel, and F. Wendling, “A physiologically plausible spatio-temporal model for EEG signals recorded with intracerebral electrodes in human partial epilepsy,” *Biomedical Engineering, IEEE Transactions on*, vol. 54, no. 3, pp. 380–388, 2007.

[CRMB$^+$10] D. Cosandier-Rimélé, I. Merlet, F. Bartolomei, J.-M. Badier, and F. Wendling, “Computational modeling of epileptic activity: from cortical sources to EEG signals,” *Journal of clinical neurophysiology*, vol. 27, no. 6, pp. 465–470, 2010.

[dS13] F. L. da Silva, “EEG and MEG: relevance to neuroscience,” *Neuron*, vol. 80, no. 5, pp. 1112–1128, 2013.

[EJ93] J. Engel Jr, “Outcome with respect to epileptic seizures.” *Surgical treatment of the epilepsies*, pp. 609–621, 1993.

[Eng01] J. Engel, “A proposed diagnostic scheme for people with epileptic seizures and with epilepsy: report of the ILAE task force on classification and terminology,” *Epilepsia*, vol. 42, no. 6, pp. 796–803, 2001.

[Eve94] G. Evensen, “Sequential data assimilation with a nonlinear quasi-geostrophic model using Monte Carlo methods to forecast error statistics,” *Journal of Geophysical Research: Oceans*, vol. 99, no. C5, pp. 10 143–10 162, 1994.

[GCM$^+$08] R. Grech, T. Cassar, J. Muscat, K. Camilleri, S. Fabri, M. Zervakis, P. Xanthopoulos, V. Sakkalis, and B. Vanrumste, "Review on solving the inverse problem in EEG source analysis," *Journal of NeuroEngineering and Rehabilitation*, vol. 5, no. 1, p. 25, 2008. [Online]. Available: http://www.jneuroengrehab.com/content/5/1/25

[GKH$^+$01] J. Groß, J. Kujala, M. Hämäläinen, L. Timmermann, A. Schnitzler, and R. Salmelin, "Dynamic imaging of coherent sources: studying neural interactions in the human brain," *Proceedings of the National Academy of Sciences*, vol. 98, no. 2, pp. 694–699, 2001.

[GOM$^+$08] A. Galka, T. Ozaki, H. Muhle, U. Stephani, and M. Siniatchkin, "A data-driven model of the generation of human EEG based on a spatially distributed stochastic wave equation," *Cognitive neurodynamics*, vol. 2, no. 2, p. 101, 2008.

[GPOC10] A. Gramfort, T. Papadopoulo, E. Olivi, and M. Clerc, "OpenMEEG: opensource software for quasistatic bioelectromagnetics," *Biomedical engineering online*, vol. 9, no. 1, p. 45, 2010.

[GWO10] A. Galka, K. Wong, and T. Ozaki, "Generalized state-space models for modeling nonstationary EEG time-series," in *Modeling Phase Transitions in the Brain*. Springer, 2010, pp. 27–52.

[GYO04a] A. Galka, O. Yamashita, and T. Ozaki, "GARCH modelling of covariance in dynamical estimation of inverse solutions," *Physics Letters A*, vol. 333, no. 3-4, pp. 261–268, 2004.

[GYO$^+$04b] A. Galka, O. Yamashita, T. Ozaki, R. Biscay, and P. Valdés-Sosa, "A solution to the dynamical inverse problem of EEG generation using spatiotemporal Kalman filtering," *NeuroImage*, vol. 23, no. 2, pp. 435–453, 2004.

[Hab14] N. Habboush, "MEG-EEG fusion using spatiotemporal Kalman filtering with an emphasis on the correct localization of deep brain sources," master thesis, Digital Signal Processing and System Theory , Christian-Albrechts-University of Kiel, 2014.

[HAFM$^+$17a] L. Hamid, A. Al Farawn, I. Merlet, N. Japaridze, U. Heute, U. Stephani, A. Galka, F. Wendling, and M. Siniatchkin, "Source reconstruction via the spatiotemporal Kalman filter and LORETA from EEG time series with 32 or fewer electrodes," in *Engineering in Medicine and Biology Society (EMBC), 2017 39th Annual International Conference of the IEEE*. IEEE, 2017, pp. 2218–2222.

[HAFM$^+$17b] ——, "Spatial projection as a preprocessing step for EEG source reconstruction using spatiotemporal Kalman filtering," in *Engineering in Medicine and Biol-*

ogy Society (EMBC), 2017 39th Annual International Conference of the IEEE. IEEE, 2017, pp. 2213–2217.

[Häm84] M. Hämäläinen, "Interpreting measured magnetic fields of the brain: estimates of current distributions," *Univ. Helsinki, Finland Tech. Rep. TKK-F-A559*, 1984.

[HAW$^+$13] L. Hamid, Ü. Aydin, C. Wolters, U. Stephani, M. Siniatchkin, and A. Galka, "MEG-EEG fusion by Kalman filtering within a source analysis framework," in *Engineering in Medicine and Biology Society (EMBC), 2013 35th Annual International Conference of the IEEE.* IEEE, 2013, pp. 4819–4822.

[HDN14] S. Haufe, S. Dähne, and V. V. Nikulin, "Dimensionality reduction for the analysis of brain oscillations," *NeuroImage*, vol. 101, pp. 583–597, 2014.

[HGF$^+$05] H.-J. Huppertz, C. Grimm, S. Fauser, J. Kassubek, I. Mader, A. Hochmuth, J. Spreer, and A. Schulze-Bonhage, "Enhanced visualization of blurred gray-white matter junctions in focal cortical dysplasia by voxel-based 3D MRI analysis," *Epilepsy research*, vol. 67, no. 1-2, pp. 35–50, 2005.

[HHJ$^+$15] N. Habboush, L. Hamid, N. Japaridze, G. Wiegand, U. Heute, U. Stephani, A. Galka, and M. Siniatchkin, "The choice of the source space and the Laplacian matrix in LORETA and the spatio-temporal Kalman filter EEG inverse methods," in *Engineering in Medicine and Biology Society (EMBC), 2015 37th Annual International Conference of the IEEE.* IEEE, 2015, pp. 2745–2749.

[HSJ$^+$15] L. Hamid, M. Sarabi, N. Japaridze, G. Wiegand, U. Heute, U. Stephani, A. Galka, and M. Siniatchkin, "The performance of the spatiotemporal Kalman filter and LORETA in seizure onset localization," in *Engineering in Medicine and Biology Society (EMBC), 2015 37th Annual International Conference of the IEEE.* IEEE, 2015, pp. 2741–2744.

[IRY16] M. K. Islam, A. Rastegarnia, and Z. Yang, "Methods for artifact detection and removal from scalp EEG: a review," *Neurophysiologie Clinique/Clinical Neurophysiology*, vol. 46, no. 4-5, pp. 287–305, 2016.

[JBB$^+$12] M. Jenkinson, C. F. Beckmann, T. E. Behrens, M. W. Woolrich, and S. M. Smith, "FSL," *Neuroimage*, vol. 62, no. 2, pp. 782–790, 2012.

[JKM$^+$14] M. A. Jatoi, N. Kamel, A. S. Malik, I. Faye, and T. Begum, "A survey of methods used for source localization using EEG signals," *Biomedical Signal Processing and Control*, vol. 11, pp. 42–52, 2014.

[JPS$^+$05] M. Jenkinson, M. Pechaud, S. Smith *et al.*, "BET2: MR-based estimation of brain, skull and scalp surfaces," in *Eleventh annual meeting of the organization for human brain mapping*, vol. 17. Toronto., 2005, p. 167.

[JUDW95] S. J. Julier, J. K. Uhlmann, and H. F. Durrant-Whyte, "A new approach for filtering nonlinear systems," in *American Control Conference, Proceedings of the 1995*, vol. 3. IEEE, 1995, pp. 1628–1632.

[Kal60] R. E. Kalman, "A new approach to linear filtering and prediction problems," *Journal of Basic Engineering*, vol. 82, no. 1, pp. 35–45, 1960.

[LLE$^+$14] J. López, V. Litvak, J. Espinosa, K. Friston, and G. R. Barnes, "Algorithmic procedures for Bayesian MEG/EEG source reconstruction in SPM," *NeuroImage*, vol. 84, pp. 476–487, 2014.

[LMK$^+$11] V. Litvak, J. Mattout, S. Kiebel, C. Phillips, R. Henson, J. Kilner, G. Barnes, R. Oostenveld, J. Daunizeau, G. Flandin *et al.*, "EEG and MEG data analysis in SPM8," *Computational intelligence and neuroscience*, vol. 2011, 2011.

[LPBW12] F. Lucka, S. Pursiainen, M. Burger, and C. H. Wolters, "Hierarchical Bayesian inference for the EEG inverse problem using realistic FE head models: depth localization and source separation for focal primary currents," *Neuroimage*, vol. 61, no. 4, pp. 1364–1382, 2012.

[LPV$^+$16] A. M. Lascano, T. Perneger, S. Vulliemoz, L. Spinelli, V. Garibotto, C. M. Korff, M. I. Vargas, C. M. Michel, and M. Seeck, "Yield of MRI, high-density electric source imaging (HD-ESI), SPECT and PET in epilepsy surgery candidates," *Clinical Neurophysiology*, vol. 127, no. 1, pp. 150–155, 2016.

[LYW$^+$12] Y. Lu, L. Yang, G. A. Worrell, B. Brinkmann, C. Nelson, and B. He, "Dynamic imaging of seizure activity in pediatric epilepsy patients," *Clinical Neurophysiology*, vol. 123, no. 11, pp. 2122–2129, 2012.

[McE66] B. A. McElhoe, "An assessment of the navigation and course corrections for a manned flyby of Mars or Venus," *IEEE Transactions on Aerospace and Electronic Systems*, no. 4, pp. 613–623, 1966.

[MI16] T. Moberget and R. B. Ivry, "Cerebellar contributions to motor control and language comprehension: searching for common computational principles," *Annals of the New York Academy of Sciences*, vol. 1369, no. 1, pp. 154–171, 2016.

[NP15] G. Nakamura and R. Potthast, *Inverse Modeling*, ser. 2053-2563. IOP Publishing, 2015. [Online]. Available: http://dx.doi.org/10.1088/978-0-7503-1218-9

[NSW$^+$97] P. L. Nunez, R. Srinivasan, A. F. Westdorp, R. S. Wijesinghe, D. M. Tucker, R. B. Silberstein, and P. J. Cadusch, "EEG coherency: I: statistics, reference electrode, volume conduction, Laplacians, cortical imaging, and interpretation at multiple scales," *Electroencephalography and clinical neurophysiology*, vol. 103, no. 5, pp. 499–515, 1997.

[OFMS11] R. Oostenveld, P. Fries, E. Maris, and J.-M. Schoffelen, “FieldTrip: open source software for advanced analysis of MEG, EEG, and invasive electrophysiological data,” *Computational intelligence and neuroscience*, vol. 2011, p. 1, 2011.

[OTF07] V. P. Oikonomou, A. T. Tzallas, and D. I. Fotiadis, “A Kalman filter based methodology for EEG spike enhancement,” *Computer methods and programs in biomedicine*, vol. 85, no. 2, pp. 101–108, 2007.

[Oza12] T. Ozaki, *Time series modeling of neuroscience data*. CRC Press, 2012.

[PM95] R. Pascual-Marqui, “Reply to comments by Hämäläinen, Ilmoniemi and Nunez,” *Source localization: continuing discussion of the inverse problem*, vol. 6, pp. 16–28, 1995.

[PM99] R. D. Pascual-Marqui, “Review of methods for solving the EEG inverse problem,” *International journal of bioelectromagnetism*, vol. 1, no. 1, pp. 75–86, 1999.

[PMML94] R. D. Pascual-Marqui, C. M. Michel, and D. Lehmann, “Low resolution electromagnetic tomography: a new method for localizing electrical activity in the brain,” *International Journal of psychophysiology*, vol. 18, no. 1, pp. 49–65, 1994.

[Sar14] M. Sarabi, “EEG source imaging of epileptiform seizures using spatio-temporal Kalman filteringl,” master thesis, Digital Signal Processing and System Theory , Christian-Albrechts-University of Kiel, 2014.

[Sch12] S. J. Schiff, *Neural control engineering: the emerging intersection between control theory and neuroscience*. MIT Press, 2012.

[SGHSG17] A. Santillán-Guzmán, U. Heute, U. Stephani, and A. Galka, “Comparison of different methods to suppress muscle artifacts in EEG signals,” *Signal, Image and Video Processing*, vol. 11, no. 4, pp. 761–768, 2017.

[SSM62] G. L. Smith, S. F. Schmidt, and L. A. McGee, *Application of statistical filter theory to the optimal estimation of position and velocity on board a circumlunar vehicle*. National Aeronautics and Space Administration, 1962.

[Ste08] P. Stern, “Improved detection of deep neural activity from EEG measurements by the Kalman filter approach for inverse solutions,” diploma thesis, Institute of Theoretical Physics and Astrophysics, Christian-Albrechts-University of Kiel, 2008.

[TMLP$^+$02] N. Tzourio-Mazoyer, B. Landeau, D. Papathanassiou, F. Crivello, O. Etard, N. Delcroix, B. Mazoyer, and M. Joliot, “Automated anatomical labeling of activations in SPM using a macroscopic anatomical parcellation of the MNI MRI single-subject brain,” *Neuroimage*, vol. 15, no. 1, pp. 273–289, 2002.

[UGZ15] J. A. Urigüen and B. Garcia-Zapirain, “EEG artifact removal—state-of-the-art and guidelines,” *Journal of neural engineering*, vol. 12, no. 3, p. 031001, 2015.

[VH97] M. Verlaan and A. W. Heemink, “Tidal flow forecasting using reduced rank square root filters,” *Stochastic hydrology and Hydraulics*, vol. 11, no. 5, pp. 349–368, 1997.

[VVVDYS97] B. D. Van Veen, W. Van Drongelen, M. Yuchtman, and A. Suzuki, “Localization of brain electrical activity via linearly constrained minimum variance spatial filtering,” *IEEE Transactions on biomedical engineering*, vol. 44, no. 9, pp. 867–880, 1997.

[WBBC00] F. Wendling, J.-J. Bellanger, F. Bartolomei, and P. Chauvel, “Relevance of nonlinear lumped-parameter models in the analysis of depth-EEG epileptic signals,” *Biological cybernetics*, vol. 83, no. 4, pp. 367–378, 2000.

[WGYO06] K. F. K. Wong, A. Galka, O. Yamashita, and T. Ozaki, “Modelling nonstationary variance in EEG time series by state space GARCH model,” *Computers in biology and medicine*, vol. 36, no. 12, pp. 1327–1335, 2006.

[WHB$^+$05] F. Wendling, A. Hernandez, J.-J. Bellanger, P. Chauvel, and F. Bartolomei, “Interictal to ictal transition in human temporal lobe epilepsy: insights from a computational model of intracerebral EEG,” *Journal of Clinical Neurophysiology*, vol. 22, no. 5, p. 343, 2005.

[Wol38] H. Wold, “A study in the analysis of stationary time series,” Ph.D. dissertation, Almqvist & Wiksell, 1938.

[WWY$^+$11] G. Wang, G. Worrell, L. Yang, C. Wilke, and B. He, “Interictal spike analysis of high-density EEG in patients with partial epilepsy,” *Clinical neurophysiology*, vol. 122, no. 6, pp. 1098–1105, 2011.

[Yam03] O. Yamashita, “Dynamical EEG inverse problem and causality analysis of fMRI data,” PhD. thesis, Department of Statistical Science, School of Mathematical and Physical Science, The Graduate University for Advanced Studiesl, 2003.

[YGO$^+$04] O. Yamashita, A. Galka, T. Ozaki, R. Biscay, and P. Valdes-Sosa, “Recursive penalized least squares solution for dynamical inverse problems of EEG generation,” *Human brain mapping*, vol. 21, no. 4, pp. 221–235, 2004.

[YWB$^+$11] L. Yang, C. Wilke, B. Brinkmann, G. A. Worrell, and B. He, “Dynamic imaging of ictal oscillations using non-invasive high-resolution EEG,” *Neuroimage*, vol. 56, no. 4, pp. 1908–1917, 2011.

[ZBS01] Y. Zhang, M. Brady, and S. Smith, “Segmentation of brain MR images through a hidden Markov random field model and the expectation-maximization algorithm,” *IEEE transactions on medical imaging*, vol. 20, no. 1, pp. 45–57, 2001.

Bisher sind in der Reihe

Arbeiten über Digital Signalverarbeitung

folgende Bände ersichernen:

Nr. 1 **Luis Arévalo**
Beiträge zur Schätzung der Frequenzen gestörter Schwingungen kurzer
Dauer und eine Anwendung auf die Analyse von Sprachsignalen, 1991

Nr. 2 **Rolf Gluth**
Beiträge zur Beschreibung und Realisierung digitaler, nichtrekursiver Filterbänke
auf der Grundlage linearer diskreter Transformationen, 1993

Nr. 3 **Ulrich Halka**
Objektive Qualitätsbeurteilung von Sprachkodierverfahren unter Anwendung von
Sprachmodellprozessen, 1993

Nr. 4 **Holger Carl**
Untersuchung verschiedener Methoden der Sprachkodierung und eine Anwendung
zur Bandbreitenvergrößerung von Schmalband-Sprachsignalen, 1994

Nr. 5 **Marcelo Iribarren B.**
Real-Time Spectral Estimation of Plasma Waves Using Space-Plasma Particle
Measurements, 1994

Nr. 6 **Abdul Nasir Hossen**
Fast Approximate Discrete Fourier Transform Based on Subband
Decomposition, 1994

Nr. 7 **Hualiang Qi**
Entwurf von FIR-Filtern mit extremen Wortälngen-Beschränkungen, 1995

Nr. 8 **Stefan Dobler**
Adaptionsmechanismen für telefonbasierte Spracherkennungssysteme, 1996

Nr. 9 **Andreas Elterich**
Ein Beitrag zur Schätzung der wahren Geschwindigkeit über Grund mit einem Dopplerradar, 1997

Nr. 10 **Markus Hauenstein**
Psychoakustisch motivierte Maße zur instrumentellen Sprachgütebeurteilung, 1997

Nr. 11 **Andreas Engelsberg**
Transformationsbasierte Systeme zur einkanaligen Störunterdrückung bei Sprachsignalen, 1998

Nr. 12 **Reza Serafat**
Sprachmodellprozesse bei Vorgabe theoretischer und anwendungsorientierter Eigenschaften, 1998

Nr. 13 **Jens Berger**
Instrumentelle Verfahren zur Sprachqualitätsschätzung-Modelle auditiver Tests, 1998

Nr. 14 **Norbert Görtz**
Aufwandsarme Qualitätsverbesserungen bei der gestörten Übertragung codierter Sprachsignale, 1999

Nr. 15 **Udo Görtz**
Entwicklung eines verbesserten Sprachcodecs für das GSM-Vollraten-Mobilfunknetz, 1999

Nr. 16 **Jörg Kliewer**
Beiträge zum Entwurf modulierter Filterbänke für verschiedene Teilbandabtastraten, 1999

Nr. 17 **Thomas Lungwitz**
Untersuchungen zur mehrkanaligen adaptiven Geräuschreduktion für die Spracherkennung im Kraftfahrzeug, 1999

Nr. 18 **Guangyu Wang**
Time-Varying Filter Banks and Transform Coding for Speech and Audio Signals, 2000

Nr. 19 **Wolfram Ehnert**
Sprachcodierung variabler Bitrate mit phonembasierten Ansätzen, 2000

Nr. 20 **Thomas Gülzow**
Verbesserung der Qualität stark gestörter Sprache - Detektion eines Trägerversatzes und Unterdrückung additiver Störungen, 2001

Nr. 21 **Andreas Korthauer**
Methoden der Merkmalsextraktion für die robuste Erkennung von Buchstabiersequenzen in geräuschbehafteter Umgebung, 2001

Nr. 22 **Enisa Galijašević**
Allpass-Based Near-Perfect-Reconstruction Filter Banks, 2002

Nr. 23 **Thorsten Ludwig**
Messung von Signaleigenschaften zur referenzfreien Qualitätsbewertung von Telefonbandsprache, 2003

Nr. 24 **Walter Koch**
Optimierungsverfahren für einen universellen Spracherkenner mit robusten, effizienten Algorithmen, 2004

Nr. 25 **Lutz Leutelt**
Stimmcharakteristika und deren Transformation auf der Grundlage parametrischer Codierung, 2004

Nr. 26 **Christian Kubaczyk**
Beitrag zur Bestimmung der Kanalkapazität des zeitvarianten akustischen Flachwasserkanals, 2007

Nr. 27 **Tomasz Ruść**
Quality of Quantized and Non-Quantized FIR Filters for Single Channels or Near-Perfect Reconstruction Cosine-Modulated Filter Banks, 2007

Nr. 28 **Claude Schermesser**
Simulation and Rejection of Interferences with an Airborne Multichannel Radar, 2007

Nr. 29 **Ragnar Thobaben**
Iterative Quellen- und Kanaldecodierung mit Codes variabler Länge, 2007

Nr. 30 **Peer Dahl**
Zeit-/Frequenzanalyse - Eine neue Lösung zur hoch auflösenden Zeit-/Frequenzanalyse im Vergleich mit bekannten linearen und nicht-linearen Verfahren unter allgemeinen Analysebedingungen, 2007

Nr. 31 **Deepa Janardhanan**

Wideband Speech Enhancement, 2008

Nr. 32 **Kirstin Scholz**
Instrumentelle Qualitätsbeurteilung von Telefonbandsprache beruhend auf Qualitätsattributen, 2008

Nr. 33 **Jan Schwarz**
Statistische Stimmenumwandlung in Kombination mit prosodischen Modellen, 2010

Nr. 34 **Muthuraman Muthuraman**
Interactions in Complex Tremor-Related Motor Networks of the Brain, 2010

Nr. 35 **Halil Özer**
Untersuchung des Elektrokardiogramms bezüglich eines Zusammenhanges zwischen Herzaktivität und Schlaf, 2010

Nr. 36 **Kathrin Wilkens**
Multi-Hypthesentracking-Verfahren mit datenfusionierenden Algorithmen, 2012

Nr. 37 **Alina Santillan Guzman**
Digital Enhancement of EEG/MEG Signals, 2013

Nr. 38 **Christoph Robert Norrenbrock**
Instrumental Quality Estimation for Synthesized Speech Signals, 2014

Nr. 39 **Abdul Rauf Anwar**
Multimodal Analysis of Directional Interactions in Oscillatory Networks of the Brain, 2014

Nr. 40 **Lu Huo**
Attribute-based Speech Quality Assessment - Narrowband and Wideband, 2015

Nr. 41 **Viet Duc Nguyen**
Einfluss von Gating-Algorithmen in der Objektverfolgung am Beispiel des Multi-Hypothesentracking, 2015

Nr. 42 **Kidist Gebremariam Mideksa**
Source Analysis on Simultaneously Measured Magnetoencephalography and Electroencephalography Signals of the Brain in Tremors and Epileptic Disorders, 2015

Nr. 43 **Roman Kreimeyer**

Klassifikation von MeeressÃugern mit Mitteln der Spracherkennung, 2016

Nr. 44 **Tim Claussen**
Kognitives MIMO Sonarsystem zur Detektion von Taucherangriffen, 2017